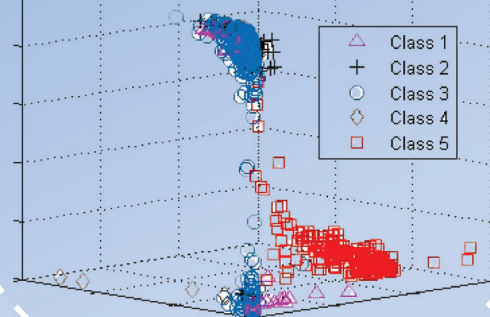
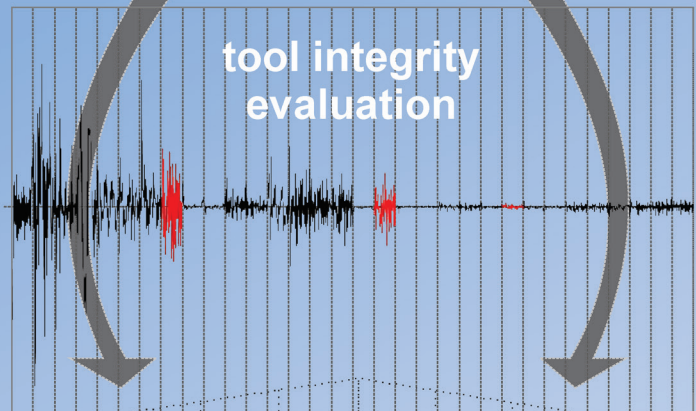
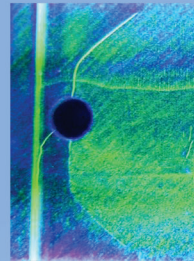




Strojniški vestnik

Journal of Mechanical Engineering



no. 11

year 2018

volume 64

Aim and Scope

The international journal publishes original and (mini)review articles covering the concepts of materials science, mechanics, kinematics, thermodynamics, energy and environment, mechatronics and robotics, fluid mechanics, tribology, cybernetics, industrial engineering and structural analysis.

The journal follows new trends and progress proven practice in the mechanical engineering and also in the closely related sciences as are electrical, civil and process engineering, medicine, microbiology, ecology, agriculture, transport systems, aviation, and others, thus creating a unique forum for interdisciplinary or multidisciplinary dialogue.

The international conferences selected papers are welcome for publishing as a special issue of SV-JME with invited co-editor(s).

Editor in Chief

Vincenc Butala

University of Ljubljana, Faculty of Mechanical Engineering, Slovenia

Technical Editor

Pika Škraba

University of Ljubljana, Faculty of Mechanical Engineering, Slovenia

Founding Editor

Bojan Kraut

University of Ljubljana, Faculty of Mechanical Engineering, Slovenia

Editorial Office

University of Ljubljana, Faculty of Mechanical Engineering

SV-JME, Aškerčeva 6, SI-1000 Ljubljana, Slovenia

Phone: 386 (0)1 4771 137

Fax: 386 (0)1 2518 567

info@sv-jme.eu, <http://www.sv-jme.eu>

Print: Abografika, printed in 300 copies

Founders and Publishers

University of Ljubljana, Faculty of Mechanical Engineering, Slovenia

University of Maribor, Faculty of Mechanical Engineering, Slovenia

Association of Mechanical Engineers of Slovenia

Chamber of Commerce and Industry of Slovenia,

Metal Processing Industry Association

President of Publishing Council

Mitjan Kalin

University of Ljubljana, Faculty of Mechanical Engineering, Slovenia

Vice-President of Publishing Council

Jože Balič

University of Maribor, Faculty of Mechanical Engineering, Slovenia

International Editorial Board

Kamil Arslan, Karabuk University, Turkey

Hafiz Muhammad Ali, University of Engineering and Technology, Pakistan

Josep M. Bergada, Politechnical University of Catalonia, Spain

Anton Bergant, Litoštroj Power, Slovenia

Miha Boltežar, UL, Faculty of Mechanical Engineering, Slovenia

Franci Čuš, UM, Faculty of Mechanical Engineering, Slovenia

Janez Diaci, UL, Faculty of Mechanical Engineering, Slovenia

Anselmo Eduardo Diniz, State University of Campinas, Brazil

Igor Emri, UL, Faculty of Mechanical Engineering, Slovenia

Imre Felde, Obuda University, Faculty of Informatics, Hungary

Janez Grum, UL, Faculty of Mechanical Engineering, Slovenia

Imre Horvath, Delft University of Technology, The Netherlands

Aleš Hribernik, UM, Faculty of Mechanical Engineering, Slovenia

Soichi Ibaraki, Kyoto University, Department of Micro Eng., Japan

Julius Kaplunov, Brunel University, West London, UK

Iyas Khader, Fraunhofer Institute for Mechanics of Materials, Germany

Jernej Klemenc, UL, Faculty of Mechanical Engineering, Slovenia

Milan Kljajin, J.J. Strossmayer University of Osijek, Croatia

Peter Krajnik, Chalmers University of Technology, Sweden

Janez Kušar, UL, Faculty of Mechanical Engineering, Slovenia

Gorazd Lojen, UM, Faculty of Mechanical Engineering, Slovenia

Thomas Lübben, University of Bremen, Germany

George K. Nikas, KADMOS Engineering, UK

José L. Ocaña, Technical University of Madrid, Spain

Vladimir Popović, University of Belgrade, Faculty of Mech. Eng., Serbia

Franci Pušavec, UL, Faculty of Mechanical Engineering, Slovenia

Bernd Sauer, University of Kaiserslautern, Germany

Rudolph J. Scavuzzo, University of Akron, USA

Branko Vasić, University of Belgrade, Faculty of Mechanical Eng., Serbia

Arkady Voloshin, Lehigh University, Bethlehem, USA

General information

Strojniški vestnik – Journal of Mechanical Engineering is published in 11 issues per year (July and August is a double issue).

Institutional prices include print & online access: institutional subscription price and foreign subscription €100,00 (the price of a single issue is €10,00); general public subscription and student subscription €50,00 (the price of a single issue is €5,00). Prices are exclusive of tax. Delivery is included in the price. The recipient is responsible for paying any import duties or taxes. Legal title passes to the customer on dispatch by our distributor.

Single issues from current and recent volumes are available at the current single-issue price. To order the journal, please complete the form on our website. For submissions, subscriptions and all other information please visit: <http://www.sv-jme.eu>.

You can advertise on the inner and outer side of the back cover of the journal. The authors of the published papers are invited to send photos or pictures with short explanation for cover content.

We would like to thank the reviewers who have taken part in the peer-review process.

The journal is subsidized by Slovenian Research Agency.

Strojniški vestnik - Journal of Mechanical Engineering is available on <http://www.sv-jme.eu>, where you access also to papers' supplements, such as simulations, etc.



Cover:

Acoustic Emission monitoring of a mold integrity during injection molding of polymer materials. Implementation of multi-dimensional feature vector with instances that are real-valued descriptors and with a use of neural network pattern recognition, the evaluation of the integrity of the mold with a high accuracy is possible in the appropriate multidimensional space.

Image courtesy:

LATOP – Laboratory for Heat treatment and Materials Testing, University of Ljubljana, Faculty of Mechanical Engineering, Slovenia

ISSN 0039-2480, ISSN 2536-2948 (online)

© 2018 Strojniški vestnik - Journal of Mechanical Engineering. All rights reserved. SV-JME is indexed / abstracted in: SCI-Expanded, Compendex, Inspec, ProQuest-CSA, SCOPUS, TEMA. The list of the remaining bases, in which SV-JME is indexed, is available on the website.

Contents

Strojniški vestnik - Journal of Mechanical Engineering
volume 64, (2018), number 11
Ljubljana, November 2018
ISSN 0039-2480

Published monthly

Editorial	655
Papers	
Tomoki Shiotani, Katsufumi Hashimoto, Hisafumi Asaue, Takahiro Nishida, Hidefumi Takamine, Kazuo Watabe, Masato Fukuda: Lateral Damage Identification in RC Slabs by Several Tomographic Approaches with Rainy Induced Elastic Waves	657
Tomaz Kek, Dragan Kusić, Rajko Svečko, Aleš Hančič, Janez Grum: Acoustic Emission Signal Analysis for the Integrity Evaluation	665
Bibi Intan Suraya Murat, Paul Fromme, Marco Endrizzei, Alessandro Olivo: Characterization of Impact Damage in Composite Plates	672
Adriana Savin, Nicoleta Iftimie, Rozina Steigmann, Dorin Rosu, Gabriel Silviu Dobrescu, Janez Grum, Paul Doru Barsanescu: Effective Methods for Structural Health Monitoring of Critical Zones of Scalable Wind Turbine Blades	680
Valentyn Uchanin, Sergej Minakov, Giuseppe Nardoni, Orest Ostash, Sergej Fomichov: Nondestructive Determination of Stresses in Steel Components by Eddy Current Method	690
Mariana Domnica Stanciu, Adriana Savin, Silviu Marian Nastac: Mechanical and Surface Properties of Lignocellulosic Fibres Reinforced Composites	698
Adriana Savin, Mihail Liviu Craus, Vitaly Turchenko, Frantisek Novy, Aura C. Mocanu, Marian Soare, Janez Grum, Oleksandr Sergiyovich Doroshkevich: Complementary Methods for Evaluation of Yttria Stabilized Zirconia Coatings used as Thermal Barrier Coating	706

Special issue:

Contemporary Non-destructive Testing and Monitoring in Engineering

The rapidly expanding role of Non-destructive Testing and evaluation methods applied in industries, as well as in basic research and development, has generated a large demand for practitioners, engineers, and scientists with knowledge of the subject. The Non-destructive Testing of materials has become important during the production process and even more important in in-service inspection where the state of the material is checked and further safe operation of the device or machine is confirmed.

The Slovenian Society for Non-destructive Testing and the Faculty of Mechanical Engineering (Laboratory for Heat Treatment and Materials Testing) are organizing periodic international conference titled: "Application of Contemporary Non-destructive Testing in Engineering". This international conference each time gathers experts from several countries all over the globe on the area of Non-destructive Testing and monitoring in engineering of production process. The lecturers discuss ultrasonic testing, electromagnetic, acoustic emission, thermal and infrared techniques and radiographic techniques, NDT education and training and other methods. It provides a forum for scientists, engineers and practitioners to review the latest developments and identifies particular needs and opportunities for further advances. Authors of the selected lectures were invited to prepare scientific papers for this issue of the Journal of Mechanical Engineering. The first selected paper presents novel method of rainy induced acoustic activity to identify damages of reinforced concrete slabs. This technique can be implemented for concrete bridge testing during in service inspection. In the following paper the evaluation of the integrity of injection molding tool based on AE signal acquisition

with resonant sensors is presented. The implemented signal processing offers detection of damage in the mold on line and prediction of process steps of injection molding. Third article presents independent characterization of the impact damage using three different NDE methods: X-ray imaging, ultrasonic immersion C-scan and guided ultrasonic waves. The following paper presents monitoring of scalable wind turbine blade carried out using complementary Non-destructive evaluation methods. Different types of sensors have been employed as optical fibre sensors, Fibre Bragg Grating type, wireless sensors based on metamaterials and classical strain gauges rosette placed on critical zones of the blade. In the fifth paper eddy current method for determination of stresses in ferromagnetic steel components based on magnetic anisotropy changes is implemented. The last two papers present mechanical and surface properties of lignocellulosic fibres reinforced composites and complementary methods for evaluation of yttria stabilized zirconia coatings used as thermal barrier coating.

The guest editors would like to acknowledge the contribution of the authors who submitted their work for publication in this special issue as well as the editor-in-chief Prof. Dr. Vincenc Butala and technical editor Mrs. Pika Škraba for professional, logistic and financial support.

Ljubljana, October 2018

Guest editors:

Asst. Prof. Dr. Tomaž Kek

Prof. Dr. Janez Grum

Lateral Damage Identification in RC Slabs by Several Tomographic Approaches with Rainy Induced Elastic Waves

Tomoki Shiotani^{1,*} – Katsufumi Hashimoto¹ – Hisafumi Asaue¹ – Takahiro Nishida¹
– Hidefumi Takamine² – Kazuo Watabe² – Masato Fukuda³

¹Department of Civil & Earth Resources Engineering, Kyoto University, Japan

²Toshiba Corporation, Japan

³West Nippon Expressway Company Limited, Japan

Efficient inspection techniques for ageing infrastructures are in great demand. In this study, rainy induced acoustic activity, which has so far been treated as a nuisance event for acoustic monitoring, is ambitiously utilized to identify damages of reinforced concrete (RC) slabs. Specifically, in-situ acoustic emission (AE) measurements of RC bridge slabs are conducted for a week. First, internal damages of the slabs are evaluated by both of AE activity and elastic wave velocity by means of AE monitoring and AE tomography. As for some representative locations showing each different damage estimated by the AE activity and the velocity, core samples are retrieved for the verification. In addition, AE activity induced by rain droplets in a short period of minutes are identified by an AE source location algorithm followed by computation on attenuation rate distribution. Through the evaluations, it was found that the distribution of AE sources induced by precipitation could reflect internal damage of RC slabs i.e., dense areas of source locations imply the intact or minor damage, while sparse areas of source locations suggest serious damage of RC decks. With this finding, the prompt decision making if the decks shall be replaced, repaired or left, which could not so far be readily implemented by other inspection techniques, would be reasonably conducted.

Keywords: acoustic emission, damage identification, raindrops, lateral damage, RC slabs

Highlights

- AE source distribution due to precipitation of rain induced elastic wave excitation, the serious damage as to be developed lateral cracks could be estimated for the low-density area of the distribution.
- The results of AE tomography with rainy induced AE activity was compatible to the results of AE tomography with using secondary AE activity generated inside of the RC deck.
- Attenuation rate distribution by means of AE tomography in this panel was also successfully computed to show the presence of lateral crack in the deck.
- It was also clarified that the distribution of attenuation rates by means of AE tomography could identify the damaged zones inside concrete.

0 INTRODUCTION

It is generally recognized that preventive and proactive maintenance works are necessary for such important infrastructure as bridges and tunnels. For reinforced concrete (RC) members, essential issues include establishing a maintenance system with the appropriate measures prior to the extensive damage and failure.

As a result of budgetary restrictions, preventive and proactive maintenance of infrastructure are desired, and thus inspections by non-destructive testing (NDT) methods providing early damage information must be applied. In terms of the damage assessment and estimation of repair and retrofit recovery in concrete structures, in addition to current NDT, innovative methods must be established.

The authors are thus studying tomography techniques based on elastic waves and acoustic emission (AE) to visualize three dimensional internal

defects in concrete. In AE tomography, past reports can be found in literatures [1] and [2]; however, as they did not consider diversion of wave propagation paths (hereafter referred to as ray paths), few successful results can be obtained. In consideration of the diversion of the ray paths, the basic analytical procedure and the applicability of these techniques have already been reported as elastic-wave tomography [3] and AE tomography [4] by authors.

Through the tomography technique, internal conditions are obtained using elastic wave parameters such as amplitudes and elastic wave velocities. This technique has been developed in the field of seismology and geophysics [5] to [7] as well as ultrasonic [8] to [10]. In this study, elastic wave velocity and attenuation rate are [11] used as the parameter. In elastic wave tomography, both the location of the excitation and the excitation time are known, whereas they are unknown for AE tomography. Specifically, the tomography can evaluate the elastic wave velocity

*Corr. Author's Address: Kyoto University, Katsura Campus, Nishikyo-Ku, Kyoto, Japan, shiotani.tomoki.2v@kyoto-u.ac.jp

and the attenuation rate in each set-element over the structure, which are theoretically associated with the modulus of elasticity. Because of the presence of such internal defects as cracks and voids, the elastic waves are reflected, diffracted, and scattered inside media with anomaly such as voids and cracks. The effect results in a decrease in elastic-wave velocity or energy. Thus, it can reasonably be assumed that the areas exhibiting lower elastic-wave velocity and higher attenuation rate correspond to those of serious deterioration. Accordingly, the distribution of wave velocities can be referred to as a good indicator of the internal condition of concrete structures.

1 AE ACTIVITY MEASUREMENT AND AE TOMOGRAPHY

1.1 Estimation of Wave Velocity Distribution

In in-situ RC Bridge decks, secondary AE activities, generated by friction among existing crack interfaces under traffic loads can be measured. Therefore, the evolutionary damage area can be visualized and specified when plotting AE sources through the measurement period; while the tomography can estimate internal velocity distributions of the structure, of which the velocity value can correspond to the quality of the concrete. The basic analysis procedure is shown as follows. Some AE sensors can record arrival time of elastic wave when the wave is generated by an AE source or artificial excitations such as hammering. After each arrival time is obtained, the propagation velocity through the propagation path of elastic wave is calculated by both of the distance from the excitation point to the receive point and T_{obs} (observed propagation time) which is obtained by Eq. (1):

$$T_{obs} = T_o - T_s, \tag{1}$$

where T_s is the excitation time and T_o is the arrival time. In the algorithm of the tomography, the inverse of velocity which is specifically referred to as the “slowness” is given as an initial parameter of each element as shown in Fig. 1. Next, T_{cal} (theoretical propagation time) is obtained, which is the total of the propagation time calculated by the slowness and the distance in each element (refer Eq. (2)), where s_j is the slowness of each element and l_j is the length crossing each element. ΔT is defined by observed propagation time (T_{obs}) and theoretical propagation time (T_{cal}) as shown in Eq. (3):

$$T_{cal} = \sum_j s_j \times l_j, \tag{2}$$

$$\Delta T = T_{obs} - T_{cal}, \tag{3}$$

Then the slowness in each element is revised in order to reduce ΔT . The slowness correction amount and the revised slowness are obtained by Eqs. (4) and (5), respectively:

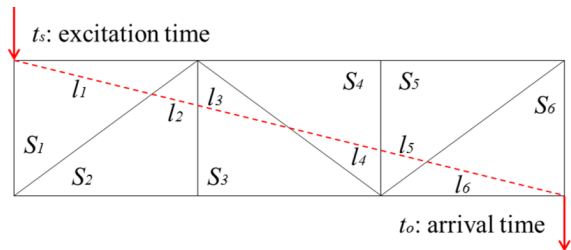


Fig. 1. Slowness for calculation of propagation time

$$\begin{bmatrix} \Delta s_1 \\ \Delta s_2 \\ \vdots \\ \Delta s_j \end{bmatrix} = \begin{bmatrix} \sum_i \frac{\Delta T_i \times l_{i1}}{L_i} / \sum_i l_{i1} \\ \sum_i \frac{\Delta T_i \times l_{i2}}{L_i} / \sum_i l_{i2} \\ \vdots \\ \sum_i \frac{\Delta T_i \times l_{ij}}{L_i} / \sum_i l_{ij} \end{bmatrix}, \tag{4}$$

$$s'_j = s_j + \Delta s_j, \tag{5}$$

where L_i is the total distance of the wave in the i th element. The iteration calculation from Eqs. (4) to (5) enables to obtain the accurate slowness and finally the velocity in each element corresponding to the observed propagation time of multiple waves over the structure, resulting in forming the tomogram of the elastic wave velocity over the target area. Through these steps, velocity distributions were determined in the structure. It is noted that in the AE tomography, the AE source identification and velocity distributions are both unknown and therefore they are calculated iteratively using AE tomography algorithm [12].

1.2 AE Measurement and Analysis

A real RC bridge deck was selected as a study target which has deterioration such as rebar corrosion due to salt attack and fatigue failure due to repeated mobile loads. The AE measurement was carried out with AE sensors, set on the bottom side of RC bridge decks. Resonant frequency of the AE sensor is 30 kHz, arranged on the RC deck as shown in Fig. 2.

Thickness of the RC bridge decks is 235 mm. Serious damage could be expected for the deck as large cracks with water leakage trace has been already observed. Threshold value of location uncertainty (LUCY) is set on 300 mm, about half space of two

adjacent sensors in this study. LUCY means source location accuracy and is the root-mean-square of the difference between calculated and observed distances between the source and the sensor [13].

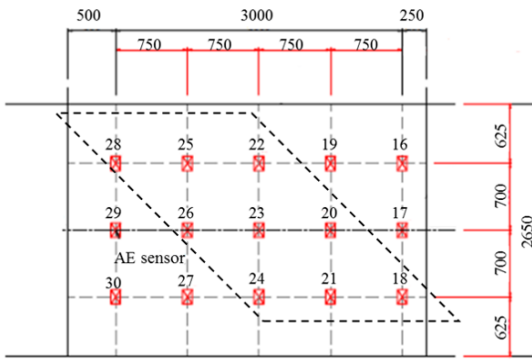


Fig. 2. Sensor arrangements for AE measurement on in-situ RC bridge decks

Dotted lines of parallelogram in Fig. 2 shows the cut-off specimen to study precise evaluation with the AE tomography, where three-dimensional analysis is carried out to estimate velocity distributions inside of the panel. AE sensor array for the tomography analysis is also shown in Fig. 3.

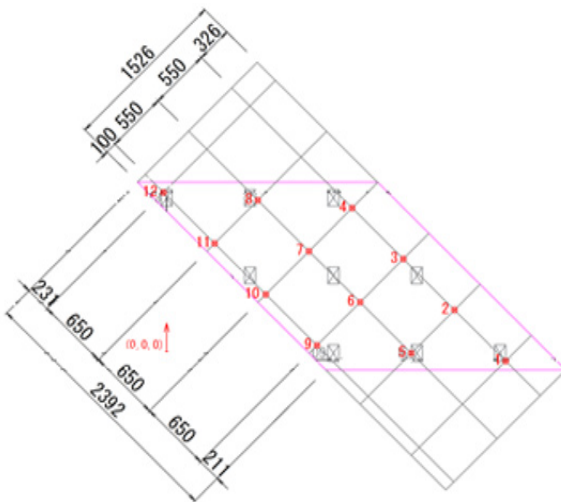


Fig. 3. Sensor arrangement in random hammering for AE tomography (Unit: mm)

1.3 AE Tomography

12 sensors of 60 kHz resonance were newly set on the bottom of panel. Random excitations with a hammer of a $\phi 11$ mm curvature edge were carried out for exciting elastic waves on the top surface of the panel. Appropriate input sources were carefully selected on

the following conditions: the case that the number of hits for an AE event is more than five by one hammering and the other is that LUCY is under 300 mm. As the results, the number of input sources for the tomography were 51. Results of AE tomography are shown in Fig. 4.

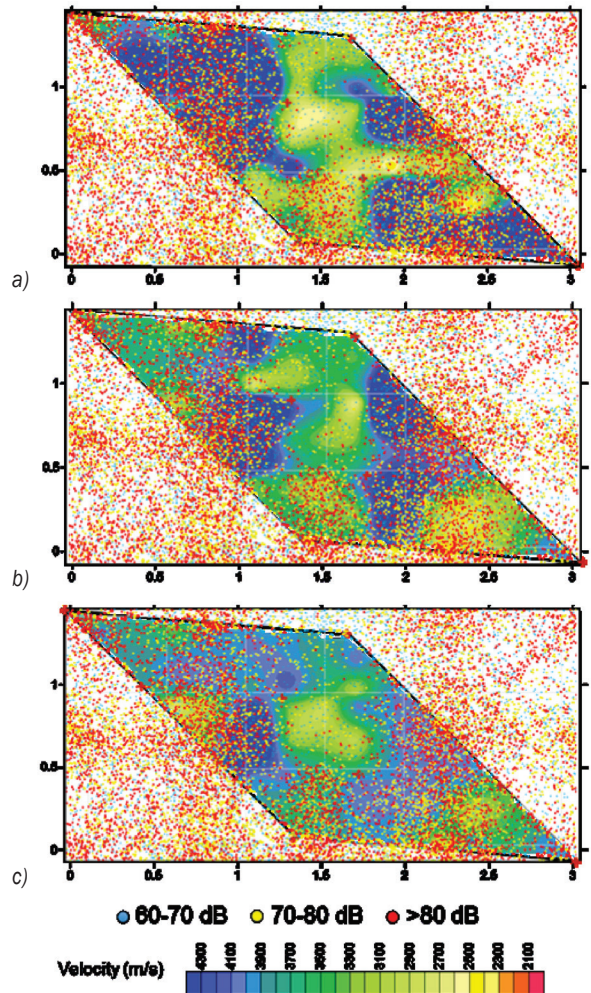


Fig. 4. Velocity distributions from the top to the bottom of RC deck with AE source location classified with peak amplitude of the first arrival of the AE hit; a) top layer, b) middle layer, c) bottom layer

In general, for the AE activity, the more intensive AE activity is obtained, the more damage than of less is expected in the media. As for the velocity, the area showing large velocity namely 4000 m/s suggests intact condition whereas small velocity of less than 3000 m/s roughly implies serious damage. As shown in Fig. 4, however, the area showing small velocity exhibits less AE activity while the area showing large velocity denotes the intensive AE activity. Some representative locations were subsequently selected,

and cores at those locations had been sampled and compared with the results both from the AE activity and the velocity. As a result, the followings were found: the area exhibiting small velocity with less AE activity showed serious damage existed inside of the deck, whereas intensive AE activity with large velocity suggested in damage progress condition, and less AE activity with large velocity implied intact condition [4].

2 RAIN-INDUCED AE ACTIVITY

2.1 AE Activity with Rain Drops

AE hits per half an hour for 135 hours is shown in Fig. 5. An intensive AE activity were acquired from 120 to 130 hours. Besides, rain droplets are also known as a factor generating AE activity when it impacts on a solid material [14]. As considered factors of AE activity in the panel, some of the AE activity, shown in Fig. 5, might be generated as the resultant impacts of rain droplets on the surface of RC deck.

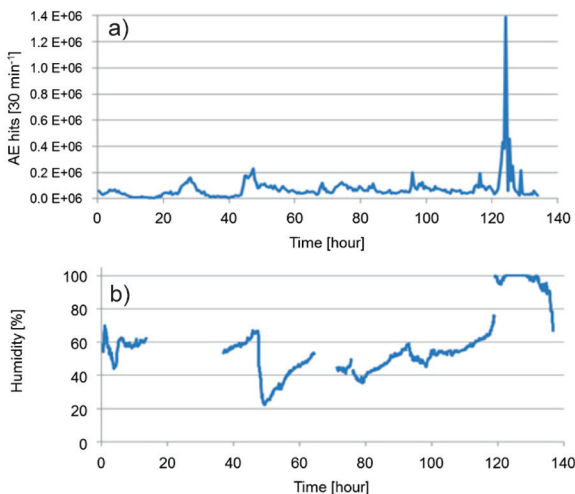


Fig. 5. a) AE activities and b) relative humidity during a measurement period

To clarify the fact of precipitation, relative humidity at the bridge is shown as in Fig. 5 as well as AE activity. After 120 hours, humidity increased to 100 % accompanied with the high AE activity. In the weather record, precipitation was also confirmed at that period. Thus, the intensive AE activities is considered to be caused by heavy rainfall. It indicates that the impacts of raindrops on the road surface caused AE activity, and some AE events reached the sensors attached on the bottom surface of the deck. Those concentrated AE activities was neither to

correlate to the traffic load nor to be considered as a result of existing cracks inside the bridge decks. Therefore, those signals are in general considered not to reflect the deterioration of the deck, leading to be treated as noise. However, a unique distribution of AE sources induced by these rain droplets was found, the following discussion would be developed to inspect the bridge decks.

2.2 Source Location of Rainy Induced AE Hits

The AE data was extracted during the intensive rain and analyzed for the source locations. Fig. 6 shows the source locations of the measured panel. Here, the source locations considered to have low reliability has been filtered out. Enough amounts of AE sources were obtained only for 700 seconds. In the figure, a low-density area surrounded by dashed lines can be confirmed on the panel. As the random AE events by the precipitation shall be resulted in uniform distribution of AE sources over the bridge deck; however, non-uniformity of the source distribution exhibiting an empty area of the source distribution is obvious, and therefore this low-density area is attributed from extremely high attenuation of AE wave propagation in the propagation media, suggesting the suspect to be heavily deteriorated. In consideration of velocity distribution as well as visual inspection by actually excavated core samples it has been concluded that the area of less AE activity accorded well to the laterally damaged or cracked locations. Accordingly, it was found that rainy induced AE activity had a potential to determine the area of serious deterioration in the concrete decks.

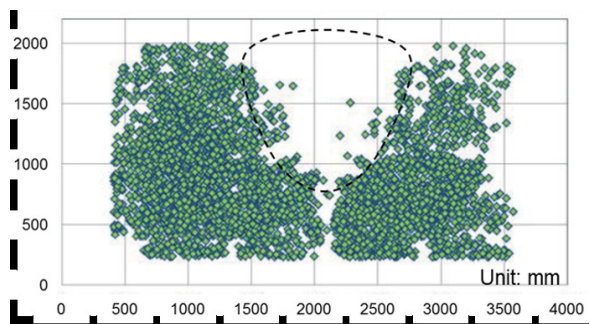


Fig. 6. Result of AE source location analysis

Specifically, by calculating the AE source locations, the density of the AE sources would reveal the damage condition inside the deck. In addition, since all AE sources generated by raindrops are on the same surface of the road surface, instead of 3D,

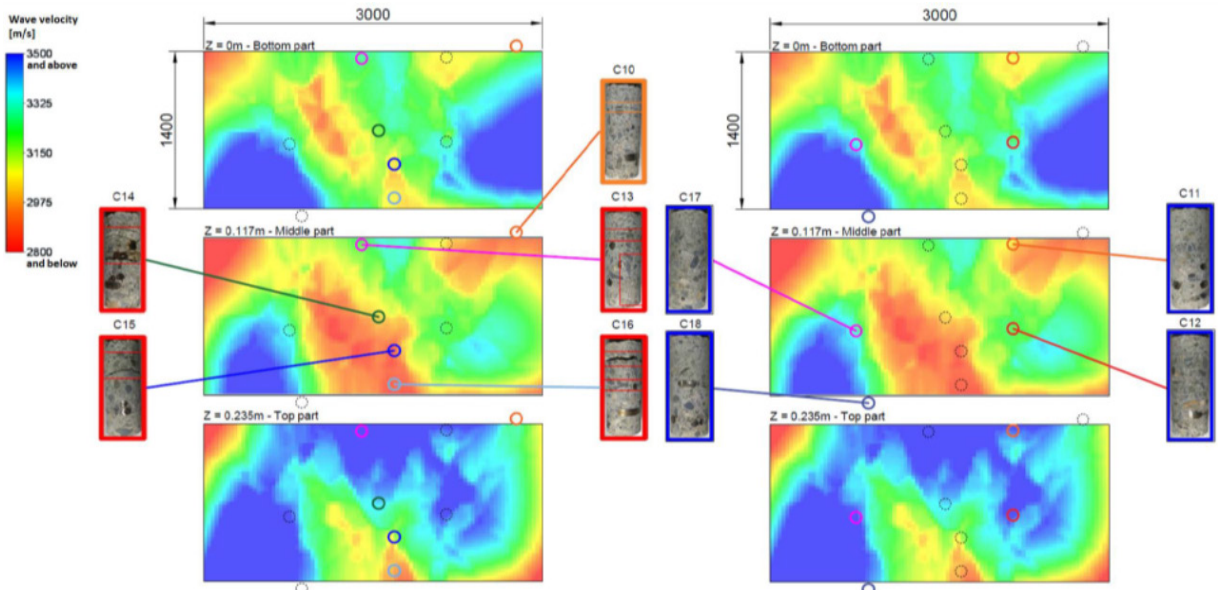


Fig. 7. Comparison between the tomograms and the core samples

simple 2D source locations can be readily conducted. As the short-term heavy rain could generate a large amount of AE hits on the road, providing reasonable interpretation on the specification of the internal damage, the damage assessment of the decks induced by rain droplets has thus a great potential to realize in-situ damage inspection with great efficiency.

2.3 AE Tomography with Rainy Induced AE Activity

As expected, a sufficient number of rainy induced AE events has been obtained, the wave velocity distribution by means of AE tomography in this panel has also been conducted using rainy induced AE sources and the results are presented in Fig. 7 with core samples taken out from the deck to verify the results. The deck after core excavation can be found as in Fig. 8.



Fig. 8. Positions of core samples

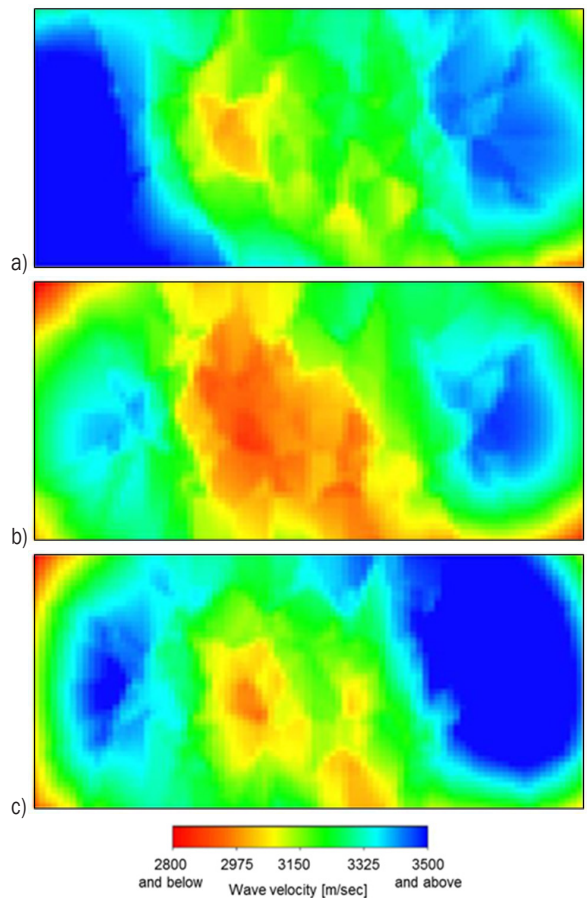


Fig. 9. AE tomography results with internal AE activity: a) $z = 0$ mm (bottom surface), b) $Z = 117$ m (middle layer), c) $Z = 235$ m (top surface)

As shown in Fig. 7, the lateral damage was observed in the cores showing small velocity and vice versa. Nevertheless, this is not exactly true for the core samples C11 and C13 which are both located at the border between a low velocity zone and a medium velocity zone. These small inaccuracies may simply be caused by the fact that the fineness of the mesh determining elements of analysis does not allow for such a precise evaluation or secondary damage produced during cut-off work.

The velocity distributions obtained by using internal AE events is shown in Fig. 9 for the comparison to that obtained by using rainy induced AE events as found in Fig. 7. The tomogram obtained by means of rainy induced AE events, is almost compatible to that obtained by the internal AE events, suggesting AE events produced by the precipitation in a short-term provides a reasonable tomogram result, being equivalent when using secondary AE events in a long-term.

2.4 Attenuation Tomography

As the computation for the elastic wave ray-trace algorithm considering all potential detours of elastic waves takes up much time, hereafter a straight line of P-wave propagation is assumed in the tomography analysis via the attenuation-rate distribution to identify the lateral cracks in RC slab. The data processing flow is shown as in Fig. 10 so as to extract meaningful AE events. As in the figure, first, the source locations of all AE events are used as input, where a constant wave velocity [m/s] and attenuation-rate [dB/m] across the tested member is assumed for calculation. Second, the amplitude and the excitation time at the source of the considered AE event are estimated on the basis of the arrival times and the amplitudes recorded by the sensors. Third, the attenuation rates along all straight ray-paths between the source and the receiving sensors are computed.

For each AE event, the peak amplitude of the elastic wave at the source is unknown. Consequently, it can be approximated to calculate the attenuation rate along the considered wave paths. In the attenuation tomography algorithm, they are generally estimated from a relation represented in Fig. 11 (the distance in logarithmic scale is used in general). The peak amplitude of the signal recorded by each sensor is plotted as a function of the distance between the source and the sensors. A linear regression between the peak amplitude of the elastic wave and the distance from the source is computed. The peak amplitude at

the source is referred to as equal to the value for the case that the distance is equal to zero.

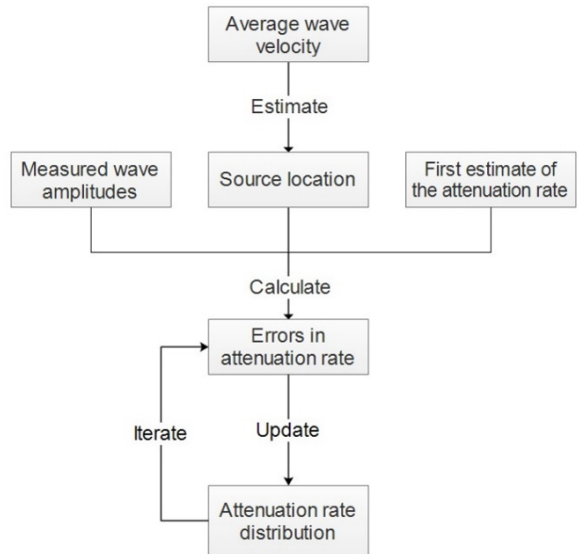


Fig. 10. Flow chart to compute attenuation tomography

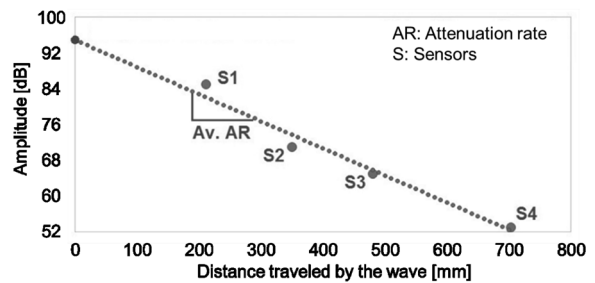


Fig. 11. Estimation of the peak amplitude of the elastic wave at the source

Tomography computation is carried out based on elastic wave parameters with the attenuation rate in this paper. In the tomography based on the attenuation, the area of interest and analysis must be divided into mesh elements characterized by their own attenuation rates. Then, a first estimate on distribution of the attenuation rates is to be provided as input. By comparing those values along each wave path to its calculated value of the assumed distribution, the SIRT algorithm [15] could lead to proper distribution of the attenuation rates. The measured travel time and attenuation rate along each ray path is estimated from Eq. (6).

$$AR_{measured,i} = \frac{A_{source} - A_{sensor,i}}{\sum_j^{N_i} d_{i,j}}, \quad (6)$$

where $AR_{measured,i}$ is measured average attenuation rate along the wave path from the source to the i^{th} sensor,

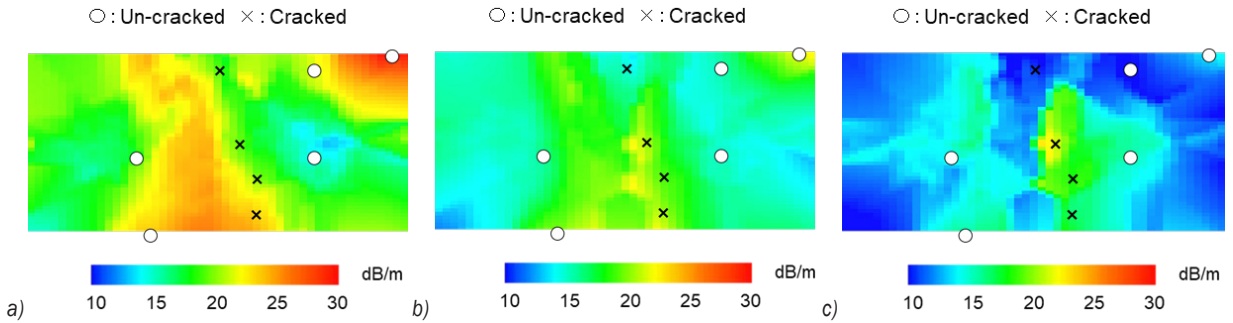


Fig. 12. Attenuation rate distributions; a) $z = 0$ mm (bottom surface), b) $Z = 117$ m (middle layer), c) $Z = 235$ m (top surface)

A_{source} estimated peak amplitude of the elastic wave associated to the considered AE event at its source, $A_{receiver,i}$ peak amplitude of the elastic wave measured at the i^{th} sensor, N_i mesh number of elements crossed by the wave path from the source to the i^{th} sensor, and $d_{i,j}$ length of the wave path from the source to the i^{th} sensor in the j^{th} element.

Second, the attenuation rate along each wave path based on distribution of the attenuation rates in the mesh elements is computed by Eq. (7).

$$AR_{calculated,i} = \frac{\sum_j^M AR_j \cdot d_{i,j}}{\sum_j^M d_{i,j}}, \quad (7)$$

where $AR_{calculated,i}$ is calculated average attenuation rate along the wave path from the source to the i^{th} sensor [dB/m], AR_j attenuation rate in the j^{th} element [dB/m], and M mesh number of elements crossed by the ray path from the source to the i^{th} sensor.

Afterwards, the difference between the measured and the calculated attenuation rates is calculated for each wave path by using Eq. (8).

$$\Delta AR_i = AR_{measured,i} - AR_{estimated,i} \quad (8)$$

In a similar manner to Eq. (1), the differences of the attenuation rates on all the wave paths are estimated by Eq. (9).

$$\Delta AR_j = \frac{\sum_{i=1}^N \Delta AR_i \cdot d_{i,j}}{\sum_{i=1}^N d_{i,j}}, \quad (9)$$

where N is the number of wave paths crossing the j^{th} element. The attenuation rate in each element is then updated with Eq. (10).

$$AR_{j,updated} = AR_j - \Delta AR_j \quad (10)$$

The procedure from Eq. (7) through Eq. (10) is repeated until the convergence is reached.

The attenuation rate distribution by means of AE tomography, as explained above, in this panel has been successfully computed in Fig. 12 with conditions' observation by sampled cores. The lateral cracks were located at 150 mm or less from the surface of the deck (mostly in the top layer) by visual inspection of the cored samples [16]. Therefore, it is reasonably understood that attenuation rate in top layer are lower than bottom layer. The soundness of concrete and the presence of lateral crack roughly correspond to the attenuation rate distribution. In this study, the attenuation rate inside the core samples presenting large lateral cracks are generally higher than 20 dB/m at least over a certain part of their depth.

3 CONCLUSIONS

The elastic waves generated by the rain droplets could be an AE activity contributing to the AE tomography. The results of AE tomography with rainy induced AE activity in a short term was compatible to the results of AE tomography with using secondary AE activity generated inside of the concrete deck in a long term. With the AE source distribution due to precipitation, the serious damage as to be developed lateral cracks could be estimated for the low-density area of the distribution. It is also clarified that the distribution of attenuation rates by means of AE tomography could identify the damaged zones inside concrete. With these findings, the prompt decision making if the decks shall be replaced, repaired or left, which could not so far be readily implemented by other inspection techniques, would be reasonably conducted.

4 ACKNOWLEDGEMENTS

A part of this study was commissioned and supported by New Energy and Industrial Technology Development Organization (NEDO).

5 REFERENCES

- [1] Katsuyama, K., Seto, M., Kiyama, T., Utagawa M. (1992). Three dimensional AE tomography for image processing of the deteriorated material. *Safety Engineering, JSSE*, p. 321-326. (in Japanese)
- [2] Schubert, F. (2004). Basic principles of acoustic emission tomography, *DGZfP, Proceedings BB 90- CD, EWGAE 2004*, Lecture 58.
- [3] Shiotani, T., Aggelis, D. G., Momoki, S. (2009). Elastic wave validation of large concrete structures repaired by means of cement grouting. *Construction and Building Materials*, vol. 23, p. 2647-2652, DOI:10.1016/j.conbuildmat.2009.01.005.
- [4] Asuae, H., Shiotani, T., Nishida, T., Watabe, K., Miyata, H. (2016). Applicability of AE tomography for accurate damage evaluation in actual RC bridge deck. *Structural Faults & Repair Conference*, no. 1743 (CD-ROM).
- [5] ISRM (1988). *Suggested Methods for seismic testing within and between boreholes. Seismic Testing Suggested Methods*, p. 449-472.
- [6] Saito, H. (1989). Travel times and raypaths of first arrival seismic waves: Computation method based on Huygens' Principle, *59th Annual International Meeting, Society of Exploration Geophysicists*, Expanded Abstracts, p. 244-247.
- [7] Saito, H. (1992). Characteristics of the first arrival travel time curves obtained by crosshole seismic measurements. *Proceedings of the 86th SEGJ Conference*, p. 88-93.
- [8] Kak, A.C., Slaney, M. (1998). *Principles of Computerized Tomographic Imaging*, IEEE Press, New York.
- [9] Schechter, R. S., Mignogna, R. B. and Delsanto, P. P. (1996). Ultrasonic tomography using curved ray paths obtained by wave propagation simulations on a massively parallel computer. *Journal of Acoustic Society of America*, vol. 100, no. 4, p. 2103-2111, DOI:10.1121/1.417920.
- [10] Mignogna, R.B., Delsanto, P.P. (1996). A parallel approach to acoustic tomography. *Journal of Acoustic Society of America*, vol. 99, no. 4, p. 2142-2147, DOI:10.1121/1.415401.
- [11] Chai, H.K., Momoki, S., Kobayashi, Y., Aggelis, D.G., Shiotani, T. (2011). Tomographic reconstruction for concrete using attenuation of ultrasound, *NDT&E International*, vol. 44, no. 2, p. 206-215, DOI:10.1016/j.ndteint.2010.11.003.
- [12] Kobayashi, Y., Shiotani, T. (2012). Seismic tomography with estimation of source location for concrete structure. *Structural Faults and Repair 2012*, (CD-ROM).
- [13] Hamstad, M.A. (2007). Acoustic emission source location in a thick steel plate using lamb modes. *Journal of Acoustic Emission*, vol. 25, p. 194-214.
- [14] Shiotani, T. (2006). Evaluation of long-term stability for rock slope by means of acoustic emission. *NDT&E International*, vol.39, p. 217-228, DOI:10.1016/j.ndteint.2005.07.005.
- [15] Tranmpert, J., Leveque, J.J. (1990). Simultaneous iterative reconstruction technique: physical interpretation based on the generalized least squares solution. *Journal of Geophysical Research*, vol. 95, no. B8, p. 12553-12559, DOI:10.1029/JB095iB08p12553.
- [16] Takamine, H., Watabe, K., Miyata, H., Asuae, H., Nishida, T., Shiotani, T. (2016). Efficient damage inspection of deteriorated RC bridge deck with rain-induced AE activity. *Proceedings of IAES-23, IIIAE 2016, Kyoto and ICAE 8*, p. 231-236.

Acoustic Emission Signal Analysis for the Integrity Evaluation

Tomaž Kek^{1,*} – Dragan Kusić² – Rajko Svečko³ – Aleš Hančič² – Janez Grum¹

¹ University of Ljubljana, Faculty of Mechanical Engineering, Slovenia

² TECOS Slovenian Tool and Die Development Centre, Slovenia

³ University of Maribor, Faculty of Electrical Engineering and Computer Science, Slovenia

This paper presents measurements of acoustic emission (AE) signals during injection molding with resonant PZT sensors that were applied to the mold via waveguides. A polypropylene material was employed for injection molding of ISO specimens. Acoustic signals were measured during production cycles on a new mold and damaged one with cracks induced by laser surface heat treatment. The mold inserts integrity description by acquired AE signal together with the fractal algorithm using box counting method is presented. Implementation of AE signal analysis based on an idea of the box-counting method in a way to divide the measured AE signals to AE signal boxes is used. To improve the capability of clustering AE data during injection process cycle, AE burst descriptors are defined. To lower computational complexity and increase performance, the feature selection method was implemented. Neural network pattern recognition of AE signals feature subsets was used for evaluation of process steps and damage detection.

Keywords: injection molding, acoustic emission, cracks, box counting method, pattern recognition

Highlights

- A method is presented able to evaluate integrity of injection molding tool based on signal acquisition with resonant sensors.
- Different aspects of signal analysis of acquired acoustic signals of a steel insert are used for integrity evaluation.
- Implementation of signal analysis based on idea of box counting method in a way to divide the measured acoustic signals to signal boxes is used.
- Implemented signal burst analysis with burst descriptors improves the capability of clustering the measured data during injection cycle. To lower computational complexity and increase performance of the evaluation, the feature selection method was implemented.

0 INTRODUCTION

Injection molding process is very popular manufacturing process for production of plastic products. It offers production of complex shaped products with high tolerance requirements which is especially difficult with combination of different polymer material. Typical production cycle usually incorporate mold closing followed by injection of molten material into a cavity. After filling the cavity, the packing pressure is applied to compensate for the material shrinkage. Product has to be sufficiently cooled for mold opening and ejection of the part.

The major acoustic signal sources detected by nondestructive testing (NDT) are crack growth and plastic deformation of the steel [1]. Acoustic inspection offers determination of location and propagation of a crack during loading as already reported by many researchers that are working in various fields. Acquisition of acoustic emission (AE) signals during different production processes in different setups has become widely used because of high sensitivity and usefulness for online surveillance [2] to [4]. Cao et al. [5] investigated acoustic signals during four-point bending fatigue crack propagation in steel. In the first stage of fatigue damage process a dominant acoustic source was micro-crack initiation.

During intermediate stage of crack growth, stacking and slipping of dislocations ahead of the crack tip are major acoustic sources. During final stage the predominant acoustic sources are shearing of ligaments and connectivity between dimples. They have set neural network model with input time domain parameters based on burst energy, peak amplitude, duration, and counts. Mukhopadhyay, et al. [6] analyzed these signals during fracture toughness tests with a compact tension (CT) specimens made of steel. During fracture toughness tests the signals have been attributed to the plastic zone formation at the crack tip and initiation and/or extension of crack. Drummond et al. [7] analyzed enhancement of proof and fatigue testing procedures for wire ropes with incorporation of measurement of AE signals. The results of their research showed that the most effective AE signal discriminators are peak amplitude and (cumulative) burst energy for differentiation between signals from wire breaks and other sources. For determination of the rope's condition there is no need for continuous monitoring and also measurement of AE is indicative of the level of damage of the rope. Kim et al. [8] measured fatigue crack growth with standard CT specimens using a hydraulic loading machine. The result of their research was the development of a neural network based model used for the prediction

*Corr. Author's Address: University of Ljubljana, Faculty of Mechanical Engineering, Aškerčeva 6, 1000 Ljubljana, Slovenia, tomaz.kek@fs.uni-lj.si

of stress intensity factor based on five parameters of acoustic emission signals (peak amplitude, energy, ring down count, rise time and event duration). Their results showed gradual increase of AE energy with the number of fatigue cycles. Change in the acoustic emission energy with the number of fatigue cycles was an effective parameter for estimation of the activity of the crack propagation and the stress intensity factor.

Acoustic emission monitoring offers a big potential for detailed in situ failure analysis of different materials. Measurement of AE signals provides information on sub-macroscopic failure phenomena and also on the overall damage accumulation [9] to [11]. Measured AE signals contain useful information on the damage mechanism in a broad spectrum of applications [12]. Measurement of AE signals during production processes or during loading of different structures usually generates a high number of detected signals. These signals can be associated to a patterns (vectors) composed of multiple relevant descriptors [13] to [16] with the intention to discriminate different damage mechanisms described with clusters. The patterns (vectors) can be classified into clusters according to their similarity by the use of multivariable data analyses based on pattern recognition algorithms [17]. Piezoelectric (PZT) sensors are usually used for inspection. They can measure ultrasound with a high sensitivity (~ 1 V/nm) as a displacement sensors and a few V/(mm/s) as a velocity sensors. Since they are sensitive only on dynamic events they automatically compensate low-frequency motion of measuring objects that can be caused by environmental vibrations.

Low-frequency cutoff of PZT sensors is a consequence of the leakage of the accumulated charge and acts as a high-pass filter. The low-frequency cutoff is determined through a time constant given by the capacitance and resistance of the device [18]. Additionally to above mentioned advantages, PZT sensors are also insensitive to electromagnetic fields and radiation, enabling measurements under harsh conditions.

1 METHODS

Correlation of crack propagation in steel and basic acoustic burst signal parameters is well described in the literature but on the other hand the detection of tool damage in the literature didn't gained sufficient coverage in the past.

In this paper different aspects of mold (tool insert) integrity based on acquired AE signals are presented. In the section 3.1 description of tool insert integrity

by time domain acoustic signal descriptors together with fractal algorithm using box counting method is presented. Section 3.2 describes implementation of acoustic signal analysis based on idea of box counting method in a way to divide the measured signals to "signal boxes". Prediction of the tool insert damage is based on signal frequency characteristics and signal amplitude probability distribution into the decision criteria. The signal box can be an aggregate of information that is described by individual bursts. Section 3.3 then describes the analysis of acquired acoustic signals in a form of bursts. The burst descriptors are stacked to form a feature (measurement) vector Z . After signal processing neural network pattern recognition of bursts during the full time of the injection molding cycle is presented.

2 EXPERIMENTAL

For injection molding one cavity tool for production of square test specimens with dimensions of 60 mm \times 60 mm \times 2 mm was used. These specimens can be used for variety of tests according to ISO 294-3 standard [19]. For injection molding a polypropylene (PP) material isofil H40 C2 F NAT manufactured by Sirmax was used. Fig. 1 shows the used KraussMaffei KM 80 CX-SP 380 injection molding machine on which a mold with a steel mold insert made of OCR12VN steel is placed. Experiments were conducted using a new tool and a damaged tool, respectively. For generation of surface cracks on a damaged mold local laser surface hardening of the tool steel was used. Experiments were conducted on injection molding machine KraussMaffei KM 80 CX-SP 380 with application of a broad spectrum of



Fig. 1. The used injection molding machine KraussMaffei KM 80 CX-SP for experimental trials

injection molding process parameters. For acoustic measurements Vallen AMSY-5 system was used with two resonant piezoelectric AE sensors VS150-M with a measuring range between 100 kHz and 450 kHz and resonance at 150 kHz. Sensors are connected via AEP4 preamplifiers with a gain of 40 dB. These sensors cover frequencies spectrum that is characteristic for the signals generated during fatigue and plastic deformation [20]. For measurement an 18-kHz high pass filter was used. The amplitude threshold was set at 40 dB and sampling frequency to 5 MHz. To protect sensors against high temperatures, fumes exhaled out of the mold and to prevent mechanical damage during operation by the operator, additional waveguides were used.

3 RESULTS AND DISCUSSION

3.1 Burst AE Signals during Injection Molding Production Cycle

Acoustic emission testing can detect dynamic processes associated with the degradation of structural integrity. During injection molding process a rapid increase of pressure during the filling and holding stage in mold occurs. This can stimulate defects in the mold that can result in release of AE signals in the form of burst.

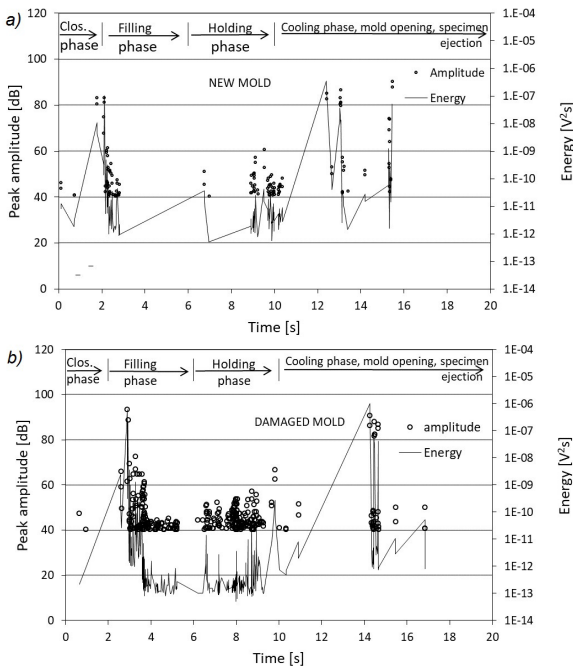


Fig. 2. Peak amplitudes and energy of AE bursts during the manufacturing of test specimens produced with a) the new and b) damaged mold

Basic AE parameters as peak amplitudes and energy of AE bursts measured during the production cycle of injection molding is shown on Fig. 2a and b for new mold and damaged mold. With a new intact mold absence of cracks offers us classifying detected acoustic signals as process orientated signals. Presence of damage in mold causes a considerable increase in the number of bursts especially during the filling and holding phase of the production cycle. Additional signals during these stages can consequently, be connected to active AE sources from mold defects. A rapid increase and high pressure in mold can stimulate plastic zone formation, slipping and stacking of dislocations in front of the crack tip and crack extension that can cause distinctive AE bursts [5], [6] and [21].

AE signal processing for evaluation of the defect in the injection mold can be achieved with fractal algorithm using box counting method. With this method acquired acoustic emission during injection molding cycle can be considered as time discrete signal. With setting time leg, also called ruler with different dimensions, the whole temporal window can be divided in an integer number of rulers (Fig. 3). Whenever the time leg μ contains a burst with the amplitude above the specified threshold, we can add 1 to the counter $G(\mu)$. Richardson's diagram incorporates interpolation line of $G(\mu)$ versus μ in a log-log diagram. Absolute value of the $\tan(\varphi)$ can be called fractal dimension that can be used as damage parameter.

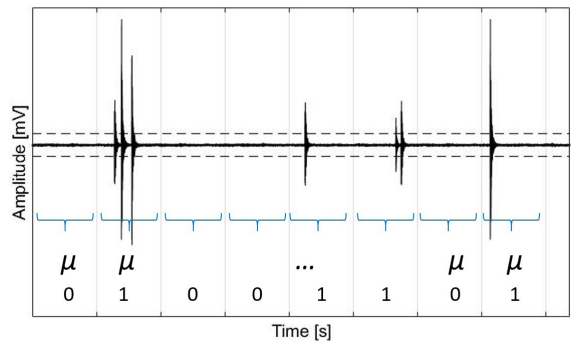


Fig. 3. Temporal window of acquired acoustic emission can be divided in an integer number of rulers

Fig. 4 shows that the presence of damage in the mold influences the slope of the interpolating line at a box counting method (BCM). Interpolated line designated as process is calculated according to the time discrete signal measured during the injection molding cycle with a new mold whilst interpolated line designated as process + damage describes

injection molding cycle with a damaged mold. With a use of neural network pattern recognition captured AE burst can be classified into classes and signals connected with a damage, can be extracted. More about that will be described in the chapter 3.3. If we extract signals connected with damage in the mold we can calculate interpolated line designated as damage.

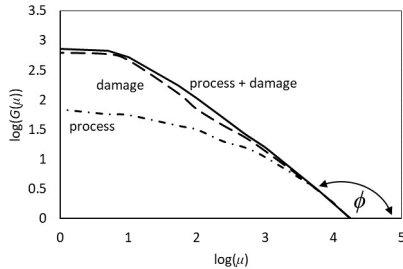


Fig. 4. Richardson's diagram for a new mold and damaged mold

3.2 Analysis of Acquired Signals with Defined Time Length (AE Signal Boxes)

The decision about the acceptability of a damaged mold with a small crack based basic AE parameters, burst rate and cumulative number of signal bursts is difficult. It is therefore reasonable to introduce additional features of detected signals during the production cycle in a form of acoustic signal frequency characteristics and amplitude probability distribution.

In our research we used the idea of box counting method in a way to divide the measured signals to "signal boxes" with defined time length (duration). Definition of signal boxes with defined time duration reduces computational complexity. For signal boxes we defined time length of 52.4 ms to cover also long bursts or burst cascades expected during cycle. Signal box represents signal vector $\mathbf{X} = (x_1, x_2, \dots, x_n)$ where

$n = 262144$. We used 3.2 ms rearm time and 3.1998 ms duration discriminant time.

For signal boxes we calculated power spectrums using fast Fourier transform (FFT) with adjusted amplitude values below 1 unit and a frequency step of 19 Hz. FFT is the most popular method for spectral analysis in digital signal processing [22] and [23]. Power spectral density is a measure of energy at various frequencies and is calculated based on FFT and the complex conjugate of FFT. We used Eq. (3) to calculate the P_L parameter to characterize the lower part of the power spectrum ($a = 90$ kHz, $b = 190$ kHz). The higher part of power spectrum ($a = 250$ kHz, $b = 350$ kHz) is characterized with parameter P_H , while P_S covers all power spectrum frequencies ($a = 50$ kHz, $b = 550$ kHz). The parameters P_L , P_H and P_S give information about the energies at various frequencies inside of measured frequency spectrum.

$$g_i = \frac{\overline{y_i y_i}}{m}, \tag{1}$$

$$m = \max(\mathbf{Y} \cdot \overline{\mathbf{Y}}), \tag{2}$$

$$P_L = \sum_{a=90}^{b=190} g_i. \tag{3}$$

In above equations $\mathbf{Y} = (y_1, y_2, \dots, y_n)$ is the vector of discrete Fourier transform using FFT.

Additional parameters describing the amplitude distribution of recorded signals like the kurtosis K and skewness S were introduced to improve the prediction of mold integrity. K is a measure of the "peakedness" of the probability distribution while S is a third central moment and is a measure of asymmetry about the mean amplitude value of \mathbf{X} .

We have set 5-dimensional feature vector with real-valued explanatory variables $\mathbf{V} = (P_H, P_L/P_H, P_L/P_S, K, S)$. \mathbf{V} represents points in appropriate multidimensional space and offers characterization

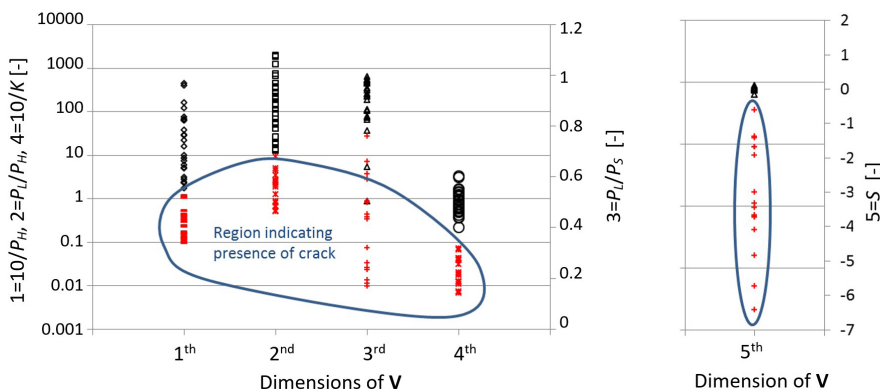


Fig. 5. Damaged mold definition based on feature vector V

of the process. Fig. 5 show characterization of the injection molding (IM) process regarding the presence of mold defects. Hollow black markers represent vectors \mathbf{V} during production using the new and damaged mold, where the mold pressure is relatively low and is below activation level of defects in the tool steel. Red markers ($-$, \times , $+$ and $*$) on Fig. 5 represent the vectors \mathbf{V} during production with the damaged mold, where the mold pressure is above the activation level of defects in the steel. Vectors \mathbf{V} that indicate the presence of damage are positioned in encircled region.

Definition of signal boxes with defined time duration reduces computational complexity during measurement and simplifies the analysis of acquired signals during monitoring. For example in a case of injection molding individual AE signal box can simultaneously carry information closely linked with a process step together with the information of injection mold integrity. AE signal box can thus represent mixture of information that can be with an individual AE signal burst analysis additionally dismembered.

3.3 Burst Analysis

Above mentioned disadvantage of the signal boxes analysis that can simultaneously carry information closely linked with a process step together with the information of mold integrity can overcome signal burst analysis. Within the scope of this method we used signal bursts for derivation of signal descriptors that are stacked to form a feature vector $\mathbf{Z} = (z_1, z_2, \dots, z_{73})$. The union of feature vectors is acquired during different phases of process. Together with already described features that represent signal frequency characteristics and signal amplitude probability distribution in feature vector \mathbf{V} in paragraph 3.2, additional time-domain features are added in a feature vector \mathbf{Z} , like A_p , (peak amplitude), R_t (rise time), d (duration) and RA value (ratio of R_t nad A_p). To overcome pitfalls of Fourier analysis, Wavelet analysis is applied for processing signals during cycle. The wavelet packet analysis decomposes signal into several levels in the whole measured frequency band [24] and [25]. To improve frequency resolution the detail of the signal is decomposed as well [26]. The wavelet packet corresponds to some frequency band and includes information on signal in different time windows at different resolutions. For the analysis some packets contain important information while other packets are relatively unimportant.

For the computation of wavelet packet transform of signal $X(t)$ we used algorithm described below:

$$P_0^1(t) = X(t), \tag{4}$$

$$P_j^{2^{i-1}}(t) = HP_{j-1}^i(t), \tag{5}$$

$$P_j^{2^i}(t) = GP_{j-1}^i(t). \tag{6}$$

In above equations $P_j^i(t)$ represents i^{th} packet on j^{th} resolution, with time parameter $t=1, 2, \dots, 2^{J-j}$, $i=1, 2, \dots, 2^j$, $j=1, 2, \dots, J$, $J=\log_2 N$. Operators H and G are convolution sum defined as:

$$H\{\cdot\} = \sum_k h(k-2t), \tag{7}$$

$$G\{\cdot\} = \sum_k g(k-2t). \tag{8}$$

In above equations $h(t)$ and $g(t)$ are a pair of quadrature mirror filters. A time parameter t is taken as a series of integers k ($t \rightarrow k = 1, 2, \dots$).

To define the energy of wavelet packet we used:

$$E_j^i = \sum_{t=1}^{2^{j-i}} (P_j^i(t))^2. \tag{9}$$

The energy of wavelet packet on selected resolution j is normalized as:

$$R_j^i = E_j^i / \sum_{i=1}^{2^j} E_j^i. \tag{10}$$

For the description of AE bursts we have set the feature vector $\mathbf{Z} = (P_H, P_L/P_H, P_L/P_S, K, S, A_p, R_t, RA, d, R_5^1, R_5^2, \dots, R_5^{32}, E_5^1, E_5^2, \dots, E_5^{32})$.

But the dimension of feature vector should not be arbitrary large. Large vectors increase computational complexity, and causes a decrease of performance [27]. A small set of features can also give us satisfactory classification performance. Feature selection method offers selection of subset $F_j(B) = \{z_b \mid b = 1, \dots, B\}$ which surpass other subsets with dimension B as:

$$J(F_i(B)) \geq J(F_j(B)) \text{ for all } j \in \{1, \dots, q(B)\}, \tag{11}$$

where $q(B)$ is the number of evaluations of performance measure $J(F_j(B))$. For reduction of dimension of feature vector we have applied sequential forward selection (SFS) method with k -Nearest Neighbor (k -NN) classification algorithm. With k -NN the input consists of the $k = 3$ closest training examples in the feature space.

SFS method offered us selection of feature subset \mathbf{Z}_s with a size of 10. \mathbf{Z}_s is an input for neural network pattern recognition of acquired bursts during the IM production cycle. The most informative selected features based on SFS are stacked in feature subset as follows: $\mathbf{Z}_s = (R_5^8, R_5^{16}, R_5^{24}, R_5^{21}, R_5^{18}, R_5^{20}, d, R_5^6, R_5^{32}, A_p)$. Vectors of the training data have been designated into

categories based on the time moment of their acquisition during the injection molding cycle and unsupervised fuzzy C means clustering (FCM) for vectors of the damaged mold. FCM clustering was found to be an effective algorithm for clustering of acoustic emission vectors composed of multiple features [28] and [29].

We introduced principal component analysis (PCA) for presentation of feature vectors \mathbf{Z}_s . Principal component analysis, as an unsupervised feature reduction method, is mathematically defined as an orthogonal linear transformation that transforms the data into a new coordinate system. Fig. 6 shows the distribution of feature vectors \mathbf{Z}_s , where these vectors are divided into five classes. Class 1 represents vectors characteristic for the closing of the mold, Class 2 vectors characteristic for the injection of the melt with maximum pressure, Class 3 vectors characteristic for the holding (packing) stage, Class 4 represents opening of the tool and Class 5 vectors characterizing damage of the mold.

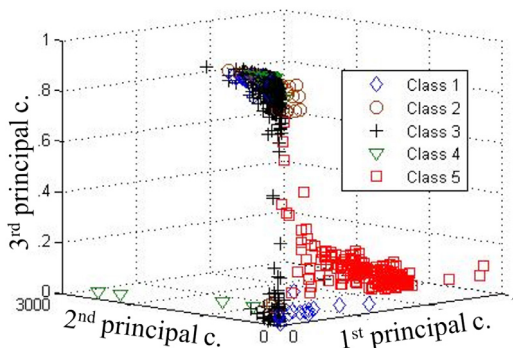


Fig. 6. The distribution of feature vectors \mathbf{Z}_s .

For automatic classification of vectors \mathbf{Z}_s we introduced neural network pattern recognition. The network was set as feed-forward with 10 neurons in the hidden layer. The transfer function was F Tan Sigmoid function for the hidden and the output layer. Five output neurons are used, because of five target classes. Scaled conjugate gradient back-propagation was used for training the network.

Neural network pattern recognition offered us on average 91.6 % correctly classified vectors \mathbf{Z}_s . The lowest error $E = 0.8$ %, or best classification was for vectors of the Class 3. These represent process-orientated bursts during the holding (packing) phase. 96.7 % correct was detection of damage (vectors of Class 5). The algorithm is not recommended for classification of mold closing with 81 % error, i.e. Class 1 vectors, and classification of mold opening vectors (Class 4) with 32 % error.

4 CONCLUSIONS

Results of AE monitoring during injection molding of polypropylene specimens are presented. Useful information about the presence of mold cracks in damaged mold area can be obtained by measuring time domain AE signal parameters during individual injection molding cycle phases. AE signal processing for evaluation of the defects in the injection mold can be achieved also with fractal algorithm using box counting method from time discrete signals. To improve the tool integrity prediction with smaller defects implementation of AE signal analysis based on idea of box counting method is used. Definition of feature vector of AE signal boxes with defined time duration reduces computational complexity during measurement, for example in production environment and simplifies the analysis of acquired AE signals during monitoring.

But AE signal box can represent mixture of information that can be with an individual AE signal burst analysis additionally dismembered. For this we implemented 10-dimensional feature subset vector with instances that are real-valued descriptors (variables). With neural network pattern recognition this vector offers us defining points in appropriate multidimensional space to characterize the damage in a mold with a high accuracy, and also recognition of acquired AE bursts that characterize the injection of the melt and holding phase injection molding production cycle.

5 ACKNOWLEDGMENTS

The research work was partly financed by the Slovenian Ministry for Higher Education, Science and Technology, European Social Fund (ESF) and by the European Union (EU).

6 REFERENCES

- [1] Pollock, A.A. (2009). Fundamentals of Acoustic Emission Testing. Moore, P.O., Miller, R.K., Hill, E.V.K. (eds.), *Nondestructive Testing Handbook—Acoustic Emission Testing*, 3rd ed. American Society for Nondestructive Testing. Columbus, p. 31-108.
- [2] Davoodi, S., Mostafapour, A. (2013). Modeling acoustic emission signals caused by leakage in pressurized gas pipe. *Journal of Nondestructive Evaluation*, vol. 32, no. 1, p. 67-80, DOI:10.1007/s10921-012-0160-x.
- [3] Harri, K., Guillaume, P., Vanlanduit, S. (2008). On-line damage detection on a wing panel using transmission of multisine ultrasonic waves. *NDT & E International*, vol. 41, no. 4, p. 312-317, DOI:10.1016/j.ndteint.2007.10.012.

- [4] Mazal, P., Pazdera, L., Kolar, L. (2006). Basic acoustic emission signal treatment in the area of mechanical cyclic loading. *International Journal of Microstructure and Materials Properties*, vol. 1, no. 3-4, p. 341-352, DOI:10.1504/IJMMP.2006.011649.
- [5] Cao, J., Luo, H., Han, Z. (2012). Acoustic emission source mechanism analysis and crack length prediction during fatigue crack propagation in 16Mn steel and welds. *Procedia Engineering*, vol. 27, p. 1524-1537, DOI:10.1016/j.proeng.2011.12.617.
- [6] Mukhopadhyay, C.K., Sasikala, G., Jayakumar, T., Raj, B. (2012). Acoustic emission during fracture toughness tests of SA333 Gr.6 steel. *Engineering Fracture Mechanics*, vol. 96, p. 294-306, DOI:10.1016/j.engfracmech.2012.08.004.
- [7] Drummond, G., Watson, J.F., Acarnley, P.P. (2007). Acoustic emission from wire ropes during proof load and fatigue testing. *NDT & E International*, vol. 40, no. 1, p. 94-101, DOI:10.1016/j.ndteint.2006.07.005.
- [8] Kim, K.-B., Yoon, D.-J., Jeong, J.-C., Lee, S.-S. (2004). Determining the stress intensity factor of a material with an artificial neural network from acoustic emission measurements. *NDT & E International*, vol. 37, no. 6, p. 423-429, DOI:10.1016/j.ndteint.2003.08.007.
- [9] Baensch, F. (2014). *Damage Evolution in Wood and Layered Wood Composites Monitored in Situ by Acoustic Emission, Digital Image Correlation and Synchrotron Based Tomographic Microscopy*. PhD Thesis, ETH Zürich, Zürich.
- [10] Podrug, S., Glodež, S., Jelaska, D. (2011). Numerical Modelling of Crack Growth in a Gear Tooth Root. *Strojniški vestnik - Journal of Mechanical Engineering*, vol. 57, no. 7-8, p. 579-586, DOI:10.5545/sv-jme.2009.127.
- [11] Akrache, R., Lu, J. (2011). Integrated Design for Fatigue Life Estimation of Structures. *Strojniški vestnik - Journal of Mechanical Engineering*, vol. 57, no. 7-8, p. 547-554, DOI:10.5545/sv-jme.2008.043.
- [12] Carboni, M., Bruni, S., Crivelli, D., Guagliano, M., Rolek, P. (2014). A study on the performance of acoustic emission and low frequency vibration methods to the real-time condition monitoring of railway axles. *12th International Conference of the Slovenian Society for The Non-Destructive Testing in Engineering, Journal of Acoustic Emission*, vol. 32, p. S1-S20.
- [13] Zaki, A., Chai, H.K., Aggelis, D.G., Alver, N. (2015). Non-Destructive evaluation for corrosion monitoring in concrete: A review and capability of acoustic emission technique. *Sensors*, vol. 15, no. 8, p. 19069-19101, DOI:10.3390/s150819069.
- [14] Momon, S., Godin, N., Reynaud, P., R'Mili, M., Fantozzi, G. (2012). Unsupervised and supervised classification of AE data collected during fatigue test on CMC at high temperature. *Composites Part A: Applied Science and Manufacturing*, vol. 43, no. 2, p. 254-260, DOI:10.1016/j.compositesa.2011.10.016.
- [15] Aggelis, D.G. (2011). Classification of cracking mode in concrete by acoustic emission parameters. *Mechanics Research Communications*, vol. 38, no. 3, p. 153-157, DOI:10.1016/j.mechrescom.2011.03.007.
- [16] Svečko, R., Kusić, D., Kek, T., Sarjaš, A., Hančič, A., Grum, J. (2013). Acoustic emission detection of macro-cracks on engraving tool steel inserts during the injection molding cycle using PZT sensors. *Sensors*, vol. 13, no. 5, p. 6365-6379, DOI:10.3390/s130506365.
- [17] Marec, A., Thomas, J.-H., El Guerjouma, R. (2008). Damage characterization of polymer-based composite materials: Multivariable analysis and wavelet transform for clustering acoustic emission data. *Mechanical Systems and Signal Processing*, vol. 22, no. 6, p. 1441-1464, DOI:10.1016/j.ymssp.2007.11.029.
- [18] Požar, T., Možina, J. (2014). Detection of subnanometer ultrasonic displacements. Sattler, K.D. (ed.), *Fundamentals of Picoscience*; CRC Press, Boca Raton, p. 553-578.
- [19] ISO 294-3 (2002). *Plastics – Injection Moulding of Test Specimens of Thermoplastic Materials – Part 3: Small Plates*. International Organization for Standardization, Geneva.
- [20] Kumar, J., Punnose, S., Mukhopadhyay, C.K., Jayakumar, T., Kumar, V. (2012). Acoustic emission during tensile deformation of smooth and notched specimens of near alpha titanium alloy. *Research in Nondestructive Evaluation*, vol. 23, p. 17-31, DOI:10.1080/09349847.2011.622068.
- [21] Hase, A., Mishina, M., Wada, M. (2012). Correlation between features of acoustic emission signals and mechanical wear mechanisms. *Wear*, vol. 292-293, p. 144-150, DOI:10.1016/j.wear.2012.05.019.
- [22] Shenoi, B.A. (2006). *Introduction to Digital Signal Processing and Filter Design*. John Wiley & Sons, Hoboken, New Jersey.
- [23] Župerl, U., Čuš, F., Irgolič, T. (2016). Prediction of Cutting Forces in Ball-End Milling of Multi-Layered Metal Materials. *Strojniški vestnik - Journal of Mechanical Engineering*, vol. 62, no. 6, p. 340-350, DOI:10.5545/sv-jme.2015.3289.
- [24] Aijun Yin, Juncheng Lu, Zongxian Dai, Jiang Li, Qi Ouyang, (2016). Isomap and Deep Belief Network-Based Machine Health Combined Assessment Model. *Strojniški vestnik - Journal of Mechanical Engineering*, vol. 62, no. 12, p. 740-750, DOI:10.5545/sv-jme.2016.3694.
- [25] Zhu, K., Wong, Y.S., Hong, G.S. (2009). Wavelet analysis of sensor signals for tool condition monitoring: A review and some new results. *International Journal of Machine Tools and Manufacture*, vol. 49, no. 7-8, p. 537-553, DOI:10.1016/j.ijmachtools.2009.02.003.
- [26] Wang, X.H., Zhu, C.M., Mao, H.L., Huang, Z.F. (2009). Wavelet packet analysis for the propagation of acoustic emission signals across turbine runners. *NDT & E International*, vol. 42, no. 1, p. 42-46, DOI:10.1016/j.ndteint.2008.07.005.
- [27] Van der Heijden, F., Duijn, R.P.W., de Ridder, D., Tax, D.M.J. (2002). *Classification, Parameter Estimation and State Estimation*, John Wiley & Sons, West Sussex.
- [28] Oskouei, A.R., Heidary, H., Ahmadi, M., Farajpur, M. (2012). Unsupervised acoustic emission data clustering for the analysis of damage mechanisms in glass/polyester composites. *Materials & Design*, vol. 37, p. 416-422, DOI:10.1016/j.matdes.2012.01.018.
- [29] Kek, T., Kusić, D., Grum, J. (2016). Wavelet packet decomposition to characterize injection molding tool damage. *Applied Sciences*, vol. 6, no. 2, p. 45-57, DOI:10.3390/app6020045.

Characterization of Impact Damage in Composite Plates

Bibi Intan Suraya Murat¹ – Paul Fromme² – Marco Endrizzei³ – Alessandro Olivo³

¹ Faculty of Mechanical Engineering, University Technology MARA, Malaysia

² University College London, Department of Mechanical Engineering, UK

³ University College London, Department of Medical Physics and Biomedical Engineering, UK

Low-velocity impact on composites typically produces a barely visible damage at the impacted surface. The internal defects can be complex, consisting of multimode damage and the extent of the impact damage normally spreads across the thickness under the impacted surface. The characterization of impact damage in composites can be very complicated and varies for every different composite structure. In this paper, independent characterization of the low-velocity impact damage on carbon-fiber/epoxy plates using three different non-destructive evaluation methods were used. The goal is to demonstrate the ability of guided ultrasonic waves imaging technique and compared to the more widely employed techniques such as X-ray imaging and ultrasonic immersion C-scan. It was demonstrated that the low frequency A_0 guided ultrasonic wave mode generated by a low-cost piezoelectric transducer can be successfully employed to detect impact damage in composite plates and managed to estimate the size and shape of the impact damage.

Keywords: low-velocity impact, composite plates, X-ray, ultrasonic C-scan, guided waves

Highlights

- Independent characterization of the impact damage using three different NDE methods: X-ray imaging, ultrasonic immersion C-scan and guided ultrasonic waves.
- X-ray can indicate local fiber debonding and mark the area of matrix cracks.
- Ultrasonic C-scan provides a useful approximation of size and depth of the impact damage.
- The guided ultrasonic waves efficiently localize the impact location and provide details of the impact damage such as depth, exact length and width of the impact damage.

0 INTRODUCTION

Composites are widely used in various applications such as aircraft because of their unique properties that can be tailored to meet specific requirements. Often composites are in the form of laminates, made of layers of different fiber orientations that are bonded together. One major concern related to composite structural integrity is the susceptibility of composite materials to incur low-velocity impact damage. The failure process caused by low-velocity impact in composites is a complex phenomenon. Matrix cracking, delamination, fiber debonding and fiber breakage are examples of various failure modes [1].

Interface delamination in cross-ply composites is of particular interest because it can lead to a significant loss of load carrying capacity. In contrast to matrix cracks or fiber breakage, delamination can occur in the absence of any visible damage, making it difficult to detect by a visual inspection as it normally does not appear on the surface [2]. Hence, it can be concluded that delaminations developed at the initial stage of an impact event are more dangerous to the structural integrity, as they could continue to expand and spread to the entire structure. Failure to detect this internal damage at an early stage may result in a

catastrophic failure of the composite structure. This concern provided the motivation for this study.

Currently, the aerospace industry utilizes a variety of NDE methods for post-fabrication and in-service inspection. The commonly used NDE methods are as follows: visual inspection, eddy current, magnetic particle, radiography, thermography and ultrasonic inspection. Most of the methods are limited to the detection of flaws that lie near the surface such as surface cracks, corrosion and other structural defects. Radiography inspection is especially suited for the inspection of internal defects that cannot be detected by visual inspection. However, it requires parts to be detached or dismantled first, hence consuming significant inspection time. Acoustic emission technique [3], electrical resistance method [4] and embedded sensors in composites for online monitoring [5] are some of the advanced NDE methods that are able to provide damage information. However, some of these methods might be less suited for the inspection of an aircraft in noisy environments. Ultrasonic C-scans can produce very sensitive measurements of the location and size of damage, but requires removal of test-parts from the structure and the test part needs to be immersed in a water tank. This causes significance disruption to service operation. The condition of the monitored structure can be

easily obtained using ultrasonic double through-transmission, but it is rather impractical for inspecting large structures when access is limited. Ultrasonic inspection techniques where air-coupling is used are an alternative, but known to be less sensitive to defects [6]. High wave attenuation associated with the composite properties and high frequency transducers limits the inspection on large complex structures. Ultrasonic phased array [7] and tomography [8] have recently been utilized more in aircraft SHM as they can produce high resolution images. However the biggest problem with these methods is the requirement of good coupling and a constant angle of incidence for reproducible inspection results.

The shortcomings of current methods indicate a need for rapid inspection, online monitoring and cost-effective methods for the inspection of large composite structures. One possible method is the guided ultrasonic wave method. The ability to inspect a structure from a single transducer position results in a simple and fast inspection [9]. For the realization of reliable NDE techniques in composites, the aim of this study is to present the characteristic of impact damage in composite plates using three different NDE methods.

1 METHODS

Two specimens were supplied by the Composite Systems Innovation Centre, University of Sheffield, which had been investigated in a separate study [4]. The composite plates (990 mm × 110 mm × 2 mm) were fabricated with unidirectional prepreps by autoclave cure using Cytec 977-2 / Tenax HTS cross-ply laminates. The plates consist of 8 prepreg layers with a symmetric layup sequence of $[0/90]_{2s}$. The specimens were subjected to a 7.4 J impact damage using a hemispherical 15 mm impactor head and following standard drop weight impact procedures. A small degree of fiber fracture and indentation is visible on the surface of the plates.

In order to reveal the extent of the impact damage, the NDE measurements were performed on the defective composite plates for the detection and characterization of impact damage. The following section describes the procedure as well as their results.

2 RESULTS

2.1 X-ray Imaging

It should be noted that this experimental work was performed by a collaborator in Department of Medical

Physics and Biomedical Engineering, UCL. The system and parameters for the X-ray imaging used is as follows in experiment [10]. The X-ray source is composed by using the ordinary test set-up for an Edge-Illumination imaging system where a sample mask that shapes the beam before it interacts with the sample, and an analyser which is composed of a second mask and a digital detector. This method generally is capable of inspecting materials with hidden flaws by using short-wavelength electromagnetic radiation to penetrate into various materials. The variations in the transmitted X-ray intensity are used to determine the thickness or composition of the object or flaws in the object.

Fig. 1 shows a conventional X-ray image of an impacted cross-ply composite plate, provided by collaborators from the Composite Systems Innovation Centre, University of Sheffield. It should be noted that the X-ray testing was performed on a different, but similar plate to the specimens. The oval shape and the marking out of the damage extremities can be clearly seen. The high black density region is significant compared to other regions, which identifies the location of the impactor head. This could correspond to a small degree of fiber fracture under the impactor head. The high contrast region marked the boundaries between the undamaged and damaged regions, which could be contributed to delamination and matrix cracks. The low contrast regions correspond to the undamaged regions, where no significant changes could be detected. Based on the report by the collaborator, the extended length beyond the impactor-located damage area (15 mm in diameter) were estimated to be approximately 20 mm and 25 mm respectively on the left and right sides, making the total length of the defective region approximately 60 mm (in x -direction). Due to the oval shape, the widths (minor diameters) varied from 5 mm to 30 mm across the defective region. Unfortunately there was no scale provided on the image.

Fig. 2 presents the reconstructed X-ray images on one of the two tested composite plates that are based on the edge-illumination technique, performed in the Department of Medical Physics and Biomedical Engineering, University College London. The method enables dark-field imaging by using incoherent illumination and operates with broadband radiation [11]. The same composite panels were used in their studies and it is expected that these results could provide some extra information about the impact damage. As a preliminary demonstration, the extracted images show a strong differential contrast for the composite plate. The presence of the high contrast of

adjacent densities can be clearly observed from both vertical and horizontal X-ray scattering, which reveal defects inside the plate. The bright lines could indicate local fiber debonding and the two small bright areas which nearly resemble the shape seen in Fig. 2 could probably mark the area of matrix cracks in the plate. This bright area could be used to approximate the size of impact damage in the plate. However, no further information is obtained from the collaborator since this project is still under development. Overall, the damaged region, shape and the extent of the impact damages were observed from the X-ray analysis.

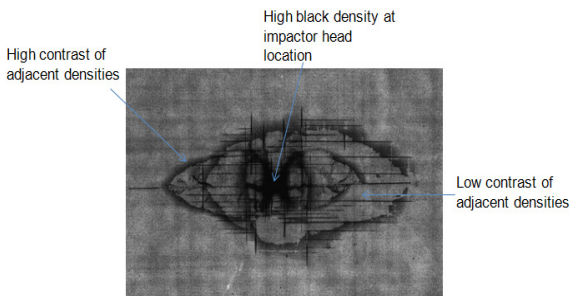


Fig. 1. X-ray images of composite plate impacted at 7.4 J with impact damage; provided by collaborator in Composite Systems Innovation Centre, University of Sheffield

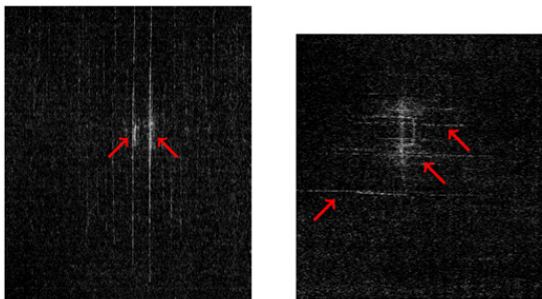


Fig. 2. X-ray images of composite plate impacted at 7.4 J with impact damage; a) vertical scattering; and b) horizontal scattering

2.2 Ultrasonic C-scan

An immersion ultrasonic C-scan method was performed to obtain an approximation of the size, shape and depth of the impact damage in the defective composite plates. The method involved the detection of echoes produced when an ultrasonic pulse was reflected from a discontinuity or an interface in the plates.

The C-scan inspection was performed on one small cross-ply plate due to the requirement of cutting the plate into a small piece for immersion in the water tank. The plate was cut to 200 mm length and

110 mm width, with thickness of 2 mm. The impact was located approximately at the middle of the cut-out plate. A 5 MHz focused ultrasonic transducer was used with a focal length of 76.2 mm. A focused immersion transducer was used because it expansion the sensitivity to small defects or other reflectors. For longitudinal wave travelling in thickness direction of the small cross-ply plate at 2700 m/s speed, the wavelength was estimated to be 0.54 mm. The transducer was mounted perpendicular to the surface of the small cross-ply plate. The distance of water path was set to be about 76.2 mm between the transducer and test plate. The reason was to match the focal length of the transducer, where the signal with the highest amplitude was located. The scanned area was 40 mm × 40 mm. The inspection resolution was 1 mm in both the *x*- and *y*-direction for the amplitude C-scan images as shown in [12].

The C-scan display records echoes from the internal portions of the test plate as a function of the position of each reflecting interface. The corresponding wavelength in the composite panel is 0.54 mm. For the C-scan image representation, two different time gating settings were used. The first time gate was set to capture the positive maximum of reflections from the surface. The second time gate was set to capture the negative minimum amplitude that corresponds to the reflections within the plate.

Fig. 3 presents typical received time traces measured from the front surface. The time traces were obtained at four locations, all located at *y* = 20 mm, but *x* positions were varied: 5 mm, 15 mm, 25 mm and 35 mm. The signal monitored at position (*x* = 5 mm, *y* = 20 mm) represents a signal collected at the undamaged area. The green dashed line (*x* = 25 mm, *y* = 20 mm) corresponds to the reflection from the dented and cracked area (caused by the impact). Measuring the time of flight from the front surface reflection and knowing the thickness and wave speed of the material (approximately 2700 m/s ±10 %), one can determine the arrival time of the reflection from the back-wall surface. Since the front surface reflection (first echo) arrived at 98 μs, the back-wall reflection was calculated to arrive at approximately 99.5 μs ±10 %. The time interval of echoes from every layer cannot be detected as the wavelength (0.54 mm) is larger than the nominal thickness of each layer (0.25 mm thick). Fig. 3 shows three groups of reflections that can be observed based on their arrival times. These groups correspond to the reflections from (i) the surface, (ii) within the plate thickness and (iii) back-wall of the plate.

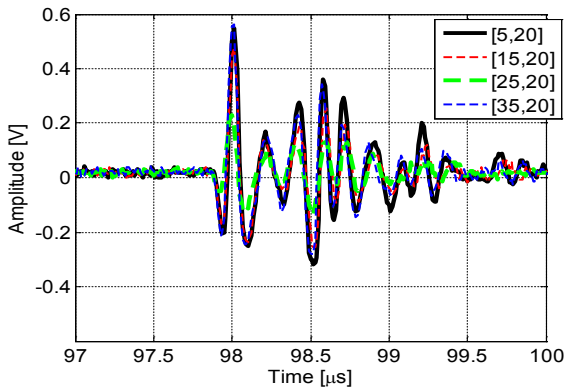


Fig. 3. Comparison of response signals at various locations; signal at location $x = 5 \text{ mm}$, $y = 20 \text{ mm}$ corresponds to the undamaged signal; pulse-echo mode; focused; 5 MHz frequency

From Fig. 3, it can be observed that the lowest reflected amplitude (0.2 V) was obtained from the signal measured at the center of the impacted area ($x = 25 \text{ mm}$, $y = 20 \text{ mm}$). The other three signals have higher amplitudes (0.6 V) of the surface reflection, which described the undamaged and smoother surface. For the second group of the reflections within the plate, multiple peaks of reflections occurred, which can be due to local higher scattering from within the plate. Again it can be observed that the lowest reflection amplitude (0.1 V) was obtained at the impacted area. This shows that the irregular surface (at the impactor location) greatly degraded the normal incident and reflected waves. Meanwhile, the other three signals have inconsistencies in their amplitudes. This may be related to the variations and changes in the interlaminar condition caused by the impact on the surface. What is interesting in this data is that the assumed undamaged signal (based on visual inspection on the surface area) also produced multiple reflections as the other signals. The highest reflected amplitude was observed at $98.5 \mu\text{s}$. Briefly, the arrival time matches approximately to a quarter of the plate thickness. This could indicate the through-thickness location of the delamination as the delamination is normally located in-plane between plies, which produces high reflections. Turning now to the last reflected group (the back-wall reflections), it can be observed that the highest amplitude reflection was obtained from signal monitored at the undamaged area ($x = 5 \text{ mm}$, $y = 20 \text{ mm}$). This could be due to less wave attenuation and scattering between the plies. Meanwhile, the back-wall reflections from the damaged area are lower than that observed in the undamaged location, which relates to the scattering by the impact damage within the plate.

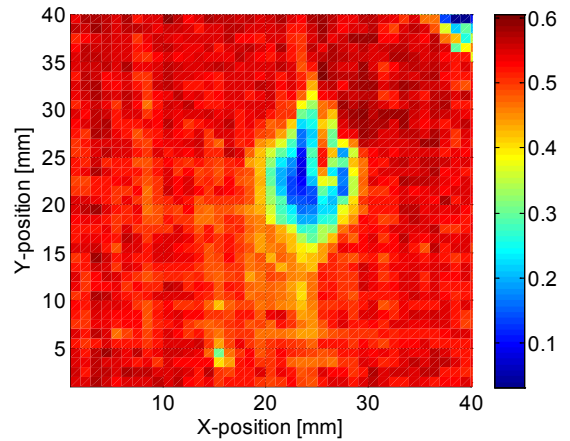


Fig. 4. C-scan image of the front surface of the 2 mm cross-ply specimen; 40 mm \times 40 mm scanned area; 5 MHz frequency; 76.2 mm transducer focal length

Fig. 4 shows the C-scan image of the front surface of the test plate (that has a smoother surface compared to the back-wall surface). This image was generated using the maximum peak amplitude of the first reflection. Referring to Fig. 3, the first reflection is mainly a reflection from the plate surface and therefore it is expected not to be sensitive to the internal defects. From Fig. 4, the impact damage is located in the middle of the scanned area. The oval shape region reasonably matches the 15 mm diameter of the hemisphere shaped impactor head. The oval shaped section with lower amplitude region, ranging from 0.1 V to 0.4 V, can be clearly observed with an approximate length of 10 mm (x -axis) and width of 15 mm (y -axis). This lower amplitude at the impacted area can be explained by the fact that the incident wave encounters the dented surface, which causes the wave to be reflected back at different angles and causes energy loss due to the scattering at the surface. Meanwhile, the rest of the area has a consistently higher and uniform reflected amplitude within a range of 0.5 V to 0.6 V due to the smooth plate surface.

Fig. 5 shows a C-scan image of the same section as Fig. 4, but plotted using the minimum negative amplitude, time gated after the surface reflection. This image represents the internal reflections from within the plate. From the figure, the oval shape with relatively low minimum amplitude (0 V to 0.2 V) as similarly obtained from Fig. 4 can be seen. This shows that the surface indentation not only reduced the normal incident wave but also the reflected wave from within the plate. It also appears there is another large region (half oval shape) with the highest negative amplitude (0.2 V to 0.3 V). This is not observed in Fig.

6, which is time gated for the first surface reflection only.

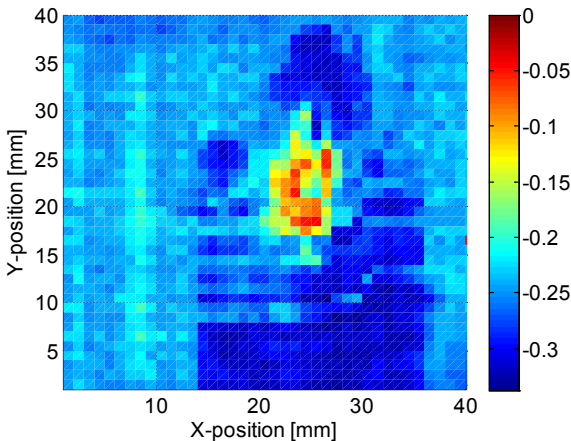


Fig. 5. C-scan image of negative peak amplitude measured from the frontal surface of the 2 mm cross-ply panel; 40 mm × 40 mm scanned area; 5 MHz frequency; 76.2 mm transducer focal length

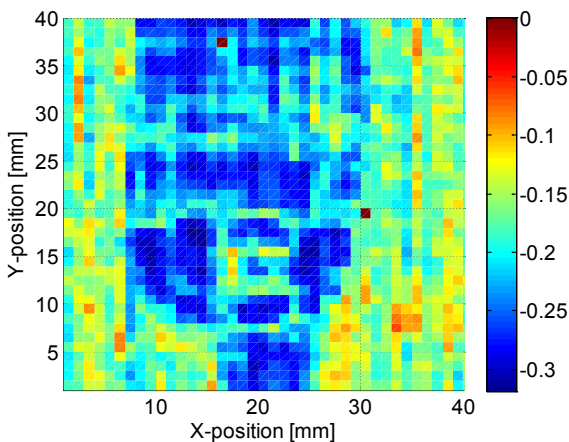


Fig. 6. C-scan image of negative peak amplitude measured from the back-wall surface of the 2 mm cross-ply panel; 40 mm × 40 mm scanned area; 5 MHz frequency; 76.2 mm transducer focal length

The same time gating (after surface reflection; negative minimum amplitudes) was also used from the back wall surface (rougher surface compared to the front surface). Fig. 6 shows an approximately similar pattern as obtained in Fig. 5, although the sharp oval shape area (0 V to 0.2 V) was not observed in this figure as the back surface was not dented. The extent of the impact damage (0.2 V to 0.3 V) is reproducible although the surface of the back-wall is rougher. This time gated approach seems to be more sensitive to the extent of the impact damage in the composite laminate. The possible defective area is much larger, about 20 mm and 40 mm in the x - and

y -axis respectively, and the damage level (indicated by different amplitude relative to the neighborhood area) is significant. However, the width of the damaged area could be larger than the scanned area, and may spread in a similar oval-shaped pattern. In relation to that point, Sohn et al. [13] have found that the impact response and damage states in flat composite panels is dependent on the diameter of the spherical impactor head. Although this result does not give full information about damage distribution through the thickness, it has provided a useful approximation of size and depth of the impact damage in the composite plate. It is worthwhile at this stage to use this information for the comparison between the numerical predictions and the experimental results of the guided wave scattering at impact damage.

2.3 Guided Ultrasonic Waves

A piezoelectric transducer consisting of a piezoelectric disc and a brass backing mass was bonded to the plate using Loctite 2-part epoxy glue approximately 50 mm from the center of the impact damage. The first antisymmetrical (A_0) guided wave mode with an excitation frequency of 100 kHz was chosen below the cutoff frequencies for the higher wave modes. The excitation signal consisted of a 5-cycle Hanning windowed toneburst generated by a programmable function generator. The wave propagation and scattering around defects is measured using a commercially available heterodyne laser vibrometer fixed to a scanning rig, which permits the non-contact and remote sensing of the guided waves. The voltage signal corresponds to the velocity of the out-of-plane-displacement of the specimen surface. The measurement was performed on the area of 40 mm × 40 mm area containing the impact damage with a step size of 1 mm in both directions. The time traces of the received signals were collected and further processed in Matlab. From the scanned time signals, wave field images were reconstructed and processed to study the interaction of the guided wave with the impact damage.

Fig. 7 presents the guided wave fields at various time snapshots, respectively for damaged composite plate 1 and 2. It can be seen that the incident wave interacts with the impact damage and causes scattering within the damaged region. Relatively weak scattering by the damage is present when the incident wave arrives (Figs. 7a and c), then a significant increase of the scattering is apparent when wave has travelled past the damaged area (Fig. 7b and d). Based on the FE study, a significant portion of the waves is also

reflected back from the exit of the impact damage. These reflected waves travel within the damaged region and keep reflecting back at both entrance and exit of the impact damage. As a consequence of these multiple reflections, a considerable amount of guided wave energy is trapped inside the impact damage area. This causes an increase in the amplitude of the wave in that region.

The amplitude of the transmitted waves diminished noticeably after passing through the impacted area. Similar wave behavior was also observed by Sohn et al. [13], where the measurement was performed on a quasi-isotropic composite plate. This finding however is contradictory to some of the FE simulation results [12], where a large amount of transmitted wave can be observed. However, some FE results have demonstrated the reduction in the amplitude past the delamination area. The FE simulations for the delamination placed at 0.5 mm depth is in agreement with this experimental measurement. Comparing both specimens, which were impacted with same 7.4 J impact energy, it can be seen that guided wave scattering in both plates are unique and such variations are expected due to the complexity in the failure mechanism of impact damage.

Fig. 8 presents the image of the maximum amplitude of the signal envelope over the damaged areas in both composite specimens. Areas of higher amplitudes can be seen, that occur close to the impact location center ($x = 20$ mm, $y = 20$ mm). This indicates the presence of severe damage such as a delamination or fiber and matrix cracking, and matched reasonably well with the visually observed size of the impact damage on the plates as well as the X-ray and C-scan images. Meanwhile, the undamaged area is represented by the low amplitude distribution. From the figure, three different zones can be observed and each zone has its own wave propagation behavior; (i) Zone 1: before the impact damage ($x < 15$ mm), (ii) Zone 2: across the impact damage (15 mm $< x < 25$ mm), and (iii) Zone 3: behind the impact damage ($x > 25$ mm).

The first zone (before damage) shows the incident waves propagating towards the impact damage location. It is also can be seen there were reflected waves propagating back towards the excitation source. Some periodical increase and decrease of the amplitude is visible in the region around $x = 15$ mm, potentially indicating the interference between the incident and the reflected waves at the impact damage. In zone 2, high amplitudes of the A0 mode signals are visible, which could indicate the multiple reflections

and scattering events within the impact damage area. Meanwhile, in zone 3, the transmitted waves propagating out from the damaged area are seen to be blocked in certain direction with significantly reduced signal amplitudes. Considerable waves transmitted

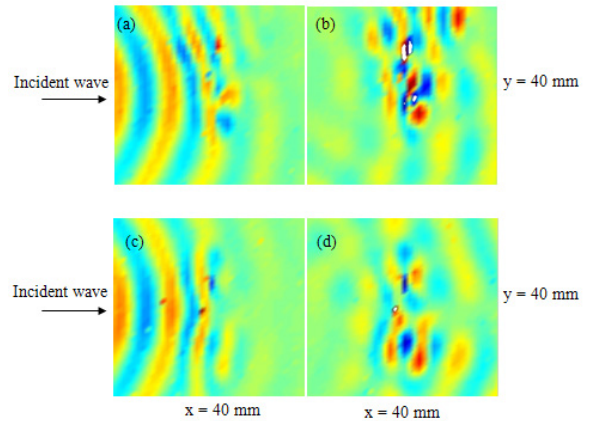


Fig. 7. Guided wave displacement fields in two composite plates; Plate No. 1, snapshot time; a) 20 μ s and b) 30 μ s; Plate No. 2, snapshot time; c) 20 μ s and d) 30 μ s; 7.4 J impact; 40 mm \times 40 mm scanned area

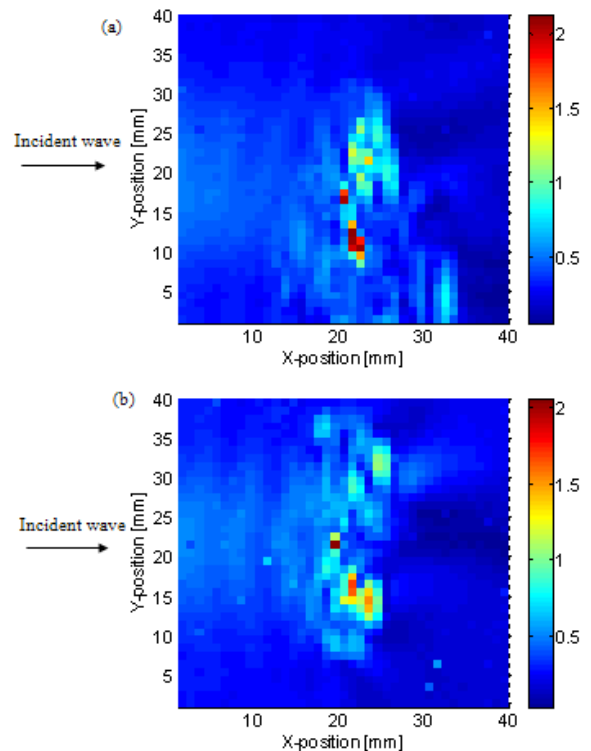


Fig. 8. Maximum amplitudes of guided wave pulse across damaged area of composite plate: a) Plate 1; b) Plate 2; frequency 100 kHz; 40 mm \times 40 mm area with impact location at center ($x = 20$ mm, $y = 20$ mm)

across the impact damage indicate that probably little mode conversion occurred as has been observed from the FE simulations. The cross-section of the impact damage in Plate no. 1 can be roughly approximated with length of 10 mm (x -axis) and width of 20 mm (y -axis), identified by the higher amplitude maxima. For Plate no. 2, the cross section area of the impact damage can be estimated to be about 10 mm \times 25 mm.

Referring to the FE simulation results in [12] and [14] good agreement between the experimental and simulated result was achieved. Similar wave propagation behaviour before and within the impact damage can be observed from both results. The increase in amplitudes identifies the localization of the impact damage in the measured area. There was a significant difference in the wave behaviour behind the damage location, where many FE simulations did not predict a persistent amplitude drop compared to the experimental results. Details of the impact damage such as depth, exact length and width as well as its complex scattering are further investigated here [15] and [16]. From this study, it is evident that the impact damage can be detected using the guided ultrasonic wave measurement.

3 CONCLUSIONS

This paper reports the characterization of impact damage using 3 different NDE methods: X-ray, ultrasonic C-scan and guided ultrasonic waves. From the X-ray measurement, it has shown that it can indicate the local fiber debonding and mark the area of matrix cracks, whereas the ultrasonic immersion C-scan provides a useful approximation of size and depth of the impact damage. From the scattering of the guided wave at the impact damage, this method efficiently localized the impact location and provide details such as depth, exact length and width of the impact damage. Comparing these three methods, the guided ultrasonic waves method perfectly demonstrated the capability to detect impact damage in composite plates using smaller equipments that are less expensive and have a quick experimental setup and measurements.

4 ACKNOWLEDGEMENTS

The author gratefully acknowledges the support in funding by Universiti Teknologi Mara (UiTM), Malaysia, especially from the Geran Dana Pembudayaan Penyelidikan (600-RMI/RAGS 5/3 (12/2015)).

5 REFERENCES

- [1] Murat, B.I.S., Rahman, A.A.A. (2017). Study of impact damage behavior in woven carbon fiber plates. *Procedia Engineering*, vol. 170, p. 47-54, DOI:10.1016/j.proeng.2017.03.009.
- [2] Richardson, M.O.W., Wisheart, M.J. (1996). Review of low-velocity impact properties of composite materials. *Composites Part A: Applied Science and Manufacturing*, p. 1123-1131, DOI: 10.1016/1359-835X(96)00074-7.
- [3] Mal, A.K., Shih, F., Barnerjee, S. (2003). Acoustic emission waveforms in composite laminates under low velocity impact. *Proceedings SPIE*, vol. 5047, p. 1-12, DOI:10.1117/12.484448.
- [4] Swait, T.J., Jones, F.R., Hayes, S.A. (2012). A practical structural health monitoring system for carbon fibre reinforced composite based on electrical resistance. *Composites Science and Technology*, vol. 72, no. 13, p. 1515-1523, DOI:10.1016/j.compscitech.2012.05.022.
- [5] Takeda, N., Okabe, Y., Kuwahara, J., Kojima, S., Ogisu, T. (2005). Development of smart composite structures with small-diameter fiber Bragg grating sensors for damage detection: Quantitative evaluation of delamination length in CFRP laminates using Lamb wave sensing. *Composites Science and Technology*, vol. 65, no. 15-16, p. 2575-2587, DOI:10.1016/j.compscitech.2005.07.014.
- [6] Raghavan, A., Cesnik, C.E.S. (2007). Review of guided-wave structural health monitoring. *The Shock and Vibration Digest*, vol. 39, no. 2, p. 91-114, DOI:10.1177/0583102406075428.
- [7] Freemantle, R.J., Hankinson, N., Brotherhood, C.J. (2005). Rapid phased array ultrasonic imaging of large area composite aerospace structures. *Insight - Non-Destructive Testing and Condition Monitoring*, vol. 47, no. 3, p. 129-132, DOI:10.1784/insi.47.3.129.61315.
- [8] Hay, T.R., Royer, R.L., Gao, H., Zhao, X., Rose, J.L. (2006). A comparison of embedded sensor Lamb wave ultrasonic tomography approaches for material loss detection. *Smart Materials and Structures*, vol. 15, no. 4, p. 946-951, DOI:10.1088/0964-1726/15/4/007.
- [9] Murat, B.I.S., Fromme, P. (2013). Detection of impact damage in composite panels using guided ultrasonic waves. *Proceedings of SPIE - Health Monitoring of Structural and Biological Systems*, vol 8695, DOI:10.1117/12.2009459.
- [10] Endrizzi, M., Murat, B.I.S., Fromme, P., Olivo, A. (2015). Edge-illumination X-ray dark-field imaging for visualising defects in composite structures. *Composite Structures*, vol. 134, p. 895-899, DOI:10.1016/j.compstruct.2015.08.072.
- [11] Endrizzi, M., Diemoz, P.C., Millard, T.P., Jones, J.L., Speller, R.D., Robinson, I.K., Olivo, A. (2014). Hard X-ray dark-field imaging with incoherent sample illumination. *Applied Physics Letters*, vol. 104, no. 2, 024106, DOI:10.1063/1.4861855.
- [12] Murat, B.I.S., Fromme, P. (2016). Propagation and scattering of guided waves in composite plates with defects. *International Journal of Automotive and Mechanical Engineering*, vol. 13, no. 3, p. 3728-3741, DOI:10.15282/ijame.13.3.2016.15.0305.
- [13] Sohn, H., Dutta, D., Yang, J.Y., Park, H.J., DeSimio, M., Olson, S., Swenson, E. (2011). Delamination detection in composites through guided wave field image processing. *Composites Science and Technology*, vol. 71, no. 9, p. 1250-1256, DOI:10.1016/j.compscitech.2011.04.011.

- [14] Michaels, T.E., Michaels, J.E., Ruzzene, M. (2005). Damage detection in plate structures using sparse ultrasonic transducer arrays and acoustic wavefield imaging. *AIP Conference Proceedings*, vol. 760, no. 1, 938–945, DOI:10.1063/1.1916774.
- [15] Murat, B.I.S., Khalili, P., Fromme, P. (2014). Impact damage detection in composite panels using guided ultrasonic waves. *AIP Conference Proceedings*, vol 1581, no. 1, p. 286-293, DOI:10.1063/1.4864832.
- [16] Murat, B.I.S., Fromme, P. (2016). Finite element modeling of guided wave scattering at delaminations in composite panels. *Proceedings of SPIE - Health Monitoring of Structural and Biological Systems*, vol. 9805, DOI:10.1117/12.2220409.

Effective Methods for Structural Health Monitoring of Critical Zones of Scalable Wind Turbine Blades

Adriana Savin^{1,*} – Nicoleta Iftimie¹ – Rozina Steigmann¹ – Dorin Rosu² –
Gabriel Silviu Dobrescu¹ – Janez Grum³ – Paul Doru Barsanescu⁴

¹National Institute of R&D for Technical Physics, Nondestructive Testing Department, Romania

²S.C. Compozite S.A., Romania

³University of Ljubljana, Faculty of Mechanical Engineering, Slovenia

⁴Gheorghe Asachi Technical University, Faculty of Mechanical Engineering, Romania

The most important part of wind turbine is the blade that must be tested during fabrication and functioning when can be damaged by moisture absorption, fatigue, wind gusts or lightning strikes. The common defects in turbine blades may be faulty microscopic and mesoscopic appeared in matrix, broken fibers can also appear and develop under moderated loads, or cracks and delaminations due to low energy impacts, etc. The paper presents the results obtained from testing and monitoring of a scalable wind turbine blade (WTB) using different sensors placed on critical location, which were determined by finite element method (FEM) simulation. A comparison between the complementary methods is carried out in order to choose the most efficient method as quality/price ratio.

Keywords: wind turbine blades, structural health monitoring (SHM), nondestructive testing, wireless sensors, fiber Bragg gratings (FBG), strain gauges (SG)

Highlights

- The monitoring of scalable wind turbine blade has been carried out using complementary nondestructive evaluation methods.
- Different types of sensors have been employed as optical fiber sensors, fiber Bragg grating type, wireless sensors based on metamaterials and classical strain gauges rosette placed on critical zones of the blade.
- The critical zones have been determined using finite element method.
- The results have been compared in order experimental emphasize the maximum concentration stress zones, theoretically determined.

0 INTRODUCTION

The problem of climate changing, due to pollution includes not only modification of average temperatures but also changing of its different aspects as winds, quantity and precipitation categories and frequency of extreme meteorological events. Power plants in the European Union will have to cut the amount of toxic pollutants they emit such as sulfur dioxide and mercury, nitrogen oxides, arsenic, lead and cadmium emissions under new rules approved by EU member states on 2017 and widely applauded by environmental groups. Thus, the market for electrical energy obtained by harvesting wind power is expanding [1].

In Romania over 3 % from annual electricity is produced by wind turbines, the majority being GE1.5sle or similar, having the length of the blade of 33.5 m and the height of tower of 65/80 m [2]. In January 1st, 2017, Romania recorded 3025 MW installed in wind turbines (WT), the total number of installed turbines being 1250 at an average turbine power of 2.5 MW (located in 80 wind farms in operation, the average of a wind farm in Romania

being 40 MW) [3]. WT development and increasing of their capacity are important ways to respond to growing global energy demand.

Most of the past years papers are focused on optimizing WT from the point of view of gearbox analysis [4] design parameters to minimize energy costs, maximize energy production [5] and minimize wind turbine blade (WTB) sizes [6] to [8]. This type of optimization resulted in slender blades, with less resistance. All these had implications over the blade profile and lead to rethinking of weight and stability of the blade. Yang et al. [9] studied major design cases meanwhile others [10] were focused on cases with loadings in the design of blades using laser triangulation in order to reduce the design time [11] and the evaluation of their deformations.

In the process of optimizing the structural design of the blade, the priority is to prevent failure in compliance with structural resistance requirements. Critical areas were taken into account when optimizing the blade [12] selecting the Tsai-Wu failure criterion. It can be concluded that the decision to maximize the aerodynamic performances to optimize the objective functions of the wind turbine has to be done

according to safety in operation rules, with the aim of minimum report cost of energy by maximum annual energy production. Chehouri et al. [13] highlights the need to further study the issues that have not been resolved satisfactorily: complete load calculation and composite structural optimization.

We analyzed the methods of calculating blade loads: the basic method was to translate the aerodynamic load into a concentrated force for numerical simulation using moment's theory. Since it is impossible of revealing the pressure distribution of the blade surface, is preferable to be chosen the substitution of the inverse design tool with computational fluid dynamics software and to load the distribution into a finite element method (FEM) solver to investigate the mechanical strength [14]. That needs increasing of the computational time of the optimization process. The use of glass fiber-reinforced plastics (GFRP) is popular in making blades because of it offers production of parts with low weight, high stiffness and good load resistance. However, the use of traditional two dimensional (2D) laminates due to their low properties (stiffness, low fatigue strength) interlaminar failure at shear followed by fracture impose behavioral analysis by complementary methods.

In order to undertake the design optimization, analysis of loads in the design of blades and deformation evaluation, a scalable WTB has been constructed. It had the scaled dynamics of a full-scale blade as well as enough sensors for measurements and monitoring. The scaled WTB studies have been developed to test WTB with better accuracy and lower cost, but with results relevant to full scale WTB [15].

In order to obtain greater efficiency and to increase the generated power, the general trend is to use large-diameter rotors and manufacturing the blades with GFRP due to their low weight. This resulted in WT blades length of 60 m [16]. The blades are usually subject to random and complex mechanical stresses. The most common defects in turbine blades may be faulty microscopic and mesoscopic appeared in matrix, no detected by classical nondestructive testing (i.e. using phased array sensors). Broken fibers can also appear and develop under moderated loads, or cracks and delaminations due to low energy impacts, etc. However, large blades led to no concrete data in due time during in-service inspection. These explain the attention given to structural health monitoring (SHM) [17] systems for WTB, development and consolidation of diagnosis, prognosis methodologies, damage detection (location and their nature). The SHM process involves the observation of a system

over time using periodically sampled dynamic response measurements from an arrangement of sensors, the extraction of damage-sensitive features from these measurements to determine the current state of system health [18]. Fig. 1 illustrates the SHM system concept [10], the blades damages shall be detected and evaluated with high probability of detection and reliability coefficient.

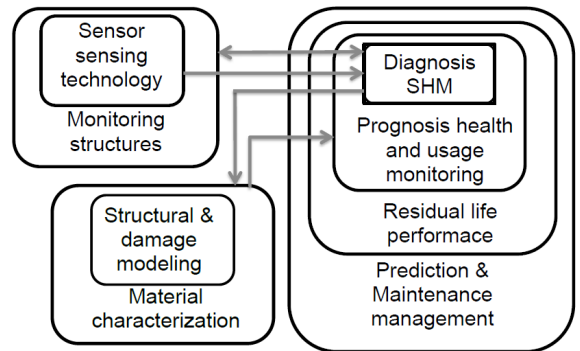


Fig. 1. SHM system

For an estimated lifetime of 20 years and extended as long as is possible, the long-term integrity of a blade became a very interested area. The monitoring of WTB made from GFRP have been reviewed in [9], proposing either statistical pattern recognition using simulation or experimental data, or in [19] considering mechanical property testing and full-scale testing as well as nondestructive testing methods. In order to calculate the lifetime of GFRP structures used in WTB construction, it is essential to have access to information about fatigue resistance of the material. These data include a number of fatigue tests in the frame of specific combinations of amplitude and average stress.

From extended fatigue points of view of GFRP in WTB [20] and, [21] different databases are compiled but the data are not compatible with other experiments databases, being hard to employ them into new ones. There are many literature reviews concerning WTB starting from design, propulsion and including theories of maximum efficiency [21] to [25]. In order to decrease the fabrication and maintenance costs, as well as for avoiding unproductive time, the nondestructive testing (NDT) is required both during fabrication and in-service. NDT techniques for in-service inspection and determination of regions with high degradation risks are developed (function on the type and the size of the WT) [26].

The results of complex mechanical tests, performed on scalable WTB model (in our case a

blade of 1750 mm length) are used to give efficiency to monitoring strategy. Using FEM, the maximum stress zones [27] and damage evolution and remnant stress [28] have been determined.

The paper presents results of testing of a WTB, under static loading, using three types of sensors (i.e. radio-frequency identification (RFID) strain wireless sensor (WRS), optical fiber (OF) fiber Bragg gratings (FBG), stress/strain gauges (SG)) in order to detect possible damages that further can lead to risky flaws. The objective of the current work is to demonstrate that the methodologies for scaled blades can be applied to real size WTB. To the best of our knowledge, this investigation has not been performed for WTBs before.

1 PRINCIPLES

WTBs are most exposed component of WT so that their structures are designed and realized based on the concept that a layered structure more easily supports an early stage damage that can be stopped when it has a tendency to propagate following the repeated loads prescribed by the project. Based on *a priori* knowledge about WTBs, the sensors used for their characterization are placed on the most expected damage area, aiming the minimizing of the sensors number.

1.1 Sensors with Fiber Bragg Grating

SHM includes the use of FBG for detecting delamination in composite laminates [29] and monitor impact event occurrence [30] and [31]. A FBG is a periodic or semiperiodic permanent perturbation of the fiber core refractive index. Optical fiber (OF) sensors are made based on OF in integrated

structures. This sensor can monitor the structure in critical regions. The central wavelength of this signal, called Bragg wavelength λ_B is related to the physical parameters of the grating according to $\lambda_B = 2n\Lambda$ where n is the effective refractive index of the fundamental mode propagating inside the fiber; Λ is the spacing between gratings, known as grating period. When the OF is submitted to strain, the central wavelength is displaced to higher or smaller values [32].

The direction and the magnitude of displacement are proportional with the modification of strain or temperature. The strain axial sensitivity is $d\lambda_B/d\varepsilon \approx \lambda_B(1-p_e)$ where $\partial\lambda_B$ is the OF wavelength shift; $\varepsilon \ll 1$, p_e is photo-elastic coefficient of the fiber $p_e \approx 0.22$. OF sensors, whose gauge lengths are about 10 mm were used for SHM. At the wavelength of our OF, $\partial\lambda_B/\lambda_B \approx 0.78\varepsilon$ so the OF strain sensing can be expressed as $\varepsilon = \frac{1}{0.78 \times 10^{-6}} \frac{\Delta\lambda_B}{\lambda_B}$. In structure of WTB, three OF sensors were embedded along the central longitude of the blade, placed into critical points determined by FEM of blade under bending (red region in Fig. 7).

The optical block diagram of measurement is shown in Fig. 3. The reflectance cell consists of a double FBGs housed in an athermal package and reflect two wavelength peaks (around 1529 nm and 1571 nm). The measurement system consists of a broadband light source, light-emitting diode (LED) that illuminates the optical input line and a reference cell after passing through a 2x2 double-clad fiber couplers that combine the double-clad fiber (single mode core surrounded by a multimode inner cladding) with a standard step-index multimode fiber.

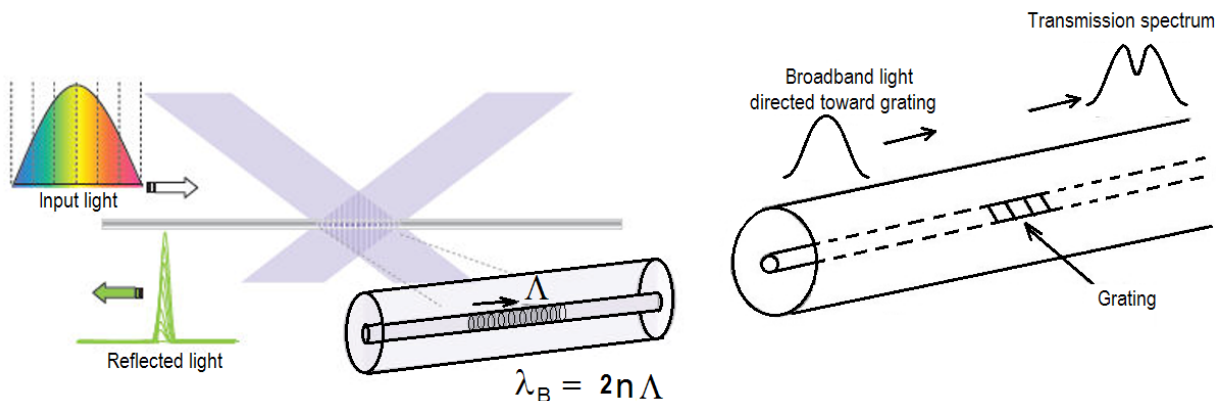


Fig. 2. Fiber Bragg gratings principle [26]

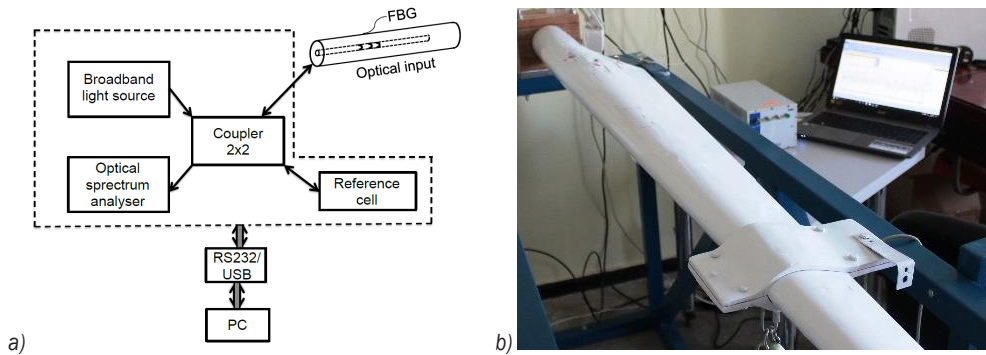


Fig. 3. Basic diagram and FBG interrogator; a) optical block diagram of measurement, b) measurement system

1.2 Wireless Sensors

The passive WRS designed to monitor stress/strain status have as sensitive element that follows the relative displacement (compression or tension) of its components due to loads. In specific construction as 2D geometry on flexible dielectric support with thickness t , having ϵ_d permittivity and σ_d conductivity, copper split-ring resonator (SRR) can be used as stress/strain sensors [33] and [34]. The sensor consists of a folded rectangular microstrip patch antenna [35] coupled with a tunable inductive SRR, with central space of SRR filled with a material having electrical conductivity σ_g , length g and width l , it forms the terminals of a new capacitor C_m , representing the strain cell and with a passive integrated circuit (IC) chip. When over the capacitive strain cell, η strain is applied, the capacitance is modified.

The structure of this type of sensor is shown in Fig. 4a, the sensing element is shown in Fig. 4b.

Resonance frequency of sensor is in range of radio frequency (RF) and microwaves, depends of geometrical dimensions and design. WRS presents resonant properties [36] and the inductance and the capacitance are given by [37]. The resonance frequency is $f_r = c / \sqrt{4(L + \Delta L) \sqrt{\epsilon_r}}$ with c speed of

light in vacuum, L the length of the copper layer, ϵ_r the dielectric permittivity of the substrate, ΔL is the additional length who compensate the effect due to thickness, width and dielectric constant of the substrate.

Parallel with capacitance C , a capacitive element sensitive to stress/strain is connected, with the capacitance varying linear with the strain as $C_{sensitive} = \epsilon_r \epsilon_0 l g / [t(1 + \eta)]$ with t thickness of dielectric layer and η strain in $[\mu\text{m}/\text{m}]$. For the capacitive element, sensitive to stress/strain, to function upon a law closer to this, it is imposed that the Poisson ratio of dielectric support shall be as high as possible. For polyimide, the layer supporting copper strips, the Poisson ratio is 0.4. If $\eta = 10 \mu\text{m}/\text{m}$, the connection between the two-capacitance make C increases with 10 %, inductance L remaining unchanged. Detection system consist in a RFID reader and a RFID tag [38], the tag including the sensor and the IC. When the sensor detect a modification of the strain η , the shifted resonance frequency becomes

$$f'_r = \frac{c}{4(1 + \eta)(L + \Delta L)\sqrt{\epsilon_r}} = \frac{f_r}{1 + \eta} \approx f_r(1 - \eta). \quad (1)$$

For a small load, the resonance frequency modifies almost linear with load, the load can be

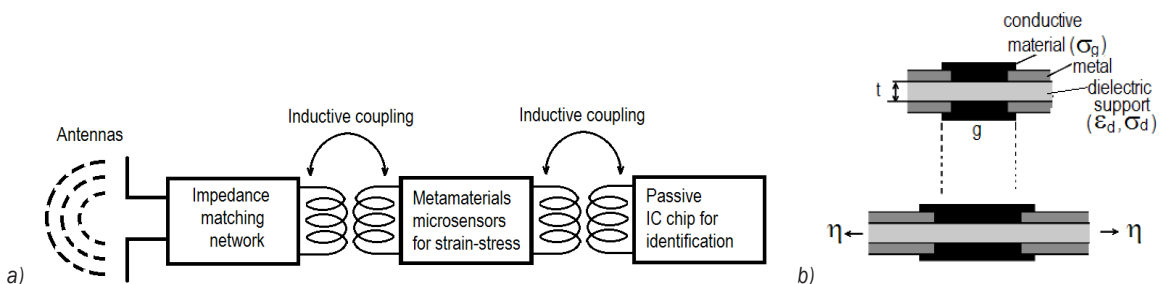


Fig. 4. Metamaterial passive wireless sensors for SHM: a) schematic of a RF / microwave - RFID tag; b) schematic of sensing element

determined if the resonance frequency is measured. Applying a loading force, the inside dielectric is deformed leading to shorting height and increasing of contact area between dielectric and sensing area. Thus, the capacitance is increased transducing the modification of resonant frequency by integrated inductor-capacitor (LC) circuit [27]. The capacitive responses and the applied loads follow a linear relationship, the measuring device providing direct plots of microstrain vs. force.

The RFID tag antenna assures that the interrogation frequency f shall be equal with the one of RFID tag to obtain perfect matching of impedance between antenna tag and IC chip. The smallest amount of energy must be transmitted toward reader to activate RFID tag, the transmitted power threshold (measured through the reader) reach minimum value at resonance frequency.

1.3 Strain Gauges

Three-element strain gage rosette must be employed to determine the principal strains in a general biaxial stress state when the directions of the principal axes are unknown. The usual goal of experimental stress analysis, however, is to arrive at the principal stresses, for comparison with some criterion of failure [38]. Three-element strain gage rosette have the advantages of being thin and flexible, with greater conformability to curved surfaces, minimal reinforcing effect, superior heat dissipation to the test part. They are available in all standard forms of gage construction, and generally accepts all standard optional features, optimal stability, and maximum freedom in lead wire routing and bonding.

The equations for calculating principal strains from three rosette strain measurements are derived from what is known as a “strain-transformation” relationship. For each gauge, maximum and minimum specific strains ϵ_{\max} , ϵ_{\min} , the arbitrary angle θ from the major principal axis, maximum shear strain γ_{\max} , maximum and minimum normal stress, σ_{\max} , σ_{\min} , are calculated.

2 EXPERIMENTAL SET-UP

Detecting early-stage WTB degradations and monitoring their progress over time can lead to improved diagnostic capability and the development of more efficient repair strategies and, last but not least, the improvement of structural blade design. Taking into account the efficacy of the method and *a priori* knowledge about WTB (obtained by

simulations), the sensors is distributed on the most expected damage area, aiming the minimizing of the sensors number (Figs. 5 and 6). The blade has been realized from E-glass/epoxy EPIKOTE Resin MGS LR 385 composite. The leading edge is straight and the trailing edge conical for an easy construction. The profile follows NACA airfoil [15].

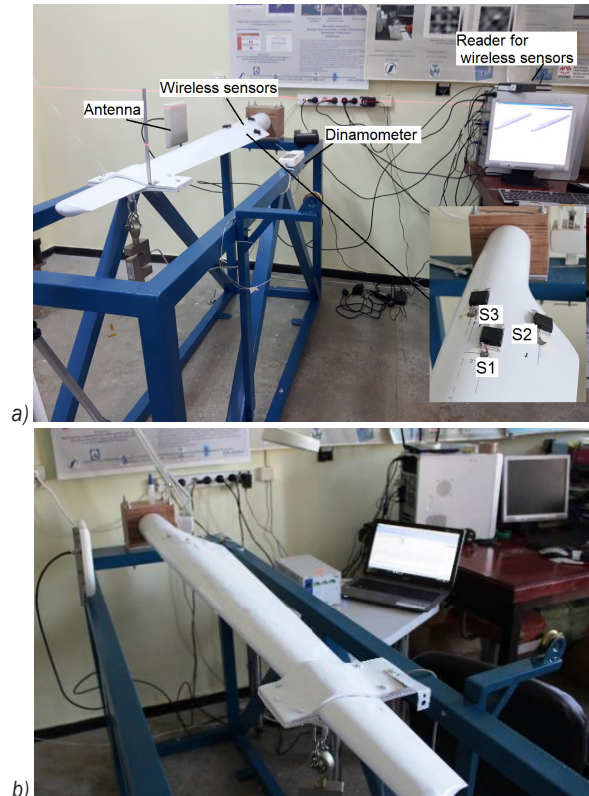


Fig. 5. Testing stand for a) wireless sensors and b) optical fiber measurements

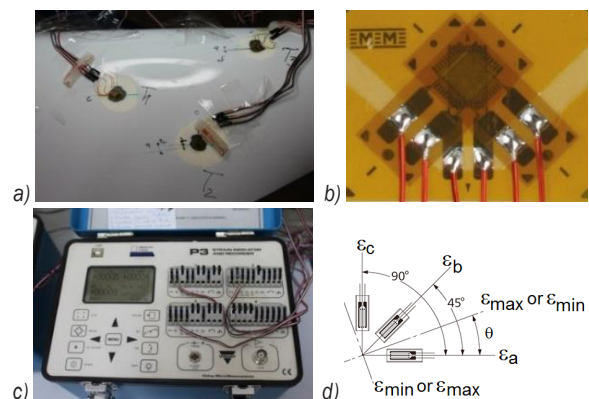


Fig. 6. Strain gauges measurements: a) stress/strain gauge; b) rectangular 3 stacked rosette; c) Vishay P3 strain indicator and recorder; d) positioning of the stacked gauges

For increased structural strength and stiffness at 0.286R (R - the total length of distance between the center of rotor and the tip of blade), the same NACA has been applied both for the upper surface (the top face where sensors are placed) and lower surface (bottom face of the blade), keeping the aerodynamical performances of the blade's tip [15].

The profiles between 0.268R and tip were linearly interpolated. A compromise has to be found between high-resolution and long propagation distance.

Three sensors C2A-06-062WW-350, stacked rosette were used, each having 3 strain gauges with 350 Ω electrical resistance were employed (Figs. 6 a and b). These were connected to Vishay P3 Strain Indicator and recorder (Fig. 6c), in quarter bridge connection with automatic balance.

Their positioning (Fig. 6d) has allowed the determination of deformations due to bending along blade axis at distance of 488 mm from the fixed end, respectively close to trailing edge at 409 mm from the fixed end, as well as closely to the leading edge at 351 mm from the hub. The bending test was effectuated in 7 loading stages with 100 N steps, with maximum of bending momentum of 900.90 Nm.

3 EXPERIMENTAL RESULTS AND DISCUSSIONS

The simulation of blade behavior has been carried out with ANSYS Academic 17.2 at 300 mm distance from the tip of the blade, a compression force of 500 N has been applied on Y axis (blade upper shell) on a region with 100 mm width. The produced displacement of the tip is of 30.082 mm. Fig. 7a presents the division of the blade in critical regions, in Fig. 7b is presented the loading forces disposition towards blade axis. The FEM model shown above takes into account the presence of the reinforcement structure, which's mass cannot be neglected, especially if one considers that the distance from the axis of rotation increase the

inertia and can reduce the frequency associated with the first mode of vibration of WTB. Fortunately, the glass fibers employed makes the structure very rigid. OF sensors are placed in region at 307 mm, 362 mm, 406 mm from the hub fixing in stand. All the loadings are static and the sensors were placed in region with maximum critical points. For establishing critical regions of WTB using FEM, 1338842 nodes, 832563 elements were employed, the maximum dimension of an element being 8 mm.

The resulted maximum stresses were under material flow limit. In all the cases, the stresses on lower shell are higher than on the upper shell. The maximum stresses on WTB appear closely to the joint between the hub and the longeron and at transition between circular geometry to NACA profile. For the WRS the reader antenna is fixed on the upper part of the stand, at 30 cm from the middle area of WRS placement locus.

The antenna is connected to a logger reader coupled to a personal computer (PC) by universal serial bus (USB). IC frequency range is 840 MHz to 960 MHz. The results of bending tests in a loading-unloading cycle are presented in Figs. 8a and b. Maximum deformations at 700 N loadings are characteristics of region where sensor S1 (see inlet in Fig. 5a) is placed (along longeron axis) and the minimums are in the region of sensor S2 (placed outside the critical zone). In addition, the deformation is linear, the loading remain in elastic range. During the unloading, the values follow the same characteristic as at loading.

Comparing loading/unloading data at 500 N with the simulated ones, it can be observed a good correlation of the displacement, experimentally being determined as 37 mm. The OF sensor, FBG single DTG S-01 type used for monitoring composite materials type GFRP [39] have center wavelength in

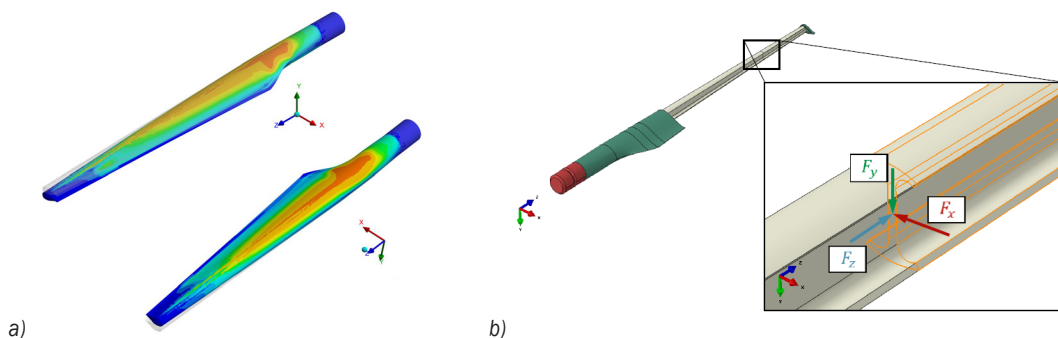


Fig. 7. FEM simulation of WTB: a) division of blade in critical regions; b) loading forces disposition

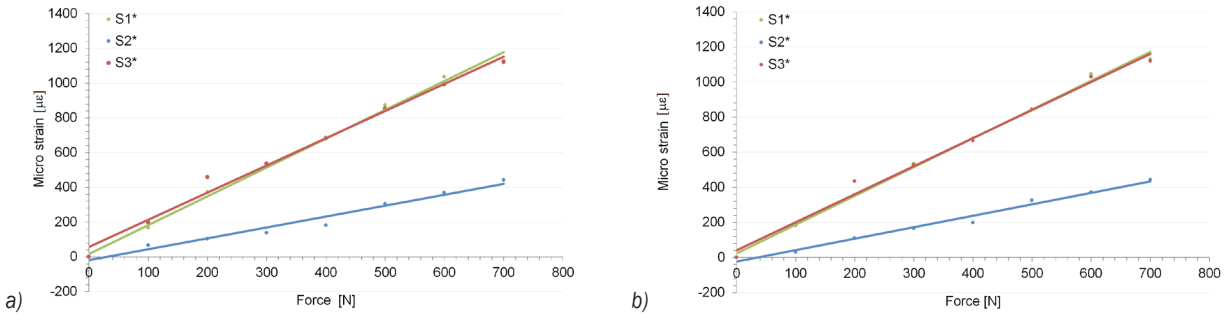


Fig. 8. Signal delivered by the three WRS placed in different critical regions of WTB: a) loading; b) unloading

1535 nm with strain sensitivity $7.8 \times 10^{-7} \mu\epsilon^{-1}$ and temperature sensitivity $6.5 \times 10^{-6} K^{-1}$.

This is connected at optical system FS22 Industrial BraggMETER HBM Germany coupled with PC. During the experiments, the temperature has been maintained constant at $22 \pm 1 \text{ }^\circ\text{C}$. The experimental test setup was performed according to [40], progressively loading/unloaded forces were applied.

Physically, stress concentration around the damage in the composite laminates can be directly observed from row sensor signal. The data processing has been made in Matlab 2014b, the temperature correction being made, the equipment indicating the temperature of fiber, too. Fig. 9a presents the raw data recorded by the device for different loadings. The relative variation of Bragg wavelength was determined in function of loading is presented in Fig. 9b showing that the relative variation of Bragg wavelength is linear. The dependency strain-load for WTB in a loading-unloading cycle for three sets of experimental measurement is presented in Fig 9. The same linear dependency strain-load can be shown, even the existence of a remnant stress at force

removal, indicating an accumulation of energy in WTB composite structure, preponderant in the resin.

The measurements using OF were carried on the same time with those using WRS sensors.

The sensor denoted T1 measures the deformations of the blade in the plane of I shape longeron, having height/width variable along the blade, T2 measures the deformations of blade shell closely to the trailing edge and T3 measures the deformations of blade shell closely to leading edge. The experimental data were used to calculate [40] maximum specific deformation ϵ_{max} , minimum specific deformations ϵ_{min} , acute angle from the axis θ , the maximum shear strain γ_{max} , maximum normal stress σ_{max} , minimal normal stress σ_{min} and tangential maximum stress τ_{max} .

Fig. 10 presents the plotting of σ_{max} , σ_{min} and τ_{max} for the 3SG for loading (Figs.10 a, c and e) and unloading (Figs. 10 b, d and f) until maximum force of 700 N. It can be observed that the high values of stresses with applied force appears in the region where sensor T3 is placed, this region being emphasized in FEM analysis too. The difference between maximum stress of loading and unloading is given due to the static conditions of measurements. The studied

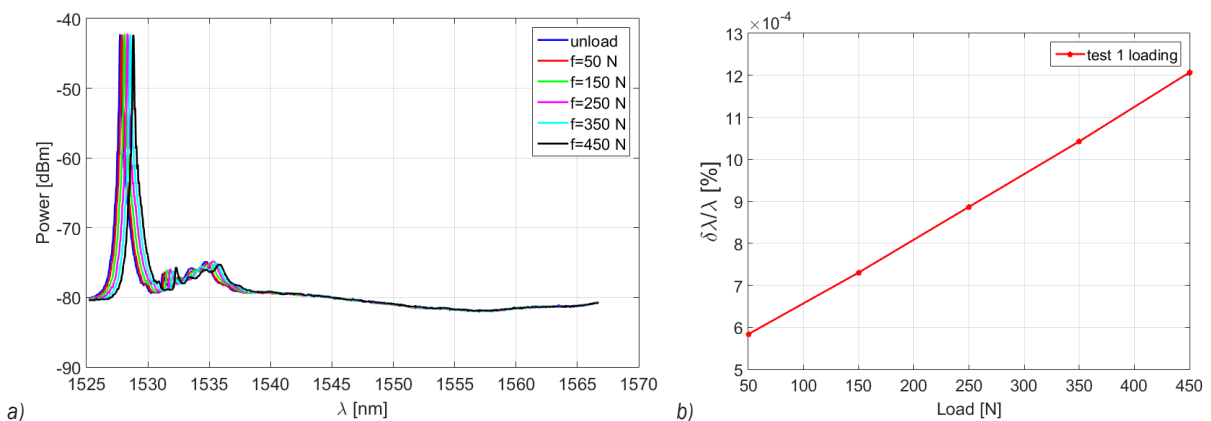


Fig. 9. FBG measurements: a) response to successive loading; b) relative variation of Bragg wavelength

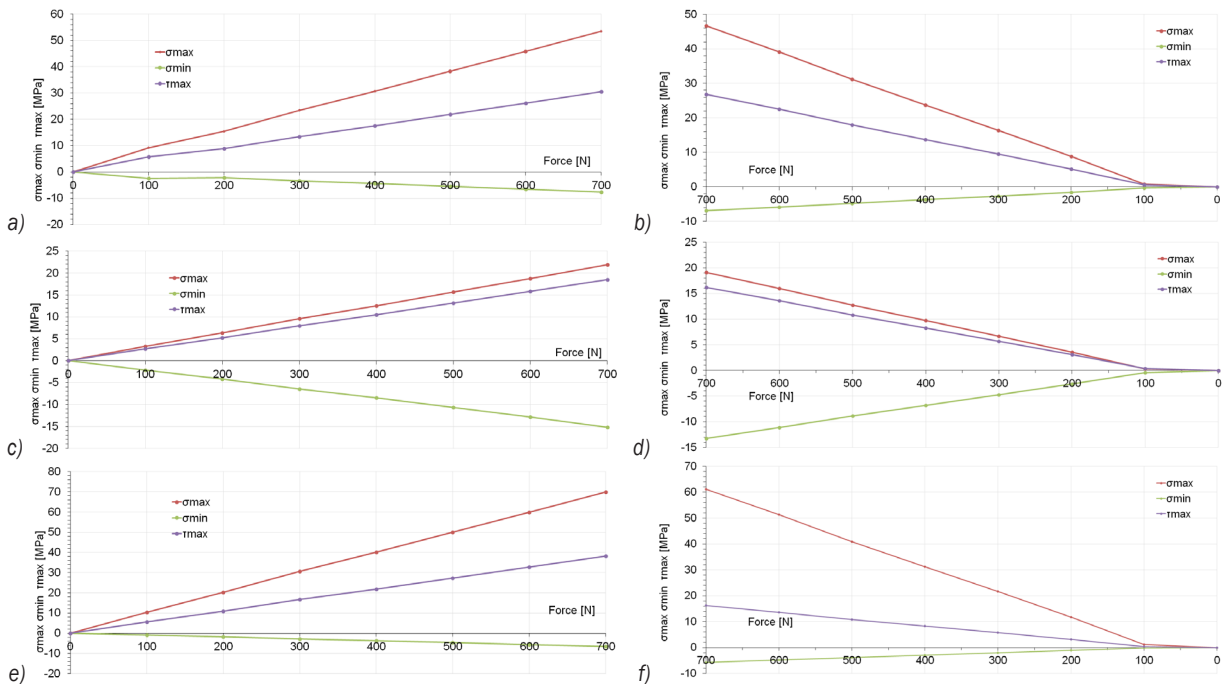


Fig. 10. Variation of stresses with force: a) rosette 1 - loading; b) rosette 1 - unloading; c) rosette 2 - loading; d) rosette 2 - unloading; e) rosette 3 - loading; f) rosette 3 - unloading

composite materials store the energy. The plots following the same profile shows that the tests were carried out in elastic range.

4 CONCLUSIONS

Monitoring of complex structures has become an economic necessity, the trend consisting in using of a lot of sensors (described in this paper, i.e. not only) to detect broken fibers which may occur and develop under moderated loads, or cracks and delamination due to low energy impacts, etc.

Practical applications demonstrates that, in order to avoid environmental disasters, it is necessary to establish diagnosis and prognosis methods, based on using information obtained from sensors constructed on known physical principles.

The monitoring is close related with nondestructive evaluation and the trend is to obtain real time information. Scalable WTB have been constructed and tested to loadings using WRS, OF-FBG and SG located in the maximum concentration stress zones.

The tests were carried on scalable models, in the further research the WRS sensors will be embedded, because in the frame of the project that sustains the paper, the blades will be employed into a demonstrator

to show the righteousness of solutions, reliability of correct diagnosis probability, prognosis, and evaluation of residual lifetime and maintenance management.

5 ACKNOWLEDGEMENTS

This paper is partially supported by Romanian Ministry of Research and Innovation under project Nucleus Program PN 2018 and under UEFISCDI Grant PN-III-P1-1.2-PCCDI-2017-0239.

6 REFERENCES

- [1] Wind Energy Targets for 2020 - 2030 (2015). Wind Europe, from <https://windeurope.org/about-wind/reports/wind-energy-scenarios-2030>, accessed 2018-01-24.
- [2] GE Renewable Energy (2018). from http://www.ge-energy.com/products_and_services/products/wind_turbines/ge_1.5_77_wind_turbine.jsp, accessed on 2018-01-24.
- [3] RWEA (2018). from <http://rwea.ro/cifre-cheie/>, accessed on 2018-01-24.
- [4] Xiang, D., Jiang, L., You, M., Shen, Y. (2017). Influence of quasi-steady, wind loads on the fatigue damage of wind turbine gearboxes. *Strojniški vestnik - Journal of Mechanical Engineering*, vol. 63, no. 5, p. 300-313, DOI:10.5545/sw-jme.2016.4224.
- [5] Chen, J., Yang, R., Ma, R., Li, J. (2016). Design optimization of wind turbine tower with lattice-tubular hybrid structure using particle swarm algorithm. *The Structural Design of Tall and*

- Special Buildings*, vol. 25, no. 15, p. 743-758, DOI:10.1002/tal.1281.
- [6] Kusiak, A., Song, Z. (2010). Design of wind farm layout for maximum wind energy capture. *Renewable Energy*, vol. 35, no. 3, p. 685-694, DOI:10.1016/j.renene.2009.08.019.
- [7] Kaidis, C., Uzunoglu, B., Amoiralis, F. (2015). Wind turbine reliability estimation for different assemblies and failure severity categories. *IET Renewable Power Generation*, vol. 9, no. 8, p. 892-899, DOI:10.1049/iet-rpg.2015.0020.
- [8] Yang, J., Peng, C., Xiao, J., Zeng, J., Xing, S., Jin, J., Deng, H. (2013). Structural investigation of composite wind turbine blade considering structural collapse in full-scale static tests. *Composite Structures*, vol. 97, p. 15-29, DOI:10.1016/j.compstruct.2012.10.055.
- [9] Hillmer, B., Borstelmann, T., Schaffarczyk, P., Dannenberg, L. (2007). Aerodynamic and structural design of MultiMW wind turbine blades beyond 5 MW. *Journal of Physics: Conference Series*, vol. 75, p. 012002, DOI:10.1088/1742-6596/75/1/012002.
- [10] Cajal, C., Santolaria, J., Samper, D., Garrido, A. (2015). Simulation of laser triangulation sensors scanning for design and evaluation purposes. *International Journal of Simulation Modelling*, vol. 14, no. 2, p. 250-264, DOI:10.1088/1742-6596/75/1/012002.
- [11] Ding, Y. Zhang, X. (2016). An optimal design method of swept blades for HAWTs. *Journal of Renewable and Sustainable Energy*, vol. 8, no. 4, p. 043303, DOI:10.1063/1.4961588.
- [12] Chehoury, A., Younes, R., Ilinca, A., Perron, J., (2015). Review of performance optimization techniques applied to wind turbines. *Applied Energy*, vol. 142, p. 361-388, DOI:10.1016/j.apenergy.2014.12.043.
- [13] González-Cruz, C., Jauregui-Correa, J., Herrera-Ruiz, G. (2016). Nonlinear response of cantilever beams due to large geometric deformations: Experimental validation. *Strojniški vestnik - Journal of Mechanical Engineering*, vol. 62, no. 3, p. 187-196, DOI:10.5545/sv-jme.2015.2964.
- [14] Hassanzadeh, A., Naughton, J.W., Kelley, C.L., Maniaci, D.C. (2016). Wind turbine blade design for subscale testing. *Journal of Physics: Conference Series*, vol. 753, no. 2, p. 022048, DOI:10.1088/1742-6596/753/2/022048.
- [15] Lee, H.G., Kang, M.G., Park, J. (2015). Fatigue failure of a composite wind turbine blade at its root end. *Composite Structures*, vol. 133, p. 878-885, DOI:10.1016/j.compstruct.2015.08.010.
- [16] Balageas, D., Fritzen, C.-P., Güemes, A. (eds.). (2010). *Structural Health Monitoring*, vol. 90, John Wiley & Sons, New York.
- [17] Yin, A., Lu, J., Dai, Z., Li, J., Ouyang, Q. (2016). Isomap and deep belief network-based machine health combined assessment model. *Strojniški vestnik - Journal of Mechanical Engineering*, vol. 62, no. 12, p. 740-750, DOI:10.5545/sv-jme.2016.3694.
- [18] Adams, D., White, J., Rumsey, M., Farrar, C., (2011). Structural health monitoring of wind turbines: method and application to a HAWT. *Wind Energy*, vol. 14, no. 4, p. 603-623, DOI:10.1002/we.437.
- [19] Lambert, J., Chambers, A.R., Sinclair, I., Spearing, S.M. (2012). 3D damage characterization and the role of voids in the fatigue of wind turbine blade materials. *Composites Science and Technology*, vol. 72, no. 2, p. 337-343, DOI:10.1016/j.compscitech.2011.11.023.
- [20] Mandell, J.F., Samborsky, D.D. (2012). *SNL/MSU/DOE Composite Material Fatigue Database*. Sandia National Laboratories, Albuquerque.
- [21] Wang, T. (2012). A brief review on wind turbine aerodynamics. *Theoretical and Applied Mechanics Letters*, vol. 2, no. 6, p. 062001, DOI:10.1063/2.1206201.
- [22] Schubel, P.J., Crossley, R.J. (2012). Wind turbine blade design review. *Wind Engineering*, vol. 36, no. 4, p. 365-388, DOI:10.1260/0309-524X.36.4.365.
- [23] Lachenal, X., Daynes, S., Weaver, P.M., (2013). Review of morphing concepts and materials for wind turbine blade applications. *Wind Energy*, vol. 16, no. 2, p. 283-307, DOI:10.1002/we.531.
- [24] Li, D., Ho, S.C.M., Song, G., Ren, L., Li, H. (2015). A review of damage detection methods for wind turbine blades. *Smart Materials and Structures*, vol. 24, no. 3, p. 033001, DOI:10.1088/0964-1726/24/3/033001.
- [25] Wind turbine accident compilation (2018). from <http://www.caithnesswindfarms.co.uk/fullaccidents.pdf>, accessed on 2018-02-10.
- [26] Grimberg, R., Tian, G.Y., Savin, A., Steigmann, R., Dobrescu, G.S. (2014). Electromagnetic metamaterial sensors for structural health monitoring. *Electromagnetic Nondestructive Evaluation (XVII)*, vol. 39, p. 3-10, DOI:10.3233/978-1-61499-407-7-3.
- [27] Xu, J., Dong, Y., Li, H. (2014). Research on fatigue damage detection for wind turbine blade based on high-spatial-resolution DPP-BOTDA. *Sensors and Smart Structures Technologies for Civil, Mechanical and Aerospace Systems*, vol. 906130, DOI:10.1117/12.2044840.
- [28] Takeda, S.-I., Aoki, Y., Nagao, Y. (2012). Damage monitoring of CFRP stiffened panels under compressive load using FBG sensors. *Composite Structures*, vol. 94, no. 3, p. 813-819, DOI:10.1016/j.compstruct.2011.02.020.
- [29] Kuang, K.S.C., Kenny, R., Whelan, M.P., Cantwell, W.J., Chalker, P.R. (2001). Residual strain measurement and impact response of optical fibre Bragg grating sensors in fibre metal laminates. *Smart Materials and Structures*, vol. 10, no. 2, p. 338-346, DOI:10.1088/0964-1726/10/2/321.
- [30] López-Higuera, J.M. (ed.) (2002). *Handbook of Optical Fibre Sensing Technology*. Wiley, New York.
- [31] Gouveia, C.A., Baptista, J.M. Jorge, P.A., (2013). Refractometric optical fiber platforms for label free sensing. *Current Developments in Optical Fiber Technology*, InTech, London, p. 345-373, DOI:10.5772/55376.
- [32] Daliri, A., Galehdar, A., Rowe, W.S., Ghorbani, K. John, S. (2012). Utilising microstrip patch antenna strain sensors for structural health monitoring. *Journal of Intelligent Material Systems and Structures*, vol. 23, no. 2, p. 169-182, DOI:10.1177/1045389X11432655.
- [33] Chen, T., Li, S., Sun, H. (2012). Metamaterials application in sensing. *Sensors*, vol. 12, no. 3, p. 2742-2765, DOI:10.3390/s120302742.
- [34] Pendry, J.B., Holden, A.J., Robbins, D.J., Stewart, W.J. (1999). Magnetism from conductors and enhanced nonlinear phenomena. *IEEE Transactions on Microwave*

- Theory and Techniques*, vol. 47, no. 11, p. 2075-2084, DOI:10.1109/22.798002.
- [35] Pendry, J.B., Holden, A.J., Stewart, W.J., Youngs, I. (1996). Extremely low frequency plasmons in metallic mesostructures. *Physical Review Letters*, vol. 76, no. 25, p. 4773-4776, DOI:10.1103/PhysRevLett.76.4773.
- [36] Savin, A., Steigmann, R., Dobrescu, G.S. (2014). Metamaterial sensors for structural health monitoring. *Proceedings of the ASME 12th Biennial Conference on Engineering Systems Design and Analysis*, p. 25-27, DOI:10.1115/ESDA2014-20596.
- [37] Vishay (2014). Strain gage rosettes: selection, application and data reduction, Tech Note TN-515, from <http://www.vishaypg.com/docs/11065/tn-515.pdf>, accessed on 2018-01-24.
- [38] FS22 Industrial BraggMETER (2017). *Static and Dynamic Optical Interrogators, User Manual*, HBM Germany Darmstadt.
- [39] ASTM D5868 - 01(2014). Standard Test Method for Lap Shear Adhesion for Fiber Reinforced Plastic (FRP) Bonding, ASTM International, West Conshohocken, DOI:10.1520/D5868-01R14.
- [40] Sciammarella, C.A., Sciammarella, F.M., (2012). Strain gage rosettes: selection, application and data reduction. *Experimental Mechanics of Solids*, John Wiley & Sons, New York, p. 111-121, DOI:10.1002/9781119994091.ch5.

Nondestructive Determination of Stresses in Steel Components by Eddy Current Method

Valentyn Uchanin^{1,*} – Sergej Minakov² – Giuseppe Nardoni³ – Orest Ostash¹ – Sergej Fomichov²

¹Karpenko Phisico-Mechanical Institute of National Academy of Sciences, Ukraine

²Kyiv Politechnical Institute, Ukraine

³I&T Nardoni Institute, Italy

Nondestructive eddy current (EC) method for evaluation of stresses in ferromagnetic steel components based on the stress-induced magnetic anisotropy (MA) changes was investigated. The proposed method is based on the rearrangement of the magnetic domains under stresses due to the reverse magnetostrictive effect (Villari effect). For evaluation of stresses special EC probe was developed. Investigations were carried out with the application of the conventional testing machine for tensile loading and the specially developed experimental set-up for four-point loading for creation the adjusted tensile and compressive stresses on different sided of the loaded specimen. From results obtained some specific properties were determined: the magnetic-mechanical hysteresis existence and the invariance feature in relation to the structural state of the material. The last result can create the outlook for stress measurement independently of the structural state of material as opposed to other known magnetic methods based on coercivity or Barkhausen noise measurements. Two original practical applications of the MA technique for stress determination were realized: the evaluation of the welding-induced residual stresses and the estimation of stresses in the steel bridge framework during the launching to the pillars.

Keywords: eddy current, magnetic anisotropy, applied and residual stresses, tensile, compressive, magnetic-mechanical hysteresis, welding, bridge framework

Highlights

- Eddy current method for determination of stresses in ferromagnetic steel components based on MA changes under the stress influence.
- Experimental results concerned with peculiarities of the EC probe signal changes under the tensile and compressive stress influence.
- Results obtained show the magnetic-mechanical hysteresis existence and the invariance feature of the investigated method in relation to the structural state of the material.
- Results of new practical applications, such as: the evaluation of the welding-induced residual stresses and the estimation of stresses in the steel bridge framework during the launching to the pillars.

0 INTRODUCTION

Applied and residual stresses can influence the operable state of the structures and components. Especially it is important for welding, because shrinkage, quenching and phase transformations during the welding process create different distributions of residual stresses. Welding-induced tensile residual stresses provoke the brittle fracture and stress-corrosion cracking, which significantly reduce the fatigue life of welded structures in service [1] and [2].

Different destructive and nondestructive methods have been developed to estimate the stress state of the material in different applications [1] to [3].

The nondestructive techniques based on the magnetic phenomena concerned with Barkhausen noise or hysteresis loop parameters evaluation has been applied for determination of the stresses in the ferromagnetic steel components [4] to [9]. These methods provide the possibility of non-contact, reliable

and fast inspection with high repeatability of the results obtained. Methods based on Barkhausen noise technique were successfully applied for evaluation the residual stress state in steel weldment [4] to [7]. The effectiveness of Barkhausen noise method for stress measurement was validated by comparative investigations [7] and [8]. The original method based on the combined application of Barkhausen noise and coercive field strength techniques possible to separate the information about structural and stress state of material was proposed in [9]. These methods can be characterized by comparatively low operational frequencies (can be considered as constant) of applied magnetic fields.

The methods based on magnetic elastic (including the magnetic anisotropy (MA)) probes and alternating electromagnetic field application also can be applied for stress determination in the surface layers of the steel components [10] to [21]. In this case, the depth of evaluated material is strongly limited by skin-effect influence due to higher operational

frequency application. The depth of penetration of electromagnetic field can be changed by the choice of the operational frequency.

In majority publications, the different types of the four-pole probes were applied as primary sensors in MA stress measurement techniques [11] to [19]. The four-pole probe with cross-shaped indivisible core and two excitation and two sensing coils installed on opposite poles (legs) of the core is considered to be one of the most useful among the MA probes [11] and [12]. Other type of the four-pole probe with cross-shaped indivisible core was analyzed in [13]. On each pole (leg) of this probe one excitation coil and one sensing coil are installed. Therefore, this probe consists of 4 excitation and 4 sensing coils. In a many publications the probes for MA based stress measurement were composed of the two coils mounted on the two separated U-shaped (or yoke type) cores, which are positioned mutually-perpendicular each other [14] to [19]. One coil (excitation coil) commonly is connected with the harmonic generator output. And other coil is a sensing coil. Such type probes are interacted with inspected surface by 4 poles situated in the corners of a regular tetragon.

Presented methods are based on the magnetic permeability changes in the ferromagnetic material due to the rearrangements of the magnetic domains under the stresses concerned with the reverse magnetostrictive effect (Villari effect). Furthermore, the tensile and compressive stresses have an influence on the magnetic domains alignment in a different way as presented schematically in Fig. 1. For ferromagnetic material under stress, the elliptical diagram for angular distribution of directional permeability was assumed [17] and [18].

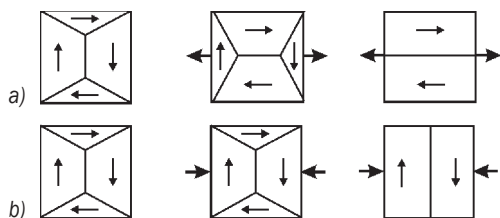


Fig. 1. Rearrangements of magnetic domains under the influence of a) tensile and b) compressive loadings

Due to high enough operational frequencies the MA methods can be considered as one of the versions of the EC method. For such approach, the big experience of EC method development can create other fruitful consideration. In this paper, the investigations of EC method with new type of stress sensitive EC probe are presented. The signals

of developed EC probe under the stresses were investigated with conventional EC flaw detector to underline the EC nature of investigated MA method. Some new results of the practical applications, such as the determination of residual stress distribution near the circumference pipeline welding and the estimation of stresses in the bridge framework walls during the launching procedure, also are presented.

1 EDDY CURRENT PROBE, INSTRUMENTATION, SPECIMENS AND INVESTIGATION PROCEDURES

Our comparative investigations show that better performance for stress induced MA changes detection can be achieved by double differential type probe [20] and [21]. This type of probes is composed of two identical excitation coils 1 and two identical sensing coils 2, which are situated in the tetragon corners, as it is shown on Fig. 2. For presented investigation stress sensitive double differential MDF 180I type EC probe with 18 mm operational diameter was produced. In this probe, all coils are installed on 4.3 mm diameter ferrite cores [20]. Excitation coils 1 of this probe are connected in series each other and oriented in order to create the identical and opposite primary electromagnetic fields as it is shown in Fig. 3. Due such design double differential type EC probes have some remarkable peculiar properties in the distribution of primary electromagnetic field and eddy currents, such as the existence of the characteristic neutral plane, in which the vertical component of summarized primary electromagnetic field is equal to zero. Due such peculiarity the high sensitivity is obtained in combination with high level of lift-off suppression [20].

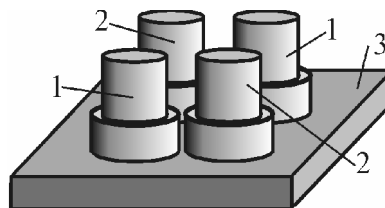


Fig. 2. MA sensitive double differential type EC probe:
1 - ferrite cores with excitation coils,
2 - ferrite cores with sensing coils, 3 - inspected object

Sensing coils 2 are oriented to be sensitive to the vertical component of the electromagnetic field and are installed in neutral plane, where this component for isotropic media is equal to zero. Due to the opposite connection of sensing coils 2 (Fig. 2) the double differential type of signal response is realized.

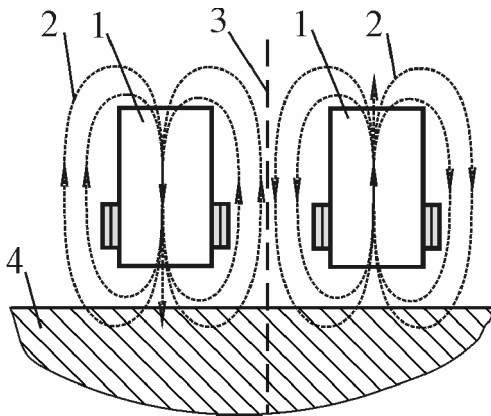


Fig. 3. The distribution of primary electromagnetic field and eddy currents in the double differential type EC probes:
 1 - ferrite cores with excitation coils, 2 - primary field,
 3 - neutral plane, 4 - inspected object

Conventional Eddycon VD3.81 type EC flaw detector (Fig. 4) was applied for observation of the EC probe signal response changes during the loading [21].



Fig. 4. EC flaw detector Eddycon VD3-81

Structural scheme of Eddycon VD3-81 flaw detector (Fig. 5) consists of: EC probe 1; excitation generator 2; input multiplexer 3; preamplifier 4; vector signal summarizer 5; balancing generator 6; amplifier 7; ADC 8; programmed logic integrated chip 9; processor 10; display 11; USB controller 12; audio controller 13; keyboard 14; sound alarm generator 15; alarm LED 16.

Eddycon VD 3-81 flaw detector permits to represent the EC probe signal responses in complex plane on the operational frequencies from 50.0 Hz to 12.0 MHz. The balancing generator 6 produce the balancing sinusoidal signal for vector summarizer 5 under the control of the programmed logic integrated chip 9. The amplitude and phase of this balancing signal was choosing to set zero signal response for probe situated on the unloaded specimen. For our investigation it is very useful the possibility to monitor

the hodographs of signal response in complex plane during the specimen loading and unloading.

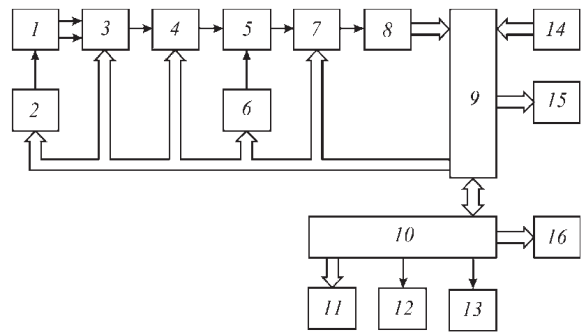


Fig. 5. Structural scheme of Eddycon VD 3-81 type flaw detector

Experimental investigations were carried out with the application of the conventional testing machine for tensile loading and the specially developed set-up for four-point loading by pure bending scheme. Stress values were calculated with the application of the displacement indicator readout (scale division value, 0.01 mm), which indicates the deformation of specimen in central point under the different level of applied force P . The indicator was calibrated in stress units preliminarily (before the investigations) by force dynamometer application. Tensile and compressive stresses were obtained on different sides of specimen due to four-point loading scheme application. It is important, that the diagram of bending moments M and stresses in the center of specimen (between the points of the force application P on Fig. 6) don't changed. Transverse forces Q in this area also are equal to zero. In that way the EC probe signal responses are not influenced by the position of the probe within this area along the specimen. The influence of the specimen edge was eliminated by accurate probe positioning.

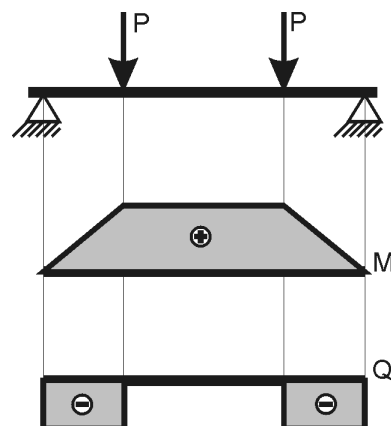


Fig. 6. Four-point loading scheme of pure bending and diagrams for the bending moments M and transverse forces Q

Specimens for investigations were made from low carbon and middle carbon steels.

The specimen made of low-carbon steel (mass %: 0.10 C; 0.42 Si; 1.47 Mn) was 450 mm long, 8 mm thick and 60 mm wide. This specimen was annealed before loading at 720 °C during 1 h (mainly ferrite structure with yield strength $\sigma_{YS} = 305$ MPa) to remove the potential residual stresses and investigated using set-up for four-point bending (Fig. 6).

Two specimens made of middle-carbon steel (mass %: 0.66 C; 0.29 Si; 1.02 Mn; 0.12 Cr) were 150 mm long, 3 mm thick and 30 mm wide. These specimens were used to investigate the influence of the steel microstructure on the EC probe signal response under the tensile loading. The first specimen was annealed at 830 °C during 2 h and contains mainly pearlite structure ($\sigma_{YS} = 560$ MPa). The second specimen was quenched (from 830 °C, cooling in oil) and tempered (at 380 °C during 2 h) and contains mainly troostite structure ($\sigma_{YS} = 1510$ MPa).

During the experiments the EC probe was mounted in middle part of the specimen in the unloaded state (before the loading) by spring bracket to minimize the clearance between specimen surface and the EC probe to zero. After that, the EC probe signal response was balanced automatically by the proper procedure of vector summation, which is typical for modern EC flaw detector. Due this procedure the initial components of the material electrophysical properties anisotropy, concerned with material texture and specimen form, were eliminated. After the balancing, the original point of signal response in complex plane on the flaw detector display was located in the center (marked by number 1 in Fig. 7). Then the specimen was loaded to create the tensile or compressive stresses. Before the investigation, the direction of hodograph for tensile loading was oriented to go vertically up by usual for EC flaw detector operation of phase rotation. The signal response changes during the specimen loading and subsequent unloading were recorded in complex plane in the form of hodograph or the increments of the signal amplitude were registered.

2 RESULTS AND DISCUSSION

2.1 The Influence of Tensile and Compressive Loading on the EC Probe Signal Response

In this investigation the low-carbon steel specimen was loaded to create the tensile and compressive stresses from unloaded state up to 225 MPa. For this purpose the EC probe was mounted on different sided

of specimen loaded by four-point scheme. The EC probe signal response hodographs in complex plane obtained on operational frequencies 5 kHz and 50 kHz are presented in Fig. 7.

We can notice that hodographs for 5 and 50 kHz are very similar. During the loading, the ends of the signal vector were moving from the initial zero point along the hodograph lines to points concerned with maximal signal amplitude. When the specimen was unloaded the ends of signal vector returned to initial zero point by the same trajectory.

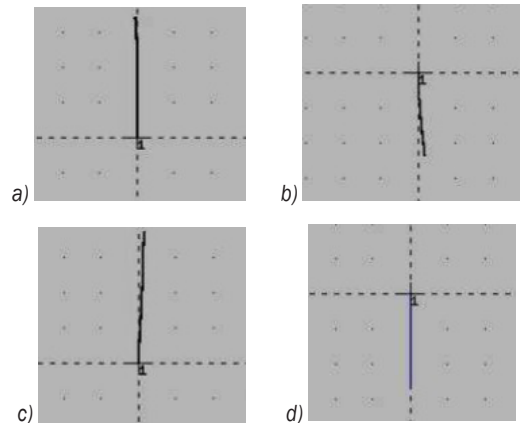


Fig. 7. Hodographs of EC probe signal responses in complex plane for a) and c) tensile and b) and d) compressive stresses on operational frequencies a) and b) 5.0 and c) and d) 50.0 kHz

One might notice that hodographs obtained for tensile and compressive stresses have opposite directions in the complex plane. This peculiarity enables the indication of stress type (tensile or compressive) if the balancing procedure was carried out on the specimen with really unloaded state. Results obtained show that the developed EC probe is sensitive to stresses even when high enough operational frequency (50 kHz) was applied.

The dependences of EC probe signal amplitude U_σ (in volts) on the tensile and compressive stresses σ on the operational frequency 5.0 kHz are presented in Figs. 8 and 9. The EC probe signal amplitudes were measured during loading trials up to 225 MPa and subsequent unloading to fully-unloaded state.

Presented results demonstrate high sensitivity of the developed double differential type EC probe to tensile and compressive stresses and the magnetic-mechanical hysteresis existence. The nature of magnetic-mechanical hysteresis can be explained by the influence of mechanical hysteresis combined with the influence of magnetic hysteresis.

It is clear that observed hysteresis can produce the relevant errors during the stress measurements.

Therefore, some methods to suppress concerned with the hysteresis errors were developed [14], [15] and [19]. On the other hand, the existence of such kind of errors is not essential for comparative inspection, when the stress distribution or the difference of the stresses on the specified points of the inspected surface is more informative, than the absolute value of stress.

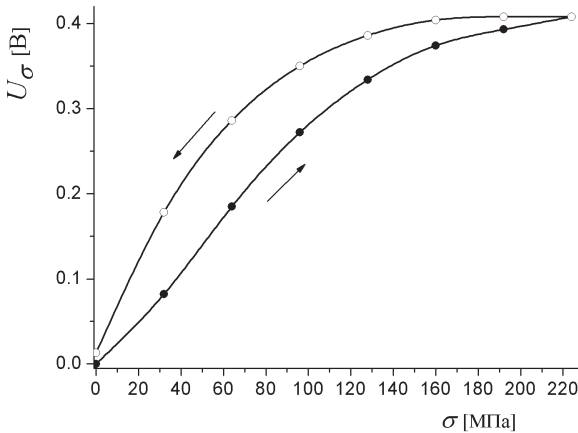


Fig. 8. Changes in EC probe signal amplitude during tensile loading (●) and subsequent unloading (○)

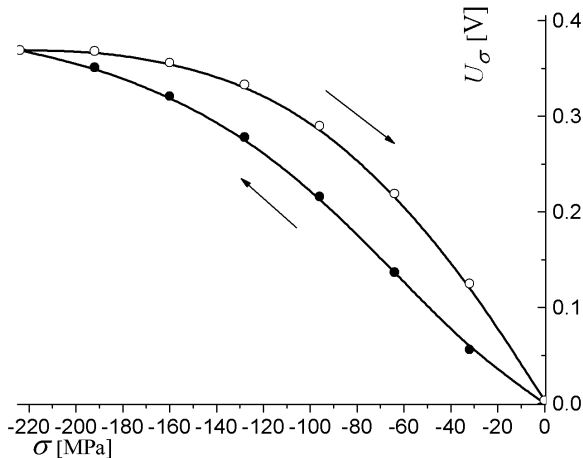


Fig. 9. Changes in EC probe signal amplitude during compressive loading (●) and subsequent unloading (○)

2.2 Investigation of the Steel Microstructure Influence

For next experiment two middle-carbon steel specimens were heat treated in different ways to obtain the different microstructure of steel. These specimens were loaded on the tensile machine up to 500 MPa. Stress-induced changes in EC probe signal response amplitude U were evaluated (Fig. 10). Here only loading branches of relative characteristics were recorded.

We can notice that the experimental points for loading branch are located on the same graph for the different structural state of specimen material. So, these results demonstrate the invariant feature of MA method in relation to the structural state of the steel. In other words – MA method is insensitive to structural state of stressed steel. Certainly, next investigations are needed to check this preliminary conclusion for different structural states and grades of steel.

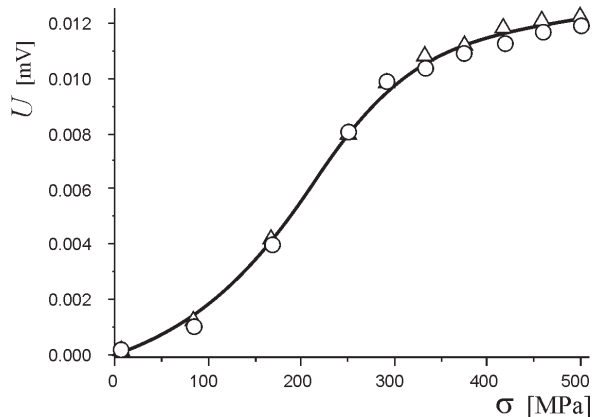


Fig. 10. Dependences of EC probe signal U on tensile stress σ in annealed (Δ) and quenched with tempering (\circ) states

The last result can create the outlook for stress measurement independently of the structural state of material as opposed to other known magnetic methods based on coercivity or Barkhausen noise measurements.

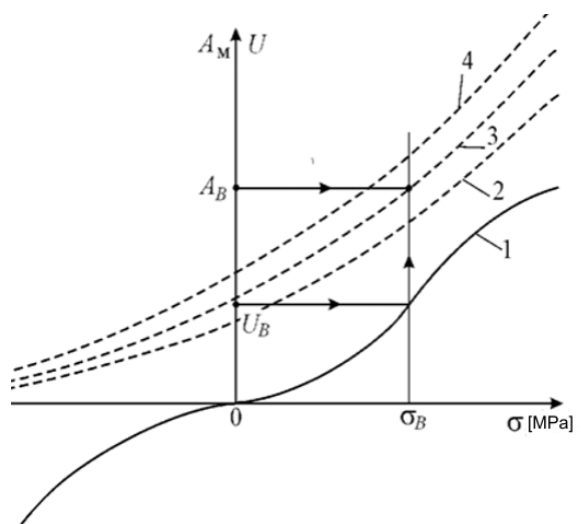


Fig. 11. Complex analysis of the Barkhausen noise and MA sensitive EC probe signals for separable estimation of structural and stress state

The idea of possible algorithm for separable structural and stress state determination based on the complex analysis of Barhausen noise technique (for example) and MA sensitive EC probe signals is shown in schematic generalized form in Fig. 11 [22]. The stress σ_{MA} can be estimated from measured value of MA probe signal amplitude U_{MA} using the dependence $U=f(\sigma)$ (curve 1). Then, from measured Barhausen parameter A_B and known stress σ_{MA} from the the dependences of Barhausen maximal amplitude A on the stresses for different structural state (curves 2, 3 and 4) the relevant curve, which characterized the structural state of inspected material, can be determined (curve 3 in our example).

3 APPLICATIONS

Two original applications of the MA method for stress determination were proposed and realized. In these applications, the possibility of contactless measurements and simple removability of EC probe create new possibilities for nondestructive inspection.

3.1 Determination of Residual Stressed in Welding

EC method based on stress-induced MA changes can be applied for estimation of residual stresses in welding. Next result was obtained by experimental pipeline application (168 mm in diameter and 22 m long with circular weld joints every 1000 mm). The width of heat affected zone in welding was estimated about 70 mm.

It was determined the distribution of stresses with distance l (Fig. 12) in the direction perpendicular to welding line.

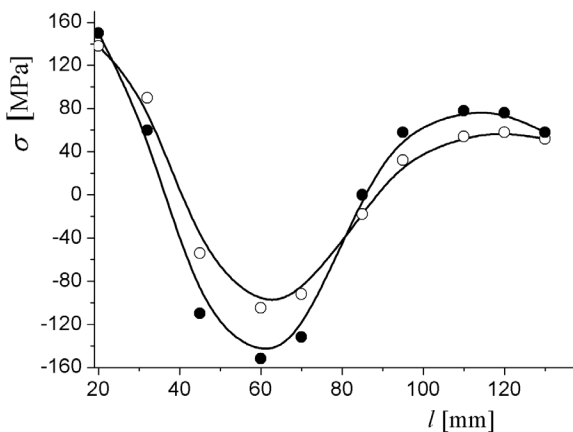


Fig. 12. Distribution of residual stresses in tube circular welding obtained by EC (○) and hole-drilling (●) methods

The EC MA meter was preliminary calibrated by four-loading set-up application (Fig. 6). The operational frequency is 700 Hz. The depth of EC penetration is estimated about 0.8 mm to 0.9 mm. The results obtained by EC method were compared with the traditional hall-drilling method. The drill diameter is 1.6 mm. The depth of drilling is 0.8 mm.

Presented results show the specific distribution of residual stresses in welding area [3].

3.2 Determination of the Stresses in Bridge Framework Walls during the Launching to the Pillars

Proposed MA technique of stress measurement was applied to estimate the balance between the different sidewalls during the bridge framework launching to the pillars to prevent possible disaster [23]. The proposed method was tested at the time of the launching the bridge framework during the building of the bridge across the Dnieper river in Kiev. The bridge framework has 2 box sections with dimensions 3240 mm × 2360 mm and 12 mm wall thickness. For stress determination two EC probes were mounted on the extreme opposite framework walls in compressed area (200 mm from the framework edge) directly above the expansion pedestal area. After every framework displacement (about 1 m) the console length of bridge framework L was increased and the point of measurement was displaced also. The EC probes were oriented to estimate the horizontal compressive stresses, which have maximal value in the point above the expansion pedestal.

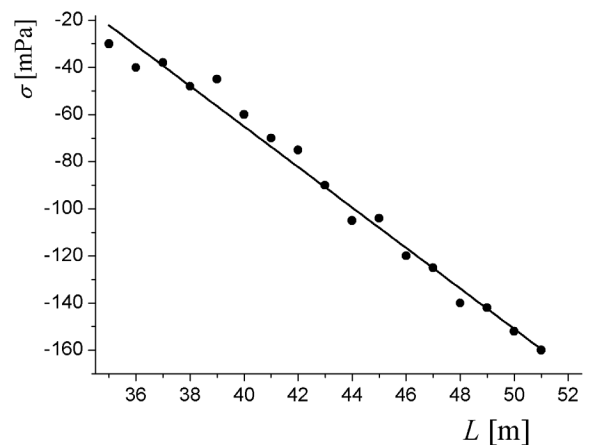


Fig. 13. The dependence of the measured stress σ on the console length L

The dependence of measured stress σ on the console length L (Fig. 13) shows that the compressive stresses in the expansion pedestal area are increased

linearly during the process of launching. The procedure of the measurement of stress changes in the bridge framework wall at the time of the launching is presented in Fig. 14.



Fig. 14. The measurement of stress changes in the bridge framework sidewall at the time of the launching

Simple removability of EC probe during the launching process and the possibility of stress determination without the direct contact with the surface of the inspected component are the main advantages of EC method in comparison with the tensometric strain-gage testing. The monitoring of the changes of the stresses in framework walls during the launching process permits to prevent possible disaster.

4 TASKS FOR FUTURE WORKS

Future investigations and elaborations are concerned with next topics:

1. The investigation of the nature of the magneto-mechanical hysteresis with the purpose to minimize the relevant errors;
2. To investigate and generalize the invariant property of MA method in relation to the structural state for different grade steels.

5 CONCLUSIONS

1. The hodographs of the signal responses of the developed EC probe in complex plane under the influence of tensile and compressive stresses in ferromagnetic steel were investigated. The opposite direction of hodographs for tensile and compressive stresses was shown. This peculiarity creates the possibility to determine the type of stress (tensile or compressive). The existence of

the magneto-mechanical hysteresis even in the elastic loading range also was shown both for tensile and compressive loading.

2. The invariant property of magnetic anisotropy EC probe signal under the tensile stress influence in relation to the structural state of ferromagnetic steel was shown. The idea of stress and structural state of material estimation was shown.
3. Two practical applications of the MA method for stress determination were presented: the determination of the residual stresses in pipeline welding area and applied stresses in the bridge framework walls during the process of framework launching to the pillars.

5 REFERENCES

- [1] De, A., DebRoy, T. (2011). A perspective on residual stresses in welding. *Science and Technology of Welding and Joining*, vol. 16, no. 3, p. 204-208, DOI:10.1179/136217111X12978476537783.
- [2] Nitschke-Pagel, T., Wohlfahrt, H. (2002). Residual stresses in welded joints – Sources and consequences. *Material Science Forum*, vol. 404-407, p. 215-226, DOI:10.4028/www.scientific.net/MSF.404-407.215.
- [3] Withers, P.I., Turski, M., Edwards, L. Bouchard, P.J., Buttle, D.J. (2008). Recent advances in residual stress measurement. *International Journal of Pressure Vessels and Piping*, vol. 85, no. 3, p. 118-127, DOI:10.1016/j.ijpvp.2007.10.007.
- [4] Vengrinovich, V., Tsukerman, V., Denkevich, Y., Bryantsev, D. (2006). The new parameters to characterize internal stresses via Brakhausen Noise. *Proceedings of the 9th European Conference on NDT*, p. 1-7.
- [5] Yelbay, I.H., Cam, I., Gur, H. (2010). Non-destructive determination of residual stress state in steel weldment by magnetic Barkhausen noise technique. *NDT & E International*, vol. 43, no. 1, p. 29-33, DOI:10.1016/j.ndteint.2009.08.003.
- [6] Gur, H., Erikan, G., Batıgün, C., Çam, I. (2016). Investigating the effect of subsequent weld passes on surface residual stresses in steel weldments by magnetic Barkhausen noise technique. *Materials Evaluation*, vol. 74, no. 3, p. 408-423.
- [7] Vourna, P., Ktena, A., Tsakiridis, P.E., Hristoforou, E. (2015). A novel approach of accurately evaluating residual stress and microstructure of welded electrical steels. *NDT & E International*, vol. 71, p. 33-42, DOI:10.1016/j.ndteint.2014.09.011.
- [8] Zerovnik, P., Grum, J. (2006). Comparative measurements of residual stresses with the method based on the magnetic Barkhausen noise and relaxation method. *International Journal of Microstructure and Materials Properties*, vol. 1, no. 3-4, p. 321-333, DOI:10.1504/IJMP.2006.011647.
- [9] Stuecker, E., Hofer, G., Koch, D., Guenes, U. (1989). *Method and Apparatus for Measuring and Precisely Locating Internal Tensile Stresses in Hardened Regions of Components by Measuring Coercive Field Strength and Barkhausen Noise Amplitude*, USA Patent no. 4881030. USPTO, Washington.

- [10] Langman, R.A., Mutton, P.J. (1993). Estimation of residual stresses in railway wheels by means of stress-induced magnetic anisotropy. *NDT & E International*, vol. 26, no. 4, p. 195-205, DOI:10.1016/0963-8695(93)90474-9.
- [11] Liu, H.S., Yin, C.H., Zhang L., Mao, X.B., Miao, X.X., Lu, A.H. (2009). Improvement of magnetic residual stress measurements based on Fourier transform. *Material Science and Technology*, vol. 25, no. 6, p. 743-746, DOI:10.1179/174328408X322187.
- [12] Kuo, S.-K., Lin, S.-Y., Lu, C.-Y. (2012). Characterization of magnetic field rotation of steel sheet under uniaxial stress. *Measurement*, vol. 45, no. 5, p. 1239-1245, DOI:10.1016/j.measurement.2012.01.013.
- [13] Grigoryan, S.G. (2012). A method of determination of the components of tensor of mechanical stresses in products from ferromagnetic materials. *Russian Electromechanics*, no. 1, p. 28-33. (in Russian)
- [14] Zhukov S.V., Zhukov V.S. (1997). *Device for Measurement of Mechanical Stresses in Metal Product*. Russian Patent no. 2079825, Russian Patent Office, Moscow. (in Russian)
- [15] Zhukov, S.V., Zhukov, V.S., Kopytsa, N.N. (2002). *Method for Determination of Mechanical Stresses and Device of Its Realization*. Russian Patent no. 2195636, Russian Patent Office, Moscow. (in Russian)
- [16] Fomichov, S., Minakov, S., Michalko, S., Yaremenko, M., Minakov, A. (2009). The determination of the force action on the pipeline by the longitudinal stresses distribution analyzing. *Technical Diagnostics and Nondestructive Testing*, no. 2, p. 11-14. (in Russian)
- [17] Sakai Y., Unishi, H., Yahata, T. (2004). Non-destructive method of stress evaluation in linepipes using magnetic anisotropy sensor. *JFE Technical Report*, no. 3, p. 47-53.
- [18] Liu, H., Dun, C., Dou, L., Yang, W. (2011). Theoretical analysis of magnetic sensor output voltage. *Journal of Magnetism and Magnetic Materials*, no. 323, no. 12, p. 1667-1670, DOI:10.1016/j.jmmm.2011.01.034.
- [19] Kishimoto, S., Kobayashi M., Kodaira Y., Kobayashi, M., Yamada, H. (1990). Non-contact stress measurement of rail steel using a magnetic anisotropy sensor. *IEEE Translation Journal on Magnetics in Japan*, vol. 5, no. 9, p. 762-767, DOI:10.1109/TJMJ.1990.4564337.
- [20] Uchanin, V. (2013). *Surface Double Differential Type Eddy Current Probes*. Spolom, Lviv. (in Ukrainian)
- [21] Uchanin, V., Lutsenko, G., Opanasenko, A., Dzhagianian, A. (2016). PROMPRYLAD family of eddy current flaw detectors – from simple to more complicated. *Proceedings of the 19th World Conference on NDT*, p. 1-8.
- [22] Uchanin, V., Minakov, S., Ostash, O., Bezlyudko, G., Minakov, A. (2015). *Method for Complex Electromagnetic Testing of Structural and Stress State of Ferromagnetic Materials*, Ukrainian patent no. 100379, Ukrainian Intellectual Property Institute, Kyiv. (in Ukrainian)
- [23] Uchanin, V., Minakov, S., Fomichov, S., Minakov, A., Bobin, B. (2017). *Method of Framework Launching during the Bridge Building*, Ukrainian Patent no. 116454, Ukrainian Intellectual Property Institute, Kyiv. (in Ukrainian)

Mechanical and Surface Properties of Lignocellulosic Fibres Reinforced Composites

Mariana Domnica Stanciu^{1,*} – Adriana Savin² – Silviu Marian Nastac³

¹Transilvania University of Brasov, Department of Mechanical Engineering, Romania

²National Institute of Research and Development for Technical Physics, Nondestructive Testing Department, Romania

³Dunarea de Jos' University of Galati, Engineering and Agronomy Faculty, Romania

The aim of this paper is to evaluate the mechanical and surface properties of lignocellulosic fibres reinforced composite before and after photo-degradation exposure. This leads to decrease the mechanical properties of composite as modification of hydrophobic behavior of matrix. In the study, the lignocelluloses specimens were obtained by mix polyester resin type 440- M888 POLYLITE, in a volume percentage of 25 %, with different wood particles classified by size classes. The samples were exposed to UV-A radiations with a wavelength λ of 365 nm for 168 hours (7 days). The evaluation of the surface energy was carried out by the θ contact angle method. For mechanical properties, the dynamic mechanical analysis (DMA) was used to determine the variation of storage and loss modulus. The results showed that UV radiation induced structural morphological instability, which leads to hydrophilic effect. The loss modulus recorded an increasing with increases of wood particles sizes.

Keywords: lignocelluloses composite, storage modulus, loss modulus, surface energy, contact angle method

Highlights

- New composite materials reinforced with hemp fibers and wood particles are studied.
- Mechanical and surface properties before and after UV radiation are analyzed.
- Effect of UV exposure of lignocelluloses composites in terms of the surface energy, morphological characteristics determined using AFM and contact angle method.
- The variations of the storage (elastic) modulus (E'), loss (viscous) modulus (E'') are obtained before and after photo and thermal exposure.

0 INTRODUCTION

The advantages and disadvantages of natural fibers as hemp, sisal, jute, wood, and flax have been studied in terms of mechanical properties, durability, cohesion between filler and matrix. The development of natural fiber reinforced biodegradable polymer composites promotes the use of environmentally friendly materials [1]. The new materials derived from biodegradable renewable sources are considered as partial solution to environmental pollution caused by the large volume of waste [2]. Even though the fiber determines the mechanical properties like elastic modulus or strength, the matrix provides the physical and chemical durability by protecting the fiber from environmental influences [3]. The use of lignocelluloses composite with polymer matrix in the environment with UV radiation can cause photo-degradation which lead to a weakening of the material and micro-cracking of the matrix [4] and [5]. Photo-degradation is the main effect of UV environmental radiation on polymeric materials, which is shown by the following phenomena: breaking chemical bonds between the polymer chains, which leads to the formation of free radicals by dissociating C-H bonds

from the polymer chains and to the oxidation of its surface because of peroxide radicals [6]. In addition, exposure to UV radiation can make the material more sensitive to the action of other factors (i.e. humidity) [7]. The hydrophilicity is one great drawback when using lignocelluloses fibers as reinforcement in polymer composites. Many approaches studied the tendency of interfacial strength and dimensional stability of bio-composite as results of UV action [8] and [9].

The paper is focused on the photo-degradation mechanism, which influences the surface energy of the lignocelluloses composite. The evaluation of the surface energy of the composite lignocelluloses materials was carried out by the θ contact angle method identifying the hydrophilic/hydrophobic properties of them. Because of the poor interfacial adhesion between fibers and polymers which leads to limitation of natural fibers reinforcement, Azwa et al. [10] studied the improvement of composite behavior due to addition of coupling agent.

The effect of the oak particle size on the mechanical and morphological properties has been studied [6]. Mechanical properties of wood plastic composites (WPC), determined by tensile and

bending tests show an increase of elasticity modulus E and yield strength simultaneous with the increasing of the particle size [11]. These mechanical parameters are lower for composites with larger particles [12] and [13]. The type of resin using in composite plays an important role in increasing the mechanical properties (tensile, bending and shear), noticed by [14] and [15]. Until date, the references about modification of mechanical and morphological properties of lignocellulosic composite because of UV radiation are relatively limited. The aim of the current study is to compare the surface and mechanical properties of lignocellulosic composites before and after ultraviolet exposure.

1 MATERIALS AND METHODS

1.1 Materials

Two types of composites were studied. The specimens for DMA test were cut from the plates taking into account the recommendation of the European standards for the flexural test by using the method of the three points [16]. The first studied lignocellulosic composite is a commercial one used in automotive industry made from hemp mat and polyurethane resin (RAIGITHANE 8274/RAIGIDUR CREM), with 50 % percentage of reinforcing natural fibres. The second is a new types of composites that contains oak particles

with volume fibre fraction of 25 %. The oak particles were separated by means of grading sieves according to the criterion of size: wood particles smaller than 0.04 mm, coded L 0.04; wood particles between 0.04 mm to 0.1 mm, coded L 0.1; wood particles between 0.1 mm to 0.2 mm, coded L 0.2; wood particles between 0.2 mm to 0.4 mm, coded L 0.4 and wood particles between 0.4 mm to 1 mm, coded L 1.0. The graded fibres were mixed with polyester resin of the POLYLITE 440 - M888 type, using hand lay-up technology. Thus, five different plates were obtained in a molding box, at 22 °C cure temperature. From these plates the specimens suitable for flexural test have been manufactured with geometry presented in Fig. 1 and physical characteristics in Table 1.

1.2 Methods

In the first step, the samples were evaluated from the morphology surfaces using contact angle method and atomic force microscope. Then, the storage and loss modules for different load frequencies were determined by DMA. In the second step, the specimens were exposed to ultra violet (UV) radiation in a radiation chamber and finally, all tests were resumed. The experimental system is presented in Fig. 2.

a) The evaluation of the surface energy of the composite lignocellulosic materials was carried

Table 1. Characteristics of the lignocellulosic composite

Type of samples	Code	Length l [mm]	Width b [mm]	Thickness h [mm]	Weight m [g]
Hemp fibers	C3	50	10.26	1.94	0.94
	L 0.04	50	10.28	4.14	2.47
	L 0.10	50	10.42	4.24	2.59
Oak particles	L 0.20	50	10.07	4.33	2.51
	L 0.40	50	10.11	4.62	2.67
	L 1.00	50	10.37	4.40	2.53



Fig. 1. The samples of lignocellulosic composite: a) hemp fibers reinforcement; b) different sizes of wood particles; c) a) The geometric shape of the specimens tested DMA (l length; d distance between supports; b width; h thickness, F applied force)

out by the θ contact angle method, which is a thermodynamic equilibrium that is a result of the superficial/ interfacial free energies appearing at the interfaces between two media. The value of the contact angle depends on: the morphology of the substrate expressed by the superficial tension between the solid - gas medium called work of adhesion W_A [mN/m], the nature of the liquid expressed by the superficial liquid - gas tension γ_{LG} [mN/m] and the nature of the liquid - substrate interactions expressed by the superficial tension between the solid - liquid medium γ_{SL} [mN/m], according to the equation Young-Dupre, Eq. (1). A liquid placed on a solid surface, in the absence of gravitational forces, will take the shape corresponding to the minimum energy of the system. This occurs when

$$W_A = \gamma_{SL} + \gamma_{LG} \cos \theta, \quad (1)$$

where θ contact angle (the angle of the tangent to the liquid-gas surface in the contact point of the liquid-solid interface).

But, the work of adhesion can be calculated with relation Eqs. (2) and (3), being composed by polar component and dispersive component .

$$W_A = \gamma_S^p + \gamma_S^d, \quad (2)$$

$$W_A = 2 \times \sqrt{\gamma_{LG}^p \times \gamma_{SG}^p} + 2 \times \sqrt{\gamma_{LG}^d \times \gamma_{SG}^d}. \quad (3)$$

For determination of both components of surface energy (dispersive denoted U_d and polar denoted U_p , in experimental results) using contact angle method, the mathematical system formed by Eqs. (1) and (3) must be calculated.

From the point of view of the values of the contact angle, it may take values between 0° and 180° . If the contact angle $\theta < 90^\circ$ (polar surface),

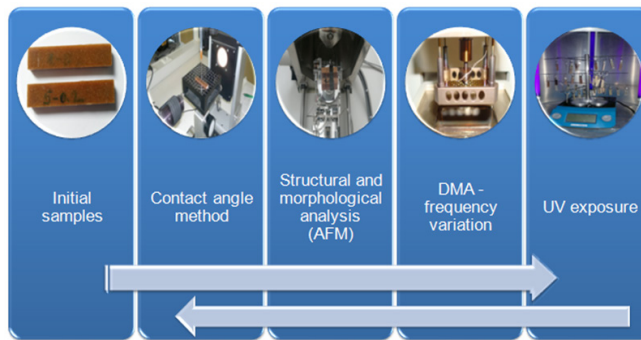


Fig. 2. The measurement of the contact angle

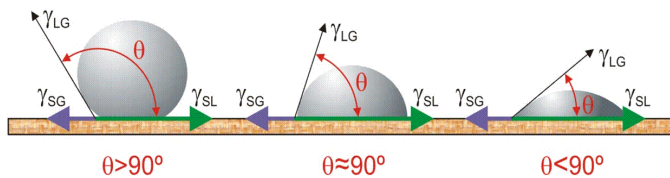


Fig. 3. The measurement of the contact angle

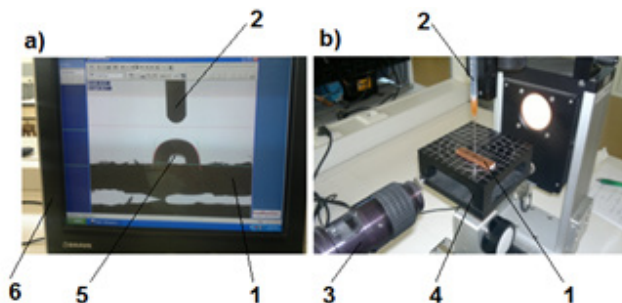


Fig. 4. The experimental determination of the contact angle: a) the projection of the droplet to measure the contact angle; b) the equipment used for contact angle measurement: 1 sample; 2 automatic dosing unit for liquids; 3 high performance video-camera; 4 worktable; 5 the drop profile measured with SCA20 software; 6 software (SCA 20) based on the Young-Laplace equation, which allows to correlate the drop shape with surface tension and with contact angle

the material is hydrophilic (it absorbs the liquid), and if $\theta > 90^\circ$ (scattered surface), the material has a hydrophobic character (it does not absorb liquid) (Fig. 3). Knowing the θ angle allows estimating the type of interaction between that surface and the liquid used in the analysis.

The contact angles were measured by the help of the System OCA-20 equipment Data Physics Instruments (Fig. 4a) by using the hanging drop method. Thus, successively a syringe with H_2O and one with NaCl were placed on top of all specimens. One drop with a volume of $15 \mu\text{L}$ of sample liquid was dropped from each syringe. By the help of a source of light situated at the back and of a camera placed in front of the droplet the contact between the droplet and the sample was recorded being followed by the measurement of the angle that the droplet forms with the surface of the specimen (Fig. 4b). Dynamic studies for the change of the contact angle offered the possibility of evaluating the absorption/ adsorption capacity of the specimens made of lignocellulosic materials based on the images recorded every second. The analysis for the measuring contact angle was done at the temperature of the room, in normal humidity conditions ($T = 22.7^\circ\text{C}$ and $RH = 65\%$).

b) For the dynamic mechanical analysis and the evaluation of the morphological changes of the surface of samples because of exposure to UV radiation and temperature, rectangular specimens from each category with the physical characteristics shown in Fig. 5 were used. Thus, the complex modulus E^* , with its two components (the storage modulus E' and the loss modulus E'') were determined under isothermal conditions ($T = 30^\circ\text{C}$), by the variation of the loading frequency ($f = 1 \text{ Hz}; 5 \text{ Hz}; 10 \text{ Hz}; 50 \text{ Hz}$).



Fig. 5. The Netzsch DMA 242 C principle of measurement

c) For the accelerated photolysis process of the specimens, the room with 18 W Philips fluorescent lamps set apart by 120° with respect to each other (Fig. 6). The specimens were exposed to UV-A radiations with a wavelength λ of 365 nm for 168 hours (7 days), checking every 24 hours the integrity and the clamping to the stand of the specimens.

d) The surface morphology of the specimens was measured by the help of the NTEGRA Probe Nanolaboratory, an atomic force microscope (AFM), at the Institute for Research and Development of the Transilvania University of Brasov, in a semi-contact mode, by using a NSG10 cantilever type (NSG10 represents cantilevers series characterized by high resolution noncontact silicon “golden”), at a constant force. Two dimensional (2D) images and histograms were taken and the images of the phase contrast of each sample were analyzed.



Fig. 6. Accelerated artificial weathering by UV radiations generated by UV fluorescent lamps

2 RESULTS

2.1 Surface Energy

An important parameter that reflects the surface changes of the composites because of the photolysis is represented by the contact angle of a drop of liquid makes with the surface of the composite. Thus, the absorption/adsorption capacity of the specimens made of lignocelluloses material has been evaluated based on the images recorded every second using as liquid the distilled water and then the NaCl solution with a concentration of 3.5 %. After the measurements, contact angles for each specimen were obtained and the values of the two components of the total surface energy were calculated U_{tot} : U_d the dispersive component and U_p the polar component, based on Eqs. (1) and (3) (see cap. 1.2). By summing up the two components, the total surface energy U_{tot} was obtained. The results are shown in Table 2.

2.2 Storage and Loss Modulus

After the exposure of the specimens to UV radiation, the specimens reinforced with particle of 0.04 mm, 0.1 mm, 0.4 mm and 1 mm have become more rigid (Table 3).

The increase in stiffness of the polyester composites because of the accelerated weathering represents a specific behavior of the polymeric composites. This trend manifests regardless of the frequency loading. One can notice a different behavior in the case of the composites reinforced with particles of 0.2 mm in size that manifests a decrease in the storage modulus after UV exposure. A similar behavior was noticed in the polypropylene matrix composites reinforced with wood particles of 0.25 mm in size. The loss modulus expresses the variation

of the viscous behavior of the composites reinforced with wood particles and polyester resin, which is influenced by the rate of the applied frequency (Table 4).

2.3 Structural and Morphological Changes

After the exposure to UV radiations, we notice a decrease in the values of the contact angle due to the structural and morphological changes, the analyzed surfaces changing from polar into slightly polar ones. This behavior is confirmed by the topographical evaluation with atomic force microscope which indicates a homogeneous surface of samples before UV exposure compare to increases of surface roughness after artificial ageing.

Table 2. The values of the contact angles and of the surface energy

Samples	Contact angle [°]				Dispersive surface energy, U_d		Polar surface energy, U_p		Total surface energy, $U_{tot} = U_d + U_p$	
	H ₂ O		NaCl(3.5 %)		[mN/m]		[mN/m]		[mN/m]	
	Initial	UV	Initial	UV	Initial	UV	Initial	UV	Initial	UV
C3	81°±0.5	61°±0.7	75°±1.0	74°±2.0	20.29	7.54	8.94	33.00	29.22	40.54
L 0.04	68°±1.0	71°±0.3	80°±2.0	65°±0.6	6.59	24.63	27.81	12.21	34.40	36.83
L 0.10	75°±0.3	75°±1.0	80°±0.6	83°±1.0	10.27	6.59	18.51	22.35	28.78	28.94
L 0.20	71°±0.6	39°±0.5	70°±0.5	63°±0.6	18.42	6.09	15.72	55.54	34.13	61.63
L 0.40	72°±1.0	48°±1.5	75°±1.0	69°±0.8	13.43	5.22	18.23	49.36	31.65	54.59
L 1.00	72°±0.8	41°±0.6	78°±0.8	49°±0.7	10.40	20.66	20.62	35.51	31.01	56.17

Table 3. The mean values of the storage modulus E' measured before and after UV

Samples	1 Hz		5 Hz		10 Hz		50 Hz		1 Hz	5 Hz	10 Hz	50 Hz
	E' [MPa]	E'_{UV} [MPa]										
C3	1152	1645	1207	1711	1226	1735	1255	1798	42.80	41.76	41.52	43.27
L 0.04	3990	4025	4105	4157	4223	4211	4284	4351	0.88	1.27	-0.28	1.56
L 0.10	3759	4456	3936	4590	4024	4645	4097	4777	18.54	16.62	15.43	16.60
L 0.20	4249	4118	4363	4248	4463	4300	4527	4430	-3.08	-2.64	-3.65	-2.14
L 0.40	3239	3419	3388	3529	3413	3572	3544	3689	5.56	4.16	4.66	4.09
L 1.00	3553	3545	3672	3739	3762	3806	3840	3982	-0.23	1.82	1.17	3.70

Table 4. The mean values of the loss modulus E'' measured before and after UV

Samples	1 Hz		5 Hz		10 Hz		50 Hz		1 Hz	5 Hz	10 Hz	50 Hz
	E'' [MPa]	E''_{UV} [MPa]										
C3	55	82	67	97	78	114	98	139	49.09	44.78	46.15	41.84
L 0.04	377	367	361	362	324	380	314	367	-2.65	0.28	17.28	16.88
L 0.10	338	363	369	365	339	389	312	373	7.40	-1.08	14.75	19.55
L 0.20	326	390	299	383	287	402	272	380	19.63	28.09	40.07	39.71
L 0.40	243	276	258	270	239	288	210	274	13.58	4.65	20.50	30.48
L 1.00	289	464	269	445	256	453	256	416	60.55	65.43	76.95	62.50

3 DISCUSSION

The surface energy increased after the exposure to UV radiations (Fig. 7), by changing the contribution of the two components: the value of the polar component U_p increased while the value of the dispersant component U_d decreased.

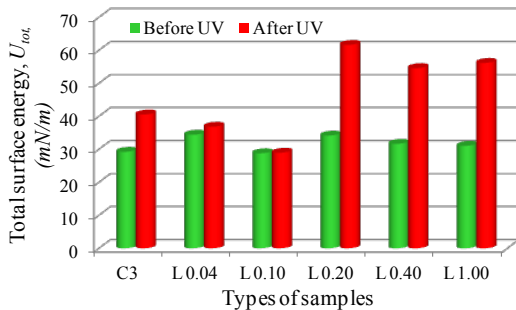


Fig. 7. The variation of the surface energy before and after the artificial weathering

From the point of view of the contact angle and implicit of the surface energy determined with distiller water H_2O (Fig. 8a), it can be noticed that the UV radiations have influenced the superficial structure of the lignocelluloses composites reinforced with bigger particles (from 0.2 mm to 1 mm). At the same time, the specimens of polyester resin and the wood particles of 0.04 mm and 0.1 mm in size were more chemically stable (Fig. 8b). Similarly, one can notice that the material becomes hydrophilic after exposure to ultraviolet radiations, thus increasing the capacity of the lignocelluloses material to absorb liquids, which leads to structural, geometrical and mechanical changes of the material. An exception of overall tendency to decreases of contact angle is recorded in case of sample L 0.04 (an slow increase with 4.41 % for water test) and L 0.10 (3.75 % increase for NaCl test). In order to stop the phenomenon and implicitly the increase of the life cycle, after the manufacturing

of the specimens a final cross-linking is recommended, which leads to stable chemical bonds between the molecules of the polymer or the use of some additives against UV radiation, as [3] and [10] noticed in the researches. Before UV exposure, the composites reinforced with wood particles have contact angles with values close to the NaCl (3.5 %) solution and distilled water H_2O (Fig. 8). After the exposure to UV radiations, we notice a decrease in the values of the contact angle due to the structural and morphological changes, the analyzed surfaces changing from polar into slightly polar ones.

As far as the contact angle of the surface is concerned when obtained by the sodium chloride solution NaCl (3.5 %) we notice its decrease after the exposure to UV, but significant differences of the contact angle measurements are noticeable when obtained with distilled water (H_2O).

With the increase of the size of the reinforcing particles, the internal friction in the structure of composites increases after the exposure to UV radiation. The most affected by UV radiation is the composites reinforced with particles of 1 mm, in which case the loss modulus E'' increases with almost 60 % to 76 % as can be seen in Table 4, sample L 1.00. Between the very small wood particles (of up to 0.04 mm), the internal frictions are more reduced after the photolysis of the specimens which can be seen in lower values of viscous modulus after UV exposure.

This can be explained due to the artificial weathering accelerates the cross-linking process of the polyester resin, the very small wood particles being included in polymer chains, the composite having a quasi-homogeneous structure. The larger the particles, the more the deformation energy is dissipated in the matrix and in the reinforcing elements, each of them overtaking a different deformation energy, depending on the viscous-elastic characteristics of the wood particles and of the polyester resin [6] and [10].

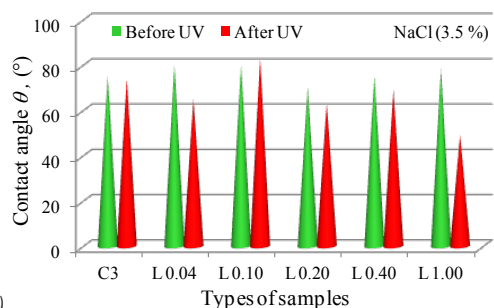
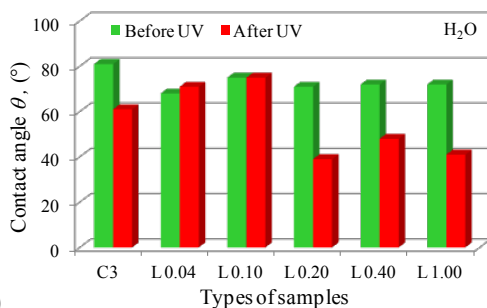


Fig. 8. The variation of the contact angle when indicating the size of the reinforcing particles of the lignocelluloses composites in the case of two liquids: a) H_2O ; and b) NaCl (3.5%), before and after exposure to UV radiations

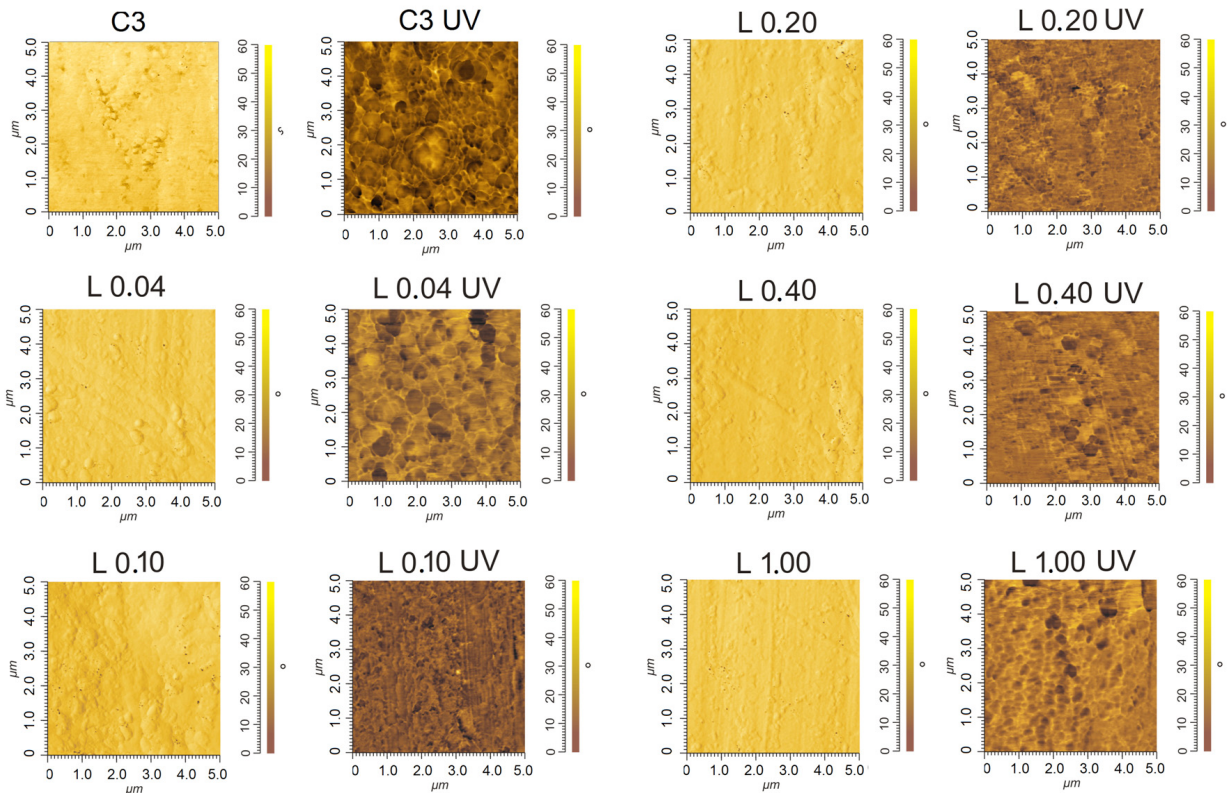


Fig. 9. The phase contrast of different studied samples obtained with AFM

Before the accelerated weathering, in the structure of the lignocelluloses composite there are phenomena specific to wood particles, matrix and interface between matrix and wood particles, which leads to variations of the internal frictions due to the physical connections (of the Van der Waals type) and chemical one situated in various stages of polymerization [14] and [15]. The UV radiation leads to a porous surface due to migration of chemical compounds (Fig. 9). This chemical and physical modification affects in time the rheological behavior of lignocelluloses composite.

From the point of view of roughness, there are two cases (Fig. 10):

- a) The first case is that of the surfaces whose roughness increased after the exposure to UV radiations, which shows an oxidative degradation of the respective surfaces. It is the case of the surface of the specimen reinforced with hemp fibres (C1), the sample reinforced with wood particles of 0.04 mm in size (L 0.04) and the solid wood.
- b) The second case is that of the surfaces whose roughness decreased after the exposure to UV. Because the decrease in roughness is of tens of nanometers, it can be appreciated that the

specimen is morphologically unstable, as is the case of the specimens reinforced with wood particles (L 0.1, L 0.2 and L 0.4).

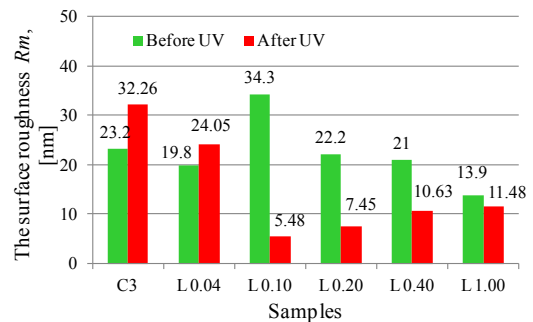


Fig. 10. The variation of surface roughness before and after UV exposure

4 CONCLUSIONS

The paper aims to assess structural and morphological changes of lignocelluloses composites surface as UV exposure, using nondestructive methods. Being studied lignocelluloses composites, the determination of structural surface changes due to exposure to UV radiation is very important because cellulose is a

hydrophilic component. The following conclusions can be drawn from the present work:

- The contact angle method provides the information about surface energy in terms of the capacity of the lignocelluloses material to absorb liquids or to act as a barrier for liquids
- The size and type of lignocelluloses reinforcement in the presence of ultraviolet radiation influence the contribution of the two components of surface energy: the value of the polar component U_p increased while the value of the dispersant component U_d decreased.
- For the composites reinforced with 0.2 mm wood particles, the mechanical performance was only slightly affected by the UV radiation in case of presented condition.
- Because the specimens were subjected to bending, extreme stresses develop in the upper and lower strata, and that explains why the influence of the UV radiation is significant due to the cross-linking process of the polymer in the structure of the composite. The hemp reinforced composite presents a similar variation in case of elastic and viscous modulus compare to wood particle reinforced composite which behavior depend by the size of particles.

5 ACKNOWLEDGEMENTS

This paper was supported by Program partnership in priority domains - PNIII under the aegis of MCI -UEFISCDI, project no. PN-III-P2-2.1-BG-2016-0017/85 SINOPTIC and MECS –ANCS project no. 18 06 01 02.

6 REFERENCES

- [1] Sahari, J., Sapuan, S.M. (2011). Natural fibre reinforced biodegradable polymer composites. *Reviews on Advanced Materials Science*, vol. 30, no. 2, p. 166-174.
- [2] Han, H. (2015). *Study of Agro-composite Hemp/Polypropylene: Treatment of Fibers, Morphological and Mechanical Characterization*, PhD thesis, Troyes University of Technology, Troyes.
- [3] Belgacem M.N., Gandini A. (2005). The surface modification of cellulose fibres for use as reinforcing elements in composite materials. *Composite Interfaces*, vol. 12, no. 1-2, p. 41-75, DOI:10.1163/1568554053542188.
- [4] Peng, Y., Liu, R., Cao, J. (2013). Effects of Antioxidants on Photodegradation of Wood Flour/Polypropylene Composites during Artificial Weathering. *BioResources*, vol. 9, no. 4, p. 5817-5830.
- [5] Stanciu, M.D., Curtu, I., Groza, M., Savin, A. (2016). The evaluation of rheological properties of composites reinforced with hemp, subjected to photo and thermal degradation. In: Chiru, A., Ispas, N. (eds.) *International Congress of Automotive and Transport Engineering, CONAT 2016*, Springer, Cham, DOI:10.1007/978-3-319-45447-4_62.
- [6] Stanciu, M.D., Bucur, V., Vâlcea, C.S., Savin, A., Sturm, R. (2018). Oak particles size effects on viscous-elastic properties of wood polyester resin composite submitted to ultraviolet radiation. *Wood Science and Technology*, vo. 52, no.2, p. 365-382, DOI:10.1007/s00226-017-0971-0.
- [7] Beg, M.D.H., Pickering, K.L. (2008). Accelerated weathering of unbleached and bleached Kraft wood fibre reinforced polypropylene composites. *Polymer Degradation and Stability*, vol. 93, no. 10, p. 1939-1946, DOI:10.1016/j.polymerdegradstab.2008.06.012.
- [8] Romanzini, D., Lavoratti, A., Ornaghi Jr, H.L., Amico, S.C., Zattera, A.J. (2013). Influence of fiber content on the mechanical and dynamic mechanical properties of glass/ramie polymer composites. *Materials & Design*, vol. 47, p. 9-15, DOI:10.1016/j.matdes.2012.12.029.
- [9] Butylina, S., Hyvärinen, M., Kärki, T. (2012). A study of surface changes of wood-polypropylene composites as the result of exterior weathering. *Polymer Degradation and Stability*, vol. 97, no. 3, p. 337-345, DOI:10.1016/j.polymerdegradstab.2011.12.014.
- [10] Azwa, Z.N., Yousif, B.F., Manalo, A.C., Karunasena, W. (2013). A review on the degradability of polymeric composites based on natural fibres. *Materials & Design*, vol. 47, p. 424-442, DOI:10.1016/j.matdes.2012.11.025.
- [11] Gozdecki, C., Wilczyn, A. (2015). Effects of wood particle size and test specimen size on mechanical and water resistance properties of injected wood-high density polyethylene composite. *Wood and Fiber Science*, vol. 47, no. 4, p. 365-374.
- [12] Benini, K.C.C.C., Voorwald, H.J.C., Cioffi, M.O.H. (2011). Mechanical properties of HIPS/sugarcane bagasse fiber composites after accelerated weathering. *Procedia Engineering*, vol. 10, p. 3246-3251, DOI:10.1016/j.proeng.2011.04.536.
- [13] Pothan, L.A., Oommen, Z., Thomas, S. (2003). Dynamic mechanical analysis of banana fiber reinforced polyester composites. *Composites Science and Technology*, vol. 63, no. 2, p. 283-293, DOI:10.1016/S0266-3538(02)00254-3.
- [14] Athijayamani, A., Ganesamoorthy, R., Loganathan, K.T., Susaiyappan, S. (2016). Modelling and analysis of the mechanical properties of agave sisalana variegata fibre/vinyl ester composites using box behnken design of response surface methodology. *Strojniški vestnik - Journal of Mechanical Engineering*, vol. 62, no. 5, p. 273-280, DOI:10.5545/sv-jme.2015.2641.
- [15] Crocchio, D., De Agostinis, M., Fini, S., Liverani, A., Marinelli, N., Nisini, E., Olmi, G. (2015). Mechanical characteristics of two environmentally friendly resins reinforced with flax fibres. *Strojniški vestnik - Journal of Mechanical Engineering*, vol. 61, no. 4, p. 227-236, DOI:10.5545/sv-jme.2014.2248.
- [16] ISO 6721-11:2012. *Plastics – Determination of Dynamic Mechanical Properties*, International Organization for Standardization, Geneva.

Complementary Methods for Evaluation of Yttria Stabilized Zirconia Coatings used as Thermal Barrier Coating

Adriana Savin^{1,*} – Mihail Liviu Craus^{1,2} – Vitaly Turchenko² – Frantisek Novy³ –
Aura C. Mocanu⁴ – Marian Soare⁴ – Janez Grum⁵ – Oleksandr Sergiyovich Doroshkevich^{2,6}

¹National Institute for R&D for Technical Physics, NDT Department, Romania

²Joint Institute for Nuclear Research, Frank Laboratory for Neutron Physics, Russia

³ University of Žilina, Faculty of Mechanical Engineering, Slovak Republic

⁴SC Nuclear NDT Research and Services SRL, Romania

⁵University of Ljubljana, Faculty of Mechanical Engineering, Slovenia

⁶ Donetsk Institute for Physics and Engineering, O. O. Galkin NAS of Ukraine, Ukraine

The paper proposes the use of a nondestructive electromagnetic (NDE) method for evaluation of zirconia coating on AISI 316L, based on an electromagnetic (EM) sensor with metamaterial lens. Metamaterials (MM), namely conical Swiss roll (CSR), operated in radiofrequency range can serve as EM flux concentrators. EM lens composing the sensors are designed on the basis of Fourier optic principles and allows the enhancement of the spatial resolution of method in order to evaluate quality of surface/adhesion coating-support. Complementary methods such as scanning electron microscopy (SEM), X ray diffraction (XRD) and neutron diffraction (ND) are employed for the studies of the samples taken into consideration.

Keywords: ZrO₂-based ceramics, yttria, scanning electron microscopy, neutron diffraction, X-ray diffraction, electromagnetic test

Highlights

- Yttria stabilized zirconia (YSZ) layers are deposited on stainless steels in order to be used as thermal barrier coatings.
- SEM, XRD and ND are used to characterize the deposited films as well as the support.
- A new sensor with metamaterial able to obtain information about films quality is used to evaluate the quality of surface/adhesion coating support.
- The presence of agglomeration of oxides and nonadherence regions were emphasized.

0 INTRODUCTION

Thermal-barrier coatings (TBCs) is used for improving efficiency and power of metallic parts employed in high temperature environment as gas-turbine engines usually used in transportation, energy, and defense sectors [1]. TBC is ceramic coating deposited on metallic surfaces, containing or not thermally grown oxide (TGO). The substrate-ceramic interface is the weakest part of TBC and can exhibit fractures under the action of thermal shock. Previous papers have been focused on behavior analysis of TGO as intermediary layer and later, on the improving of the surface of the top layer submitted to loadings during functioning. The optimization of the substrate surface topography is preferably based on a more complete characterization in order to achieve a reasonable balance between the level of induced delamination stresses, mechanical bonding as well as a minimization of the defect size.

For characterization and monitoring of TBC failure, detection of their delamination, nondestructive electromagnetic (NDE) methods are used; most of these are based on optical principles including mid-

infrared reflectance [2], luminescence spectroscopy [3] and elastic optical scattering [4]. These methods allowed detection of TBC delamination and pre-spall condition, but there are no longer investigated. Due of remarkable structural properties of zirconia (ZrO₂) based ceramics, in current technological applications (dental material, solid-oxide fuel-cell design for oxygen detection, nuclear waste confinement, medical prosthesis, etc.) ZrO₂ are preferred due to their advanced mechanical properties such as high-fracture toughness and bulk modulus, corrosion resistance, chemical inertness, low chemical conductivity and biocompatibility [5] and [6]. Lamina structures of yttria stabilized zirconia - thermal-barrier coatings (YSZ-TBC) layers deposited on stainless steels are typically porous and the pore size and character depends on the process parameters. A decreasing of global coating porosities is preferred; especially those opened at the surface, in order to reduce to minimum the permeability of coating to oxidation. ZrO₂ doped with rare earths oxides is considered a good TBC material [7] due of its low thermal conductivity (~2.0 m⁻¹K⁻¹ at 1100 °C), refractory, chemical inertness, and compatible thermal expansion coefficient [6]

and [8] with metallic support. Zirconia stabilized in tetragonal phase, namely tetragonal zirconia polycrystal (TZP) have CeO_2 and Y_2O_3 [9] and [10] as stabilizers. The dimensions of crystallites are in the range of hundreds of nanometers, conferring a high resistance to breaking, so that YSZ shows high resistance to thermal shocks and fatigue up to 1150 °C temperature [11]. It is known that three low-pressure polymorphic forms of zirconia [6] and [12] can be found: monoclinic state (stable for temperatures below 1170 °C), $P2_1/c$; tetragonal phase, $P4_2/nmc$ (stable for temperature between 1170 °C and 2370 °C) and the cubic, $Fm-3m$ phase (for temperature above 2370 °C) [13]. Despite the success of zirconia in many new applications, it has become apparent that certain zirconia compositions can also have one weakness - their tendency to low temperature degradation in the presence of moisture. Under external stress, as grinding or impact, transition from the tetragonal (t) to monoclinic (m) phase can appear at normal temperatures, being followed by an increase of volume of 3 % to 12 %, causing compressive stress of YSZ coating [14] and [15].

New nanocomposites, in which nanometer - sized second phase particles are dispersed within a ceramic matrix and/or at grain boundaries, have shown significant improvements in strength and creep resistance, even at high temperatures, and assure an exciting future in different technological fields. This paper proposes to present an electromagnetic (EM) method for evaluation of ZrO_2 coating (to differentiate the areas with good/inferior coating quality) on stainless steels using an EM sensor with metamaterial (MM) lens. The novelty consists in the type of deposition of zirconia layers, without intermediate TGO substrate, the thin thickness of the deposition and the way of nondestructive testing. Alternative methods of characterization are involved as scanning electron microscopy (SEM), X-ray diffraction and metallography [16].

1 THEORETICAL PRINCIPLES OF ELECTROMAGNETIC SENSORS WITH MM LENS

1.1 Electromagnetic Sensor

The EM NDE is a well-known method for the quality evaluation of conductive pieces and structures with the aim of discontinuities detection cracks, inclusions, voids, etc. It is based on the induction of eddy current in the object to be evaluated, of which circulation is modified when there are regions with electrical

conductivity and/or magnetic permeability different from that of the medium.

The metamaterials, electromagnetic structures with distinguished properties have started to be studied especially in the last few years (tuned mass absorbers or use for structural health monitoring (SHM)). MMs [17] can provide an engineered response to EM radiation that is not available from the class of naturally occurring materials. The size of the structure is typically smaller than the free space wavelength of incoming EM waves. Nowadays, multitudes of MM structural elements type are known, conferring special EM properties. Depending on the frequency of the incident EM field, the type and geometrical shape MM may have a high relative magnetic permeability either positive or negative [18] and [19] and allow the EM waves amplification [20]. These properties strongly depend on the geometry of metamaterials more than on its composition [20] and [21].

Due to their wide application in perfect lens [19], MM must be characterized as an effective homogeneous slab with ϵ_{eff} and μ_{eff} , that can be calculated from the scattering parameters (S -parameters) data. The matrices containing the S -parameters express the changes of EM energy propagating through a multiport transmission line if EM wave meets the impedance differing from the line's characteristic impedance. For two-port line, S -parameter express the response to reflected (S_{11} , S_{22}) and transmitted (S_{12} , S_{21}) EM signal at each port, [22]. S parameters have been measured using Agilent type 4395A coupled with Agilent S - parameter test kit 87511A. Assuming the continuous material is characterized by n refractive index and Z impedance relatively simple analytic expression can be found relating n and Z of a slab to the S parameters [23]:

$$n = \frac{1}{kd} \cos^{-1} \left[\frac{1}{2S_{21}} (1 - S_{11}^2 + S_{21}^2) \right], \quad (1)$$

$$Z = \sqrt{\frac{(1 + S_{11})^2 - S_{21}^2}{(1 - S_{11})^2 - S_{21}^2}}, \quad (2)$$

where d represents the dimension of unit cell of MM.

In the case of conical Swiss roll CSR, dimension of d is 20 mm (as the diameter of the large basis of the CSR) and k represents the wavenumber of the incident electromagnetic wave in free space, n and Z are related to dielectric permittivity and magnetic permeability by the relations [23] and [24]:

$$\epsilon = \frac{n}{Z}, \quad (3)$$

$$\mu = nZ, \quad (4)$$

where n and Z have complex values.

The EM sensor is an absolute send-receiver type [18] and [22], and has the principle scheme given in Fig. 1a and its construction in Fig. 1b. EM sensors with MM lens is made using CSR [22]. The operation frequencies depends both by the constitutive parameters of MM lens as well as by the polarization

of the incident EM field (transversal electric TE_z or transversal magnetic TM_z), in this case TM_z polarized at normal incidence. The emission part of the sensor is made from a single turn rectangular coil with $20 \text{ mm} \times 60 \text{ mm}$ dimensions, placed at 25 mm distance from the lens. The reception coil sensors has one turn with 1 mm average diameter placed in the focal image point, converting the localized energy into an electromotive force (EMF).

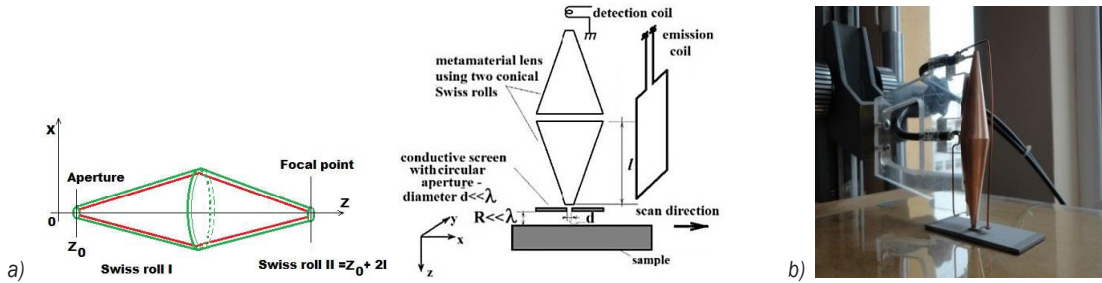


Fig. 1. Sensor with MM lens: a) principle scheme; b) physical realization

Using Fourier optic basics principles, the field in focal plane of the lens made by two CSR is:

$$H(x, y, z_0 + 2l) = \frac{H_0}{\pi^2} e^{j\left(\frac{k_b+k_a}{2}x + \frac{k_b+k_a}{2}y\right)} \frac{\sin\left(\frac{k_b-k_a}{2}x\right)}{x} \frac{\sin\left(\frac{k_b-k_a}{2}y\right)}{y}, \quad (5)$$

when $z_0 \ll \lambda$ (λ is the wave length of the incident field), H_0 being the amplitude of incident magnetic field.

In order to enhance spatial resolution, to ensure paraxial incident beam, in front of the sensor is placed a conductive screen having a circular aperture made from perfect electric conductive (PEC) material with very small diameter. The diameter of focal spot of MM lens is [25]:

$$D = \frac{4\pi}{(k_b - k_a)}, \quad (6)$$

and it is equal with CSR small basis diameter i.e. 3.2 mm , with k_a, k_b defined in [22]. When the lens is displaced along the scanning axis x , Fig. 1a, $k_a=0$ and inserting in Eq. (6), k_b can be obtained and thus the field from Eq. (5). The functioning of the sensor is presented in [18]. The scattered field must be also focused such that it can be detected by the reception part of the sensor placed in image focal point. EM sensor with MM lens has been realized with two CSRs, tuned at 105 MHz frequency [18], having

a large basis face to face. The MM lens assure the possibility to apply of electromagnetic metamaterial in eNDE.

1.2 Basic Principle of Focused Image

In order to obtain the good results of the NDT methods, it is necessary to obtain focused images on different planes [26]. Let us consider that the emission part of the sensor generates spherical waves in the material, having k waves number and R the position vector of the scatter. The signal received from a scatter which, assuming an ideal spherical wave, will be

$$\theta_H = ck \sin c(kR), \quad (7)$$

where θ_H is the phase of the sensor response vs. the incident wave, c is a complex constant and $R = |\vec{R}|$. The sensor scan the surface at the constant height $z_0 \ll \lambda$ and the scatter being located at depth z_1 below the surface, therefore the distance between sensor and scatter is $z_0 + z_1$. Let $U(x, y, z)$ be the signal delivered by the sensor and $\bar{U}(x, y, z_0)$ its two dimensional (2D) Fourier transform, where u and v are spatial frequencies associated to x and y directions. We denote by $\hat{\theta}(x, y, z)$ the 2D Fourier transform of the point spread function. The filtered and focused signal is given by the 2D Fourier transform of the convolution product of $\bar{U}(x, y, z_0)$ by the kernel $\hat{\theta}(x, y, z)$.

$$A(x, y, z) = \frac{1}{(2\pi)^2} \int_{-\infty}^{\infty} \int_{-\infty}^{\infty} \tilde{U}(u, v, z_0) \tilde{\theta}(u, v, z) \exp j(ux + vy) dudv, \quad (8)$$

The image processed in this way can be obtained with:

$$I(x, y) = |A(x, y, z)|^2. \quad (9)$$

2 STUDIED SAMPLES

The ZrO_2 - Y_2O_3 ceramics has been analyzed in the past years, the most publications presenting the special mechanical properties of the Y_2O_3 content structure.

By doping with Ytria, a cation substitutive, supplementary oxygen vacancies are added to the molecular structure, increasing the ionic electrical conductivity. When Ytria is alloyed with zirconia in concentration from 3 % to 20 % (molar percent), the crystalline structure of material in normal conditions is entirely stabilized [27], so that at variation of temperature, microcracking apparition can be avoided. Monolithic coating consisting of various thickness zirconia doped with 3 % to 20 % Y_2O_3 deposited on AISI 316L (composition in wt. % as EN 1.4404, Table 1) have been taken into study.

Table 1. Chemical composition of substrate material

element	C	Si	Mn	P	S
wt. %	0.018	0.458	1.294	0.032	0.003
element	Cr	Ni	Mo	N	
wt. %	16.815	10.086	2.004	0.032	

The AISI 316L steel may be susceptible to intergranular corrosion in certain corrosive media after it is welded or otherwise heated at temperatures between 430 °C and 860 °C [28] and [29]. It has electrical conductivity $1.3513 \times 10^6 \text{ S} \cdot \text{m}^{-1}$ and thermal expansion coefficient $17.2 \times 10^{-6} \text{ K}^{-1}$ at 473 K. TBC coating were deposited onto AISI 316L samples (20 mm × 80 mm and 2 mm height) using plasma torch F 400 with commercial atmospheric equipment APS 100 produced by Plasma-Technik AG.

Monolithic coatings of various thickness consisting of zirconia doped with 20 % Y_2O_3 and sandwich zirconia doped with 20 % Y_2O_3 and Y_2O_3 coatings were deposited on AISI 316L [30]. The coating material is produced by Metco as powder Metco™ 202NS and Metco 6035A-1 used for plasma spraying, having excellent resistance to oxidation and corrosion at temperature up to 1000 °C and can

create good TBC. Pure yttrium oxide is a highly stable compound with a high melting point, is very inert chemically, and exhibits excellent electrical insulation (volume resistivity and dielectric breakdown strength). The quality of surface of ceramic coating depend on gas flow, power levels, powder particle size distribution, etc. During the deposition, also samples without good adherence at support were obtained, being analyzed as well.

2.1 Microscopy Analyses

For TBC the most important parameters are the thickness, thermal conductivity and density of coatings. In order to minimize the residual stresses inside the sandwich coating-alloy support during the heating/cooling, the coating ZrO_2 - Y_2O_3 shall be characterized: It is difficult to achieve the electronic conductivity balance at 1200 °C in the conditions of low diffusion of cations in YSZ [31].

In Fig. 2a we are showing the cross sectional image of the sample deposited with ZrO_2 with 20 % Y_2O_3 with 0.2 mm thin monolithic coating, using a Zeiss microscope in polarized light with Axio Imager A1m and in Fig. 2b the cross section of sample deposited with ZrO_2 with 20 % Y_2O_3 with 0.25 mm thin monolithic coating using Zeiss microscope Z1m with Axio-Vision 4.8.

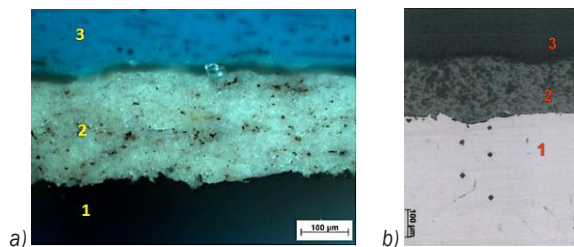


Fig. 2. Metallography: a) of ZrO_2 with addition of 20 % Y_2O_3 ceramic coating with 0.2 mm thickness; b) of ZrO_2 with 20 % Y_2O_3 ceramic coating with 0.25 mm thickness (1 substrate AISI 316L; 2 Zirconia doped with Ytria; 3a Bakelite; 3b air)

The Vickers micro-indentation tests were performing using Shimadzu M device to determine the hardness of zirconia coating to support, the measured value being of 470 HV 0.05. Indentations were effectuated on longitudinal and cross section. Information about interface between support and zirconia coating are obtained by SEM and EDX.

Usually, information about porosity of coating is obtained by surface microscopy and soft gray scale threshold setting. This technique is subjective, due to the setting of gray level and light intensity, reflection

of surface, samples preparation etc. The accuracy of gray scale threshold approach is investigated using image processing in Matlab described in [31].

Taking into account that the structures of YSZ TBC layers deposited on stainless steels are typically porous [30], to obtain relevant information about the influence of yttria concentration over the adherence at support, secondary electrons (SE) images, as well as backscattered electrons (BSE) images have been taken, Figs. 3a and c. In Figs. 3b and d are presented the histograms of voids data.

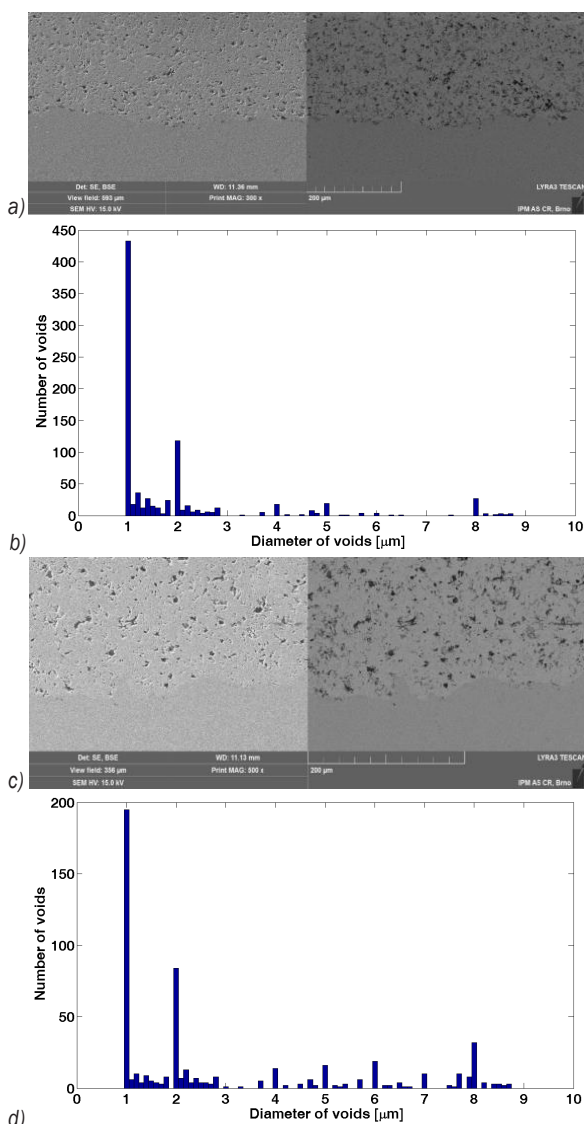


Fig. 3. SEM images (a and c) and voids counting (b and d): a) and b) for specimen with 0.2 mm thin monolithic coating ZrO_2 with addition of 20 % Y_2O_3 ; c) and d) for specimen with sandwich coating 0.25 mm ZrO_2 with addition of 20 % Y_2O_3 and 0.005 mm Y_2O_3

It can be observed that with the doping with yttria, the voids are larger but their number decreases.

Topographical characterization of the specimen is realized with a TESCAN electron microscope (TESCAN LYRA3 GM) operating at an acceleration voltage of 15 kV. The porosity of the tested surface can be evaluated from the SEM images within 0.5 % accuracy.

2.2 X-Ray Diffraction (XRD) and Neutron Diffraction (ND)

XRD experiments performed at room temperature on a Philips diffractometer, at JINR Dubna, Russia, allow determination of the phase composition and microstructural parameters by using Fullprof software. The space group and lattice constants were obtained with Ceckcell and proofed by Fullprof software. The comparisons between the diffractogram of the sample formed from a layer of zirconia doped with yttria deposited on a support of AISI316L with the diffractogram of AISI 316L and, respectively, with the diffractogram of zirconia doped with yttria allowed to identify austenite maxima (γ) (Fig. 4) and doped zirconia (t) maxima (Fig. 5).

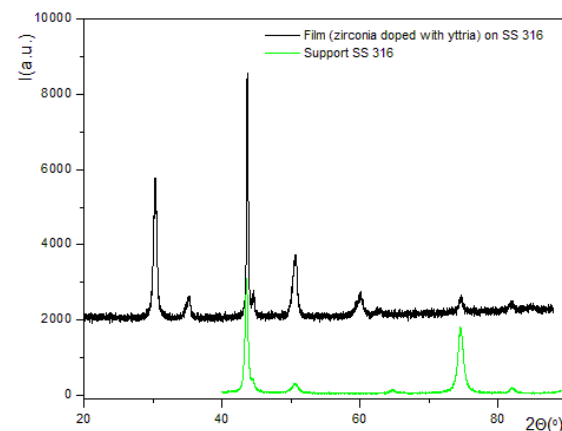


Fig. 4. The Xray diffractograms of support + the layer of zirconia with yttria and of the support

Some ND data were collected by using the high resolution Fourier diffractometer (HRFD) time-of-flight diffractometer from reactor IBR 2 – JINR Dubna, Russia, at room temperature (Fig. 6) corresponding bulk samples of zirconia doped with yttria on bulk samples (ND diffractograms were calculated also by using FullProf and PowderCell software). We have attempted to determine the conditions in which zirconia doped with yttrium can be identified in the diffractogram of a sample formed by a yttrium-doped zirconia layer and a stainless steel

support, using the data obtained on zirconia doped with yttria (4 % and 8 %) bulk sample.

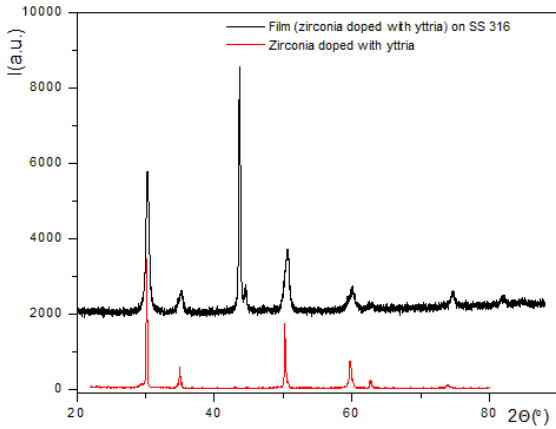


Fig. 5. The X ray diffractograms of support + the layer of zirconia with yttria and of the zirconia with yttria

Transformation of TOF values in 2Θ values was obtained using the relation:

$$2\Theta = \left[\frac{360}{\pi} \right] a \sin \left[\frac{Dtt1 \times 0.77026}{TOF - ZERO} \right]. \quad (10)$$

The constants ZERO, Dtt1 and Dtt2 can be determined with a standard (Dtt2=0 in this case). The neutrograms were obtained using $\lambda=1.5406\text{\AA}$. The test performed on zirconia doped with yttria (4 % to 8 %) bulk samples by neutron diffraction at IBR-2 Dubna, Russia indicated the presence of two phases (Fig. 6).

The calculated neutronogram for a sandwich of two layer of zirconia doped with 20 % yttria (0.25 mm thickness) and a layer of yttria (0.005 mm thickness) is presented in Fig. 7.

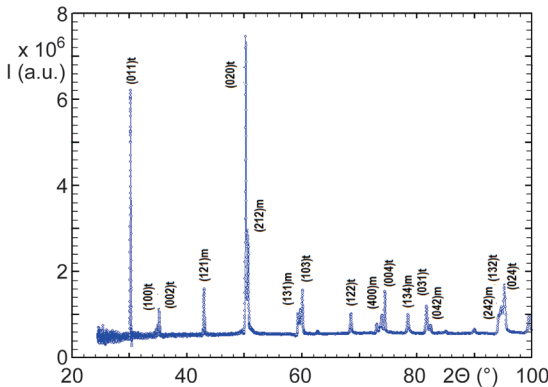


Fig. 6. The neutronogram of $ZrO_2+4\%Y_2O_3$ bulk sample; the ND data were acquired by using HFRD diffractometer, IBR-2, Dubna, Russia

The both layers are practically transparent for the neutron beam and the volumes of the layers are supposed to be the same. The diffracted intensities corresponding to the layers depend on its relative volumes.

The calculated neutronogram of a mixture between stainless steel, zirconia and yttria, in equal concentrations, is presented in Fig. 7.

We have used a neutron beam with a constant wavelength ($\lambda=1.5406\text{\AA}$), the same with the wavelength used to obtain the X-ray diffractogram of layer of zirconia deposited on AISI 316 support (Fig. 8).

In the first case (XRD) we have a real thin layer of zirconia (about 200 μ), in the second case (ND) the neutron beam sees equal volumes of the three components of the “phase mixture: steel 316, zirconia and yttria” (Fig. 7).

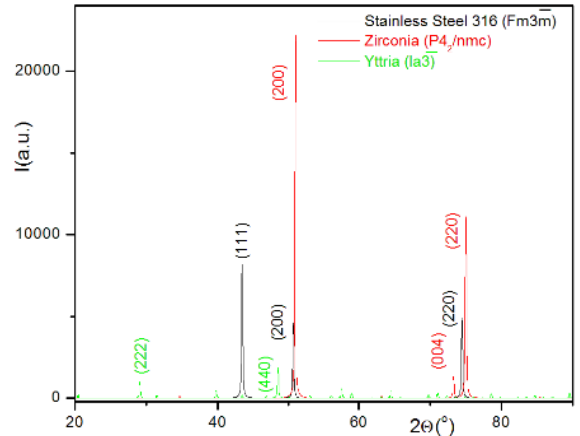


Fig. 7. The calculated diffractogram of the zirconia doped with yttria layer + yttria intermediate layer on AISI 316 support (ND)

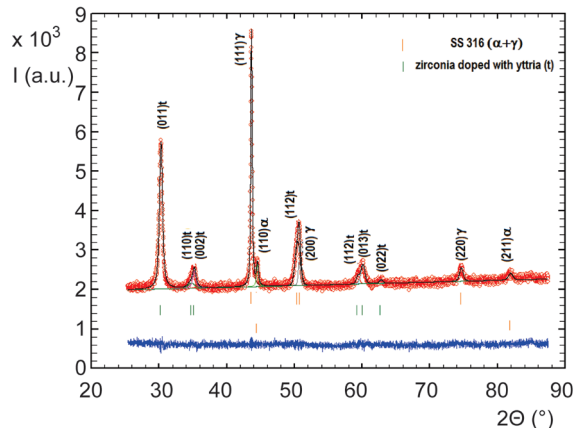


Fig. 8. The observed diffractogram of the zirconia doped with yttria layer on AISI 316L support (XRD) - in blue (curve below) - is the difference between calculated and observed X ray diffractogram

In fact, the concentration ratio of the three phases is 1000: 125: 2.5. The intensity of maxima corresponding to yttria cannot be observed in this case. We will investigate the yttria+zirconia layers deposited on stainless steel 316 support by neutron reflectometry or by X-ray diffraction.

The difference between the structure of bulk doped with yttrium zirconia and of the deposited layer of yttrium doped zirconia on 316 support will be discussed elsewhere.

3 EXPERIMENTAL SETUP OF ELECTROMAGNETIC TESTING

ZrO₂-Y₂O₃ used as top-coating (is nonconductive and nonmagnetic) behaves like an air gap between conductive support and EM sensor, creating a lift-off for the EM sensor. The challenge for the development of new types of EM transducers consists in the obtaining of good detection sensitivity for a minimum 3/1 signal to noise ratio as well as a good spatial resolution.

As shown in [22], the sensor with a lens realized with CSR, functioning in the range of frequencies such that μ_{eff} is maximum. The detection principle is similar with the one of near-field electromagnetic scanning microscopy (NFSEM) [18]. NFSEM imaging is a sampling technique, i.e., the specimen (in this case plate with thickness of coating) is probed point by point by raster scanning with the sensor over the specimen surface and recording for energy image pixel a corresponding electromagnetic signature. Scattered EM field from other regions is eliminated by using MM lens with CSR with a conductive screen with circular aperture (made from perfect electric conductor material, copper foil adhesiveless laminated with 12 μm thickness polyimide foil) according to Fig. 9a. The functioning of entire system detection can be described using Fourier optics [32] and [33]. The skin depth is limited by standard penetration $\delta = \sqrt{2/\omega\mu_0\sigma}$ with $\omega = 2\pi f$, $\mu_0 = 4\pi \times 10^{-7} \text{Hm}^{-1}$, being vacuum magnetic permeability and σ is the electric conductivity of material. The reception coil functions as a detection antenna, converting localized energy into electromotive force.

The eNDE of a material consists in the applying an EM field to the object examined and evaluating the interaction between the field and the eventual material flaws [34] and [35]. To increase the reliability and assure quality, an automatic scanning system is used, XY displacement system type Newmark together with a high frequency data acquisition [18]. The EM sensor with MM lens, presented above is connected to

a Network/Spectrum/Impedance Analyzer type 4395A Agilent USA.

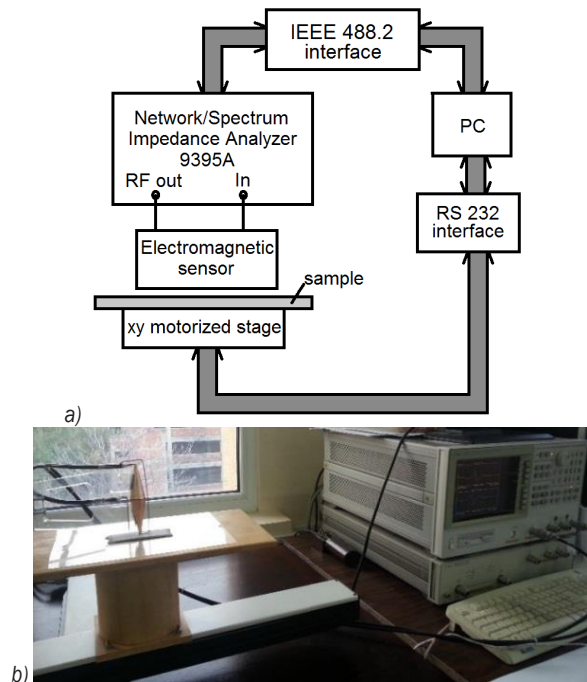


Fig. 9. Experimental setup: a) basic scheme; b) equipment

During the measurements, the sensor was fixed and the samples is mounted on a XY displacement system. That assures the displacement in plan with $\pm 10 \mu\text{m}$ precision and assures the scanning $5 \text{ mm} \times 5 \text{ mm}$ surface of sample with 0.1 mm steps in both directions. A PC allows the command of manipulation and measurement instruments, the data being acquired and stored automatically.

4 RESULTS OF EM TESTING

It is possible to appear many cracks due to the relaxation of residual stresses after deposition. The microstructure obtained by plasma jet can present lamellar or flattened splats with micro cracks through the splats or inter-splats. These splats lie parallel to the surface of the coating due to impact of the high-speed molten particles on the substrate. The surface and bonding quality of support-layers are examined [36]. The sensor with MM lens has allowed the identification and estimation of the zones where the nanoparticles have created shear distortions [37], possible to degenerate in the damage of the coatings. The samples were placed on the displacing system, with emission coil perpendicular on the surface and on scanning direction [18]. Ceramic zirconia

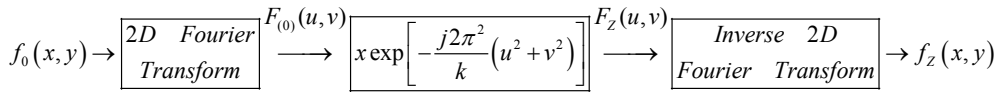


Fig. 10. The image modification by an aperture due to Fresnel diffraction

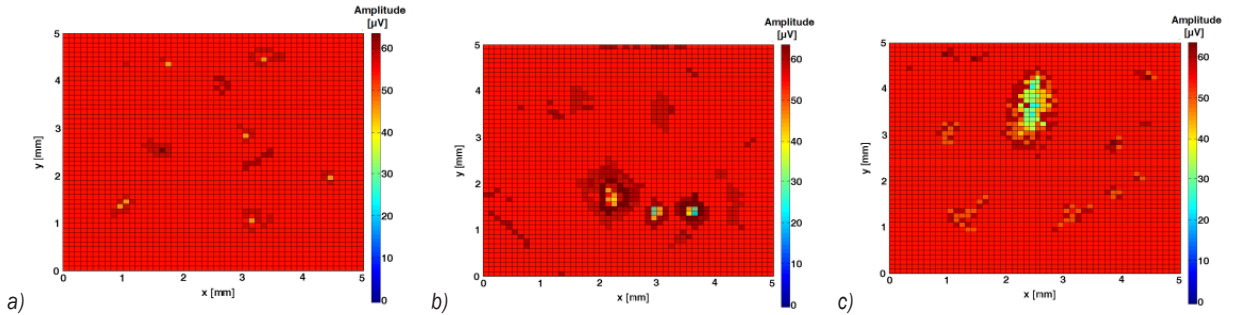


Fig. 11. The amplitude of the voltage induced in the reception coil of the electromagnetic transducer:

- a) 0.2 mm thin monolithic coating ZrO_2 with addition of 20 % Y_2O_3 ; b) sandwich coating 0.25 mm ZrO_2 with addition of 20 % Y_2O_3 and 0.005 mm Y_2O_3 ; c) specimen with nonadherence from 0.25 mm thin monolithic coating ZrO_2 with 20 % Y_2O_3 addition

top coating is nonconductive and nonmagnetic, this creates a probe lift-off effect. The specimens with 0.2 mm thickness of zirconia coating with and without yttria were fixed on a Newmark X-Y displacement system, and the image delivered by the assembly sensor-equipment is amplified. In order to improve the spatial resolution, in front of the sensor with MM lens has been placed the circularly aperture 0.1 mm diameter. This is due to the diffraction on the aperture of the electromagnetic field generated by scattering on the specimen. That assure for the structure of surface clearly visible. Considering an object placed in the plane $z=0$ and described by the function $f_0(x, y)$, at passing through an aperture, in the case of Fresnel diffraction (the aperture is closely to the object), the image obtained at the distance z from the object will be $f_z(x, y)$ and can be calculated using the algorithm presented in Fig. 10, according to the principle of Fourier optics.

To ensure that $f_z(x, y)$ might represent exactly the figure of Fresnel diffraction through the a radius aperture, between the Fourier variables and the spatial ones must be:

$$du = \frac{2a}{Ndx_0}, \quad dv = \frac{2a}{Mdy_0}, \quad (11)$$

where N and M represent the maximum number of measurement points along x and y direction and dx_0 and dy_0 are the scanning step along x and respective y directions. Inverting the operation from Fig. 10, the object $f_0(x, y)$ can be determined knowing the diffraction figure $f_z(x, y)$. The measurements effectuated with the aperture make that the signals

recorded shall represents $f_z(x, y)$. The shape of the object that scatters the electromagnetic field created by the emission coil can be determined.

Figs. 11a and b show the amplitude of the voltage induced in the reception coil of the electromagnetic transducer at the scanning of the two specimens presented above.

Fig. 11c present the scanning of a specimen with no adherence from 0.25 mm thin monolithic coating ZrO_2 with addition of 20 % Y_2O_3 . It can be observed that the values of emf induced in the reception coils are affected by the material microstructure and by the presence of inhomogeneities on/in the surface of support.

The image corresponding to 0.2 mm thin monolithic ZrO_2 with addition of 20 % Y_2O_3 do not present nonadherence regions. The amplitude of voltage induced in the reception coil has relatively constant value, excepting the regions where variations appear most probable due to agglomeration of oxides.

Sandwich coatings 0.25 mm ZrO_2 with addition of 20 % Y_2O_3 and 0.005 mm Y_2O_3 show that at doping with yttria, the voids are more extended but their number decreases, fact confirmed also by the SEM images.

5 CONCLUSIONS

TBC potential depends not only by the intrinsic properties of TBC's material but of the coating microstructure that is determined by the deposition process. Nanocomposites with nanometer - sized second phase particles dispersed in ceramic matrix

and/or at grain boundaries have shown an ability to withstand thermal cycling at temperatures significantly higher than simple layer YSZ-coatings. They also have significant better strength and creep resistance than other coatings by decreasing the number of voids. Hence the evaluation of the surface structure and possible delamination at the interface of deposited layers for this type of zirconia coating on stainless steel is important.

Further tests on a larger number of specimens with different coating aspects of the surface, influence of surface roughness on stress intensity factor, number of layers are needed to establish the accuracy of the results and the correlation between the located very small defect in size and the results of MM sensor response. Also, the results can be further continued by complementary investigation as ND, X ray diffraction or other methods that can emphasize indications about phase composition and structure parameters.

6 ACKNOWLEDGEMENTS

This paper is partially supported by Romanian Ministry of Research and Innovation under Nucleus Program PN 2018- 3MAP and Bilateral Cooperation with JINR Dubna under protocol no. 4414-4-2015/2018.

7 REFERENCES

- [1] Alvin, M.A., Klotz, K., McMordie, B., Zhu, D., Gleeson, B., Warnes, B. (2014). Extreme temperature coatings for future gas turbine engines. *Journal of Engineering for Gas Turbines and Power*, vol. 136, no. 11, p. 112102, DOI:10.1115/1.4027186.
- [2] Eldridge, J.I., Spuckler, C.M., Martin, R.E. (2006). Monitoring delamination progression in thermal barrier coatings by mid-infrared reflectance imaging. *International Journal of Applied Ceramic Technology*, vol. 3, no. 2, p. 94-104, DOI:10.1111/j.1744-7402.2006.02067.x.
- [3] Tolpygo, V.K., Clarke, D.R., Murphy, K.S. (2004). Evaluation of interface degradation during cyclic oxidation of EB-PVD thermal barrier coatings and correlation with TGO luminescence. *Surface and Coatings Technology*, vol. 188-189, p. 62-70, DOI:10.1016/j.surfcoat.200408.001.
- [4] Ellingson, W.A., Visher, R.J., Lipanovich, R.S., Deemer, C.M. (2006). Optical NDT techniques for ceramic thermal barrier coatings: NDT of ceramics: an introduction to the technical focus issue. *Materials Evaluation*, vol. 64, no. 1, p. 45-51.
- [5] Pieralli, S., Kohal, R.J., Hernandez, E.L., Doerken, S., Spies, B.C. (2017). Osseointegration of zirconia dental implants in animal investigations: A systematic review and meta-analysis. *Dental Materials*, vol. 34, no. 2, p. 171-182, DOI:10.1016/j.dental.2017.10.008.
- [6] Ceramtec (2017). from: www.ceramtec.com, accessed on 2018-10-27.
- [7] Renusch, D., Schütze, M. (2007). Measuring and modeling the TBC damage kinetics by using acoustic emission analysis. *Surface and Coatings Technology*, vol. 202, no. 4-7, p. 740-744, DOI:10.1016/j.surfcoat.2007.07.109.
- [8] Ryschkewitch, E., Richerson, D.W. (1985). *Oxide ceramics: Physical Chemistry and Technology*, Haskell General Ceramics, New York.
- [9] Zhu, W.Z. (1998). Effect of cubic phase on the kinetics of the isothermal tetragonal to monoclinic transformation in ZrO₂ (3mol% Y₂O₃) ceramics. *Ceramics International*, vol. 24, no. 1, p. 35-43, DOI:10.1016/S0272-8842(96)00074-0.
- [10] Li, P., Chen, I.W., Penner-Hahn, J.E. (1994). Effect of dopants on zirconia stabilization – an X-ray absorption study: I, trivalent dopants. *Journal of the American Ceramic Society*, vol. 77, no. 1, p. 118-128, DOI:10.1111/j.1151-2916.1994.tb06964.x.
- [11] Ren, X., Pan, W. (2014). Mechanical properties of high-temperature-degraded yttria-stabilized zirconia. *Acta Materialia*, vol. 69, p. 397-406, DOI:10.1016/j.actamat.2014.01.017.
- [12] Èvarestov, R.A. (2015). *Theoretical Modeling of Inorganic Nanostructures: Symmetry and ab-initio Calculations of Nanolayers, Nanotubes and Nanowires*. Springer, Berlin, DOI:10.1007/978-3-662-44581-5.
- [13] Faktorova, D., Novy, F., Fintova, S., Savin, A., Steigmann, R., Iftimie, N., Turchenko, V., Craus, M.L. (2016). Evaluation of zirconia coatings deposited on stainless steel substrate. *Electromagnetic Nondestructive Evaluation (XIX)*, vol. 41, p. 254-262, DOI:10.3233/978-1-61499-639-2-254.
- [14] Savin, A., Craus, M.L., Turchenko, V., Bruma, A., Dubos, P.A., Malo, S., Konstantinova, T.E., Burkhovetsky, V.V. (2015). Monitoring techniques of cerium stabilized zirconia for medical prosthesis. *Applied Sciences*, vol. 5, no. 4, p. 1665-1682, DOI:10.3390/app5041665.
- [15] Limarga, A.M., Shian, S., Baram, M., Clarke, D.R. (2012). Effect of high-temperature aging on the thermal conductivity of nanocrystalline tetragonal yttria-stabilized zirconia. *Acta Materialia*, vol. 60, no 15, p. 5417-5424, DOI:10.1016/j.actamat.2012.06.054.
- [16] Gupta, G.K., Chattopadhyaya, S. (2017). Critical failure analysis of superheater tubes of coal-based boiler. *Strojniški vestnik - Journal of Mechanical Engineering*, vol. 63, no. 5, p. 287-299, DOI:10.5545/sv-jme.2016.4188.
- [17] Wiltshire, M.C.K. (2007). Radio frequency (RF) metamaterials, *Physica Status Solidi (b)*, vol. 244, no. 4, p. 1227-1236, DOI:10.1002/pssb.200674511.
- [18] Savin, A., Steigmann, R., Bruma, A., Šturm, R. (2015). An electromagnetic sensor with a metamaterial lens for nondestructive evaluation of composite materials. *Sensors*, vol. 15, no. 7, p. 15903-15920, DOI:10.3390/s150715903.
- [19] Pendry, J.B., Holden, A.J., Robbins, D.J., Stewart, W.J. (1999). Magnetism from conductors and enhanced nonlinear phenomena. *IEEE Transactions on Microwave Theory and Techniques*, vol. 47, no. 11, p. 2075-2084, DOI:10.1109/22.798002.
- [20] Van Bladel, J.G. (2007). *Electromagnetic Fields*, 2nd ed. IEEE Press: Piscataway, DOI:10.1002/047012458X.

- [21] Liu, X., Hu, G. (2016). Elastic metamaterials making use of chirality: a review. *Strojniški vestnik - Journal of Mechanical Engineering*, vol. 62, no. 7-8, p. 403-418, DOI:10.5545/sv-jme.2016.3799.
- [22] Grimberg, R., Savin, A., Steigmann, R., Serghiac, B., Bruma, A. (2011). Electromagnetic non-destructive evaluation using metamaterials. *Insight-Non-Destructive Testing and Condition Monitoring*, vol. 53, no. 3, p. 132-137, DOI:10.1784/insi.2011.53.3.132.
- [23] Grimberg, R., Tian, G.Y. (2012). High-frequency electromagnetic non-destructive evaluation for high spatial resolution, using metamaterials. *Proceedings of the Royal Society A: Mathematical, Physical and Engineering Sciences*, vol. 468, no. 2146, p. 3080-3099, DOI:10.1098/rspa.2011.0666.
- [24] Smith, D.R., Vier, D.C., Koschny, Th., Soukoulis, C.M. (2005). Electromagnetic parameter retrieval from inhomogeneous metamaterials. *Physical Review E*, vol. 71, no. 3, p. 036617, DOI:10.1103/PhysRevE.71.036617.
- [25] Born, M., Wolf, E. (1959). *Principles of Optics: Electromagnetic Theory of Propagation, Interference and Diffraction of Light*. Pergamon Press, Oxford.
- [26] Grimberg, R., Savin, A., Steigmann, R., Bruma, A. (2006). Eddy current examination of carbon fibres in carbon-epoxy composites and Kevlar. *International Journal of Materials and Product Technology*, vol. 27, no. 3-4, p. 221-228, DOI:10.1504/IJMPT.2006.011272.
- [27] Pascual, C., Durán, P. (1983). Subsolidus phase equilibria and ordering in the system ZrO_2 - Y_2O_3 . *Journal of the American Ceramic Society*, vol. 66, no. 1, p. 23-27, DOI:10.1111/j.1151-2916.1983.tb09961.x.
- [28] Chowdhury, S.G., Das, S., Ravikumar, B., De, P.K. (2006). Twinning-induced sluggish evolution of texture during recrystallization in AISI 316L stainless steel after cold rolling. *Metallurgical and Materials Transactions A*, vol. 37, no. 8, p. 2349-2359, DOI:10.1007/BF02586209.
- [29] Matsui, K., Tanaka, K., Yamakawa, T., Uehara, M., Enomoto, N., Hojo, J. (2007). Sintering kinetics at isothermal shrinkage: II, effect of Y2O3 concentration on the initial sintering stage of fine zirconia powder. *Journal of the American Ceramic Society*, vol. 90, no. 2, p. 443-447, DOI:10.1111/j.1551-2916.2006.01440.x.
- [30] Savin, A., Novy, F., Fintova, S., Steigmann, R. (2017). Evaluation of thin discontinuities in planar conducting materials using the diffraction of electromagnetic field. *IOP Conference Series: Materials Science and Engineering*, vol. 227, no. 1, p. 012115, DOI:10.1063/1.323475.
- [31] Hanic, F., Hartmanova, M., Kundracik, F., Lomonova, E.E. (2003). Stabilization and properties of high temperature forms of zirconia. *Solid State Phenomena*, vol. 90-91, p. 303-308, DOI:10.4028/www.scientific.net/SSP.90-91.303.
- [32] Robinson, D., Ramsundar, P., Samantaray, C.B. (2014). Analyzing porosity in thermal barrier coatings: Edge detection of images using MATLAB. *121st American Society of Engineering Education Annual Conference*, paper ID: 8672.
- [33] Gustafson, S.C. (1995). Book Review: Goodman, J.W. Introduction to Fourier optics. *Optical Engineering*, vol. 35, no. 5, p. 1513-1513, DOI:10.1117/1.601121.
- [34] Langenberg, K.J., Fischer, M., Berger, M., Weinfurter, G. (1986). Imaging performance of generalized holography. *Journal of the Optical Society of America A*, vol. 3, no. 3, p. 329-339, DOI:10.1364/JOSAA.3.000329.
- [35] Savin, A., Steigmann, R., Bruma, A. (2015). Enhancement of spatial resolution using metamaterial sensor in nondestructive evaluation. *Emerging Technologies in Non-Destructive Testing VI*, p. 569-575, CRC Press, Boca Raton, DOI:10.1201/b19381-94.
- [36] Dodd, C.V., Deeds, W.E. (1968). Analytical solutions to eddy-current probe-coil problems. *Journal of Applied Physics*, vol. 39, no. 6, p. 2829-2838, DOI:10.1063/1.1656680.
- [37] Weller, M. (1994). Mechanical loss measurements on yttria-and calcia-stabilized zirconia. *Journal of Alloys and Compounds*, vol. 211-212, p. 66-70, DOI:10.1016/0925-8388(94)90449-9.

Vsebina

Strojniški vestnik - Journal of Mechanical Engineering

letnik 64, (2018), številka 11
Ljubljana, november 2018
ISSN 0039-2480

Izhaja mesečno

Razširjeni povzetki (extended abstracts)

- Tomoki Shiotani, Katsufumi Hashimoto, Hisafumi Asaue, Takahiro Nishida, Hidefumi Takamine, Kazuo Watabe, Masato Fukuda: Identifikacija lateralnih poškodb v AB ploščah z merjenjem elastičnih valov ob padavinah z različnimi tomografskimi pristopi SI 93
- Tomaž Kek, Dragan Kusić, Rajko Svečko, Aleš Hančič, Janez Grum: Analiza signalov akustične emisije za oceno integritete orodja SI 94
- Bibi Intan Suraya Murat, Paul Fromme, Marco Endrizzei, Alessandro Olivo: Karakterizacija udarnih poškodb na kompozitnih ploščah SI 95
- Adriana Savin, Nicoleta Iftimie, Rozina Steigmann, Dorin Rosu, Gabriel Silviu Dobrescu, Janez Grum, Paul Doru Barsanescu: Učinkovite metode za spremljanje stanja kritičnih con modelnih lopatic vetrnih turbin SI 96
- Valentyn Uchanin, Sergej Minakov, Giuseppe Nardoni, Orest Ostash, Sergej Fomichov: Neporušitvena metoda za določanje napetosti v jeklenih komponentah po metodi vrtničnih tokov SI 97
- Mariana Domnica Stanciu, Adriana Savin, Silviu Marian Nastac: Mehanske in površinske lastnosti kompozitov, ojačenih z lignoceluloznimi vlakni SI 98
- Adriana Savin, Mihail Liviu Craus, Vitaly Turchenko, Frantisek Novy, Aura C. Mocanu, Marian Soare, Janez Grum, Oleksandr Sergiyovich Doroshkevich: Komplementarne metode za vrednotenje prevlek v vlogi toplotne pregrade iz cirkonijevega dioksida, stabiliziranega z itrijevim oksidom SI 99

Identifikacija lateralnih poškodb v AB ploščah z merjenjem elastičnih valov ob padavinah z različnimi tomografskimi pristopi

Tomoki Shiotani^{1,*} – Katsufumi Hashimoto¹ – Hisafumi Asaue¹ – Takahiro Nishida¹
– Hidefumi Takamine² – Kazuo Watabe² – Masato Fukuda³

¹Univerza v Kjotu, Oddelek za gradbeništvo in zemeljske vire, Japonska

²Kawasaki, Toshiba Corporation, Japonska

³West Nippon Expressway Company Limited, Japonska

Potrebe po učinkovitih tehnikah za preiskave starajoče se infrastrukture so velike, saj Japonska porabi veliko sredstev za menjavo in popravilo plošč iz armiranega betona (AB) v cestni infrastrukturi. Da bi lahko zmanjšali stroške AB plošč in preusmerili sproščena sredstva za druge namene, kot je gradnja novih konstrukcij, je treba najprej kvantitativno ovrednotiti notranje poškodbe v armiranem betonu.

Na podlagi rezultatov preiskav bodo oblikovani racionalni programi vzdrževanja za minimalne stroške konstrukcij tekom življenjske dobe. Pri tovrstnih preiskavah se običajno uporabljajo radarska, infrardeča ali impulzna metoda, ki pa ne dajejo vedno uporabnih rezultatov. Avtorji zato preučujejo primernost neporušitvenih metod za kvantifikacijo notranjih poškodb v betonskih konstrukcijah. V članku je predstavljen predlog metode na osnovi AE (akustično-emisijske) tomografije za vizualizacijo in kvantifikacijo poškodb v realnih betonskih konstrukcijah.

Tehnika spremljanja sekundarne aktivnosti AE omogoča uspešno identifikacijo internih poškodb s pomočjo parametrov elastičnih valov, kot je hitrost. Potrjeno je, da je metoda uporabna za zbiranje podatkov o poškodbah v betonu pri grobem vrednotenju integritete konstrukcij. V študiji je bila za približno identifikacijo poškodb v AB ploščah uporabljena akustična aktivnost ob padavinah, ki je pri akustičnem nadzoru prej veljala za motnjo. In-situ meritve AE v mostnih AB ploščah so se izvajale en teden. Notranje poškodbe v ploščah so bile analizirane s konvencionalnimi tehnikami nadzora AE ter z AE tomografijo za spremljanje hitrosti elastičnih valov. Nato je bilo za verifikacijo odvzetih več vzorcev na tistih mestih, kjer so bile z nadzorom AE in hitrosti elastičnih valov ugotovljene različne poškodbe. Potrjeno je bilo zelo dobro ujemanje med hitrostjo elastičnih valov in dejanskimi poškodbami. V območjih intenzivne AE aktivnosti z visoko hitrostjo valov so bile najdene zmerne poškodbe, v območjih redke AE aktivnosti z nizko hitrostjo valov pa večje poškodbe. Z nekajminutnim spremljanjem AE aktivnosti, ki jo povzročajo dežne kapljice, je mogoče identificirati vire AE na osnovi lokacijskega algoritma, ki mu sledi analiza porazdelitve hitrosti in stopnje slabljenja s tehniko AE tomografije. Težje poškodbe v AB ploščah je mogoče odkriti z analizo porazdelitve virov AE ob padavinah: področja z gostimi viri AE so nedotaknjena ali imajo le manjše poškodbe, medtem ko se v področjih z redkimi viri AE skrivajo težje poškodbe AB plošč. Ta relacija je lahko osnova za hitro odločanje o menjavi ali popravilu AB plošč, ki ga dosedanje tehnike kontrole niso omogočale.

Tomografski pristop z merjenjem hitrosti elastičnih valov in slabljenja amplitude je bil povezan s spremljanjem AE aktivnosti ob padavinah, tako pridobljena karta poškodb pa je združljiva z rezultati dolgotrajnega nadzora sekundarne aktivnosti AE v betonskih ploščah.

Novi pristop zagotavlja učinkovito odkrivanje težjih poškodb na osnovi aktivnosti AE v dežju. Tomografski pristopi omogočajo tudi podrobnejše preiskave.

V prihodnjih raziskavah bo mogoče razjasniti še povezave med razsežnostmi poškodb in parametri elastičnih valov v odvisnosti od valovne dolžine oz. frekvence.

Ključne besede: akustična emisija, identifikacija poškodb, AB plošče, tomografija, elastični valovi ob padavinah, hitrost elastičnih valov, slabljenje energije elastičnih valov

Analiza signalov akustične emisije za oceno integritete orodja

Tomaz Kek^{1,*} – Dragan Kusić² – Rajko Svečko³ – Aleš Hančič² – Janez Grum¹

¹ Univerza v Ljubljani, Fakulteta za strojništvo, Slovenija

² TECOS, Slovenija

³ Univerza v Mariboru, Fakulteta za elektrotehniko, računalništvo in informatiko, Slovenija

Najpogostejši izvor signalov akustične emisije (AE), ki jih zaznamo z neporušnimi preiskusi, je rast razpoke in plastična deformacija materiala. Spremljanje signalov AE v materialu je pritegnilo veliko pozornost, saj omogoča nemoten nadzor procesov in izdelkov v uporabi, z zelo veliko občutljivostjo zaznavanja šibkega mehanskega valovanja. Injekcijsko brizganje je eden izmed najpogosteje uporabljenih proizvodnih procesov. Omogoča relativno enostaven proces izdelave izdelkov z majhnih izmetom izdelkov, vendar kljub temu zaznavanje poškodb v orodjih za injekcijsko brizganje in nadzor poteka procesa na osnovi zajetih signalov AE še ni dovolj raziskano in opisano področje v literaturi. V prispevku je predstavljena možnost integracije senzorjev akustične emisije za sočasno spremljanje stanja procesa in možnost ocene integritete orodja za injekcijsko brizganje polimernih materialov. Pri raziskavi je bil uporabljen polipropilen, ki se pogosto uporablja v avtomobilski industriji.

Uporabljeni so resonančni PZT senzorji akustične emisije, ki so akustično sklopljeni z orodjem preko valovnih vodnikov. Uporaba valovnih vodnikov omogoča zaščito senzorjev akustične emisije pred povišanimi temperaturami, parami in pred poškodbami zaradi posegov operaterja. Prikazani so izmerjeni signali akustične emisije pri uporabi novega orodja in orodja z generirano razpoko s postopkom zaporednega laserskega površinskega kaljenja. Za izvedbo preizkusa so standardni D2 ISO polipropilenski brizgani vzorci, ki se pogosto uporabljajo za analizo v skladu s standardom ISO 294-3. Izdelani vzorci z različnimi pogoji izdelave so bili tri-dimenzionalno optično premerjeni z namenom potrjevanja pogojev obdelave na dimenzijske spremembe, popačenje vzorcev in oceno spremembe integritete orodja na površino vzorca. Predstavljeni so izbruhi signalov akustične emisije med različnimi fazami injekcijskega brizganja pri uporabi votlice z lasersko generiranimi površinskimi razpokami. Definirane so različne značilke izbruhov signalov akustične emisije v časovnem in frekvenčnem prostoru z namenom ovrednotenja integritete orodja za brizganje in razpoznavo posameznih faz procesa injekcijskega brizganja. Da bi preseglji pomanjkljivosti Fourierjeve metode je vpeljana valčna analiza za obdelavo signalov akustične emisije med injekcijskim brizganjem. Valčna paketna dekompozicija (WPD) razdeli signal v več nivojev v celotnem frekvenčnem območju signala. Valčni paketi vsebujejo informacije o signalih v različnih časovnih oknih pri različni ločljivosti. Vsak paket pripada določenemu frekvenčnemu pasu. Določeni paketi vsebujejo pomembne informacije, medtem ko so določeni relativno nepomembni, kar potrjujejo tudi značilke izračunane na osnovi energije posameznih valčnih paketov. Z namenom zmanjšanja kompleksnosti in povečanja hitrosti izračunov je vpeljana metoda izbire manjšega števila značilk v podskupine značilk v ustreznem več-dimenzijskem prostoru, ki prav tako omogoča dobre klasifikacijske lastnosti sistema. Definirana podskupina značilk je bila uporabljena za razpoznavo vzorcev z nevronske mreže med celotnim ciklom injekcijskega brizganja. Resonančni senzorji zaradi svojega frekvenčnega odziva otežujejo klasifikacijo signalov v frekvenčni domeni. Rezultati raziskave kljub temu potrjujejo, da je merjenje signalov akustične emisije med injekcijskim brizganjem obetajoča tehnika za karakterizacijo integritete orodja med nemotenim procesom tudi v primeru uporabe cenovno bolj sprejemljivih resonančnih senzorjev.

Ključne besede: akustična emisija, injekcijsko brizganje, integriteta orodja, razpoznavanje vzorcev, izbira vektorjev značilk, Richardsonov diagram

Karakterizacija udarnih poškodb na kompozitnih ploščah

Bibi Intan Suraya Murat¹ – Paul Fromme² – Marco Endrizzei³ – Alessandro Olivo³

¹ Tehnična univerza MARA, FAKulteta za strojništvo, Malezija

² Univerzitetni kolidž v Londonu, Oddelek za strojništvo, Združeno kraljestvo

³ Univerzitetni kolidž v Londonu, Oddelek za medicinsko fiziko in biomedicinsko tehniko, Združeno kraljestvo

Kompozitni materiali se v današnjem času zelo pogosto uporabljajo pri različnih aplikacijah kjer izstopa letalska industrija. Ti materiali omogočajo prilagajanje svojih lastnosti različnim pogojem obratovanja pri danih primerih uporabe. Pomembna omejitev kompozitov je njihova zmanjšana sposobnost za prenašanje udarcev. Proces nastajanja poškodbe pri nizko hitrostnih udarcih v kompozitih je kompleksni pojav, ki običajno vključuje pokanje matrice, delaminacijo, ločitev vlaken od matrice in trganje vlaken. Nizke hitrostni udarci na kompozitih običajno povzročijo nastanek komaj vidnih poškodb na mestu trka, ki pa so ponavadi sestavljene iz več različnih tipov poškodb pod površino izdelkov. Njihova karakterizacija je zapletena in se razlikuje glede na kompozitno strukturo. Običajne metode pregleda kompozitnih materialov ne omogočajo hitrega pregleda večjih kompozitnih struktur s cenovno sprejemljivim pregledom. S tega stališča veliko obeta pregled kompozitov z vodenimi ultrazvočnimi valovi.

V članku je predstavljena karakterizacija poškodb zaradi nizko hitrostnega trka na ploščah iz ogljikovih vlaken in epoksija z različnimi neporušnimi metodami. Prikazana je sposobnost karakterizacije napake z vizualno tehnik na osnovi vodenih ultrazvočnih valov v primerjavi z bolj razširjenimi tehnikami ugotavljanja napak kot sta X žarkovna radiografija in podvodni ultrazvočni C način pregledovanja materialov. V okviru vodenih ultrazvočnih valov so za pregled vzorca uporabljeni nizko frekvenčni asimetrični A0 vodeni ultrazvočni valovi, ki jih v izdelku vzbujajo z nizko-cenovno PZT glavo. Glava je pozicionirana 50 mm od mesta udarca. Vzbujanje je izvedeno s 100 kHz sinusnim signalom petih valovnih dolžin. Širjenje vodenega valovanja v plošči je merjeno brez-dotično s komercialno dostopnim laserskim vibrometrom na področju velikosti 40 mm × 40 mm s korakom 1 mm v obeh smereh. Interakcija vodenih valov v kompozitni plošči z udarno poškodbo se odraža v sipanju valovanja na mestu poškodbe. Relativno izrazito sipanje zaradi poškodbe je zaznati, ko valovanje zapusti področje poškodbe v kompozitni plošči. Analiza z metodo končnih elementov potrjuje, da prihaja znotraj območja poškodbe tudi do odboja valovanja na mejah območja poškodbe. Večkratno odbijanje valovanja na mejah območja poškodbe omogoča, da ostane ujete veliko energije vodenega valovanja, kar se odraža tudi v povišani amplitudi vodenega valovanja v območju udarne poškodbe kompozitne plošče.

Uporaba X žarkovne radiografije na uporabljenih referenčnih vzorcih uporabljenih v okviru predloženega članka, omogoča zaznavo lokalne razslojitve med vlakni ter matrico kot tudi zaznavanje pokanja matrice v kompozitnih vzorcih. Ultrazvočni pregled istih vzorcev s C načinom omogoča uporabno oceno velikosti in globine udarne poškodbe. Pregled mesta poškodbe z vodenimi ultrazvočnimi valovi pa na osnovi sipanih vodenih valov na mestu udarne poškodbe na kompozitni plošči omogoča vpogled v lokacijo udarne poškodbe, njene globine, dolžine in širine. Primerjava obravnavanih metod je pokazala, da metoda z vodenimi ultrazvočnimi valovi omogoča določevanje udarnih poškodb v kompozitni plošči z uporabo manjše in cenejše opreme s hitro postavitvijo merilne opreme in izvedbo hitre meritve.

Ključne besede: kompozitne plošče, nizko hitrostni udarci, X žarki, ultrazvočni C način, vodeni valovi

Učinkovite metode za spremljanje stanja kritičnih con modelnih lopatic vetrnih turbin

Adriana Savin^{1,*} – Nicoleta Iftimie¹ – Rozina Steigmann¹ – Dorin Rosu² –
Gabriel Silviu Dobrescu¹ – Janez Grum³ – Paul Doru Barsanescu⁴

¹Nacionalni inštitut za raziskave in razvoj v tehnični fiziki, Oddelek za neporušitvene preiskave, Romunija

²S.C. Compozite S.A, Romunija

³Univerza v Ljubljani, Fakulteta za strojništvo, Slovenija

⁴Tehniška univerza Gheorghe Asachi, Fakulteta za strojništvo, Romunija

V članku so predstavljeni rezultati preizkusov in spremljanja modelne lopatice vetrne turbine (WTB) z različnimi zaznavali, ki so bila postavljena na kritičnih mestih, določenih s simulacijo po metodi končnih elementov (MKE). Podana je primerjava komplementarnih metod za izbiro metode, ki bo najučinkovitejša glede razmerja med kakovostjo in ceno.

Modelna lopatica vetrne turbine je bila preizkušena v razmerah statične obremenitve s tremi vrsti zaznaval (brezžični merilnik raztezka (WRS) s tehnologijo RFID, optično vlakno (OF) z Braggovo uklonsko mrežico (FBG), uporovni lističi (SG)) za zaznavanje morebitnih poškodb, ki bi lahko privedle do nevarnih napak. Cilj pričujočega dela je dokazati, da je ta metodologija za modelne pomanjšane lopatice uporabna tudi za lopatice realne velikosti. Avtorjem niso znane predhodne raziskave lopatic vetrnih turbin te vrste.

Zaznavala z optičnim vlaknom (OF) omogočajo spremljanje kritičnih predelov konstrukcij. Ko je vlakno izpostavljeno raztežkom, se centralna valovna dolžina premakne proti višji ali nižji vrednosti. Pasivna zaznavala WRS za spremljanje napetosti/raztezkov imajo občutljiv element, ki se pod obremenitvijo razteza (krči ali širi) skupaj z nadzorovano komponento. Rozete s tremi uporovnimi lističi omogočajo določitev glavnih napetosti splošnega dvoosnega napetostnega stanja. Njihova prednost je v tem, da so tanke in upogljive, se dobro prilegajo ukrivljenim površinam, imajo minimalen učinek ojačenja in odlično odvajajo toploto na preizkušanelec. Simulacija vedenja lopatice je bila opravljena s paketom ANSYS Academic 17.2. Na oddaljenosti 300 mm od vrha lopatice je bila uporabljena tlačna sila 500 N v osi Y (zgornja lupina lopatice) na področju, širokem 100 mm. Pri tem je nastal odmik konice v vrednosti 30,082 mm.

Preizkusi so bili opravljeni na pomanjšanih modelih. V prihodnjih raziskavah bodo vključena zaznavala WRS, saj bodo lopatice v okviru projekta vgrajene v demonstracijski sistem za potrditev pravilnosti rešitev ter zanesljivosti diagnostike in napovedovanja, oceno preostale življenjske dobe in upravljanje vzdrževanja.

Spremljanje modelne lopatice vetrne turbine je bilo izvedeno s komplementarnimi neporušitvenimi metodami. Uporabljena so bila zaznavala različnih vrst, ki so bila nameščena na kritičnih mestih na lopatici: optično vlakno z Braggovo uklonsko mrežico, brezžična zaznavala na osnovi metamaterialov in klasična rozeta z uporovnimi lističi. Kritične cone so bile določene po MKE. Opravljena je bila primerjava rezultatov za eksperimentalno potrditev teoretično določenih območij največje koncentracije napetosti.

Ključne besede: lopatice vetrnih turbin, spremljanje stanja konstrukcij (SHM), neporušitveni preizkusi, brezžična zaznavala, Bragrove uklonske mrežice (FBG), uporovni lističi (SG)

Neporušitvena metoda za določanje napetosti v jeklenih komponentah po metodi vrtničnih tokov

Valentyn Uchanin^{1,*} – Sergej Minakov² – Giuseppe Nardoni³ – Orest Ostash¹ – Sergej Fomichov²

¹ Inštitut za fiziko in mehaniko Karpenko pri Nacionalni akademiji znanosti, Lvov, Ukrajina

² Politehnični inštitut v Kijevu, Kijev, Ukrajina

³ I&T Nardoni Institute, Folzano, Brescia, Italija

Obremenitve in preostale napetosti lahko vplivajo na obratovalno stanje konstrukcij in komponent. Preostale napetosti po varjenju tako povzročijo krhki lom in razpoke zaradi napetostne korozije, ki lahko občutno skrajšajo utrujenostno trajnostno dobo varjenih konstrukcij. V članku je predstavljen razvoj metode po načelu vrtničnih tokov (EC) za določanje napetosti v komponentah iz feromagnetnega jekla na osnovi sprememb magnetne anizotropije pri feromagnetnih materialih pod obremenitvijo zaradi prerazporejanja magnetnih domen v povezavi z reverznim magnetostrikijskim (Villarijevim) efektom.

V tej raziskavi so bile obravnavane metode na osnovi magnetne anizotropije (MA) kot ena od različic metode EC. Razvita je bila nova vrsta napetostno občutljive sonde EC z delovnim premerom 18 mm, sestavljena iz po dveh identičnih vzbujalnih in zaznavalnih tuljav, postavljenih v oglišča štirikotnika. Pri tej sondi so vse tuljave nameščene na feritna jedra premera 4,3 mm. Vzbujalne tuljave sonde so vezane zaporedno in usmerjene tako, da ustvarjajo karakteristično nevtravno ravnino, v kateri je vertikalna komponenta skupnega elektromagnetnega polja enaka nič. Zaznavalni tuljavi sta orientirani tako, da sta občutljivi na vertikalno komponento elektromagnetnega polja in vgrajeni v nevtralni ravnini, kjer je ta komponenta pri izotropnih medijih enaka nič. Zasnova zagotavlja dvojni diferencialni signal.

Preizkušavec dolžine 450 mm, debeline 8 mm in širine 60 mm je bil izdelan iz maloogljivega jekla (masna sestava v %: 0,10 C, 0,42 Si, 1,47 Mn). Preizkušavec je bil pred obremenitvijo eno uro žarjen pri temperaturi 720 °C (pretežno feritna struktura z napetostjo tečenja $\sigma_{YS} = 305$ MPa) za odstranitev morebitnih preostalih napetosti, nato pa je bil z njim izveden štiritočkovni upogibni preizkus. Sonda EC je bila nameščena na sredini preizkušanca, ki je bil obremenjen tako, da so nastale natezne in tlačne napetosti od 0 do 225 MPa. Sonda EC je bila v ta namen postavljena na različnih straneh štiritočkovno obremenjenega preizkušanca. Zabeleženi so bili hodografi odzivnega signala sonde EC v kompleksni ravnini pri delovnih frekvencah 5,0 kHz in 50,0 kHz. Izkazalo se je, da imajo hodografi za natezne in tlačne napetosti različne smeri v kompleksni ravnini, ta posebnost pa omogoča določanje vrste napetosti (nateznej ali tlačnej). Opredeljena je odvisnost amplitude signala sonde EC od nateznej in tlačnej napetosti pri delovni frekvenci 5,0 kHz med obremenjevanjem do 225 Mpa in nato med razbremenitvijo. Rezultati so pokazali visoko občutljivost dvojno diferencialne sonde EC na natezne in tlačne napetosti ter obstoj magneto-mehanske histereze.

Dva preizkušanca iz srednjeogljivega jekla (masna sestava v %: 0,66 C; 0,29 Si; 1,02 Mn; 0,12 Cr) sta bila dolga 150 mm, debela 3 mm in široka 30 mm. Uporabljena sta bila za preučitev vpliva mikrostrukture jekla na odzivni signal sonde EC v stanju natezne obremenitve. Prvi preizkušavec je bil dve uri žarjen na temperaturi 830 °C in je imel pretežno perlitno strukturo ($\sigma_{YS} = 560$ MPa). Drugi preizkušavec je bil gašen v olju (začetna temperatura 830 °C), čemur je sledilo popuščanje (dve uri pri 380 °C). Struktura je bila pretežno troostitna ($\sigma_{YS} = 1510$ MPa). Preizkušenci so bili obremenjeni na stroju za natezni preizkus do 500 MPa za dokaz invariantnosti metode MA glede na strukturo jekla. Rezultati študije so osvetlili potencial metode za merjenje napetosti neodvisno od strukture materiala, po čemer se nova metoda razlikuje od metod na osnovi koercitivnosti ali Barkhausnovega šuma.

Z metodo MA je bila tako opravljena analiza preostalih napetosti po varjenju in ocena napetosti v mostni jekleni konstrukciji med navarjanjem na stebre.

Prihodnje raziskave bodo usmerjene v lastnosti magneto-mehanske histereze za zmanjšanje napak.

Ključne besede: vrtnični tokovi, magnetna anizotropija, obremenitve in preostale napetosti, natezne napetosti, tlačne napetosti, magneto-mehanska histereza, varjenje, mostna konstrukcija

Mehanske in površinske lastnosti kompozitov, ojačenih z lignoceluloznimi vlakni

Mariana Domnica Stanciu^{1,*} – Adriana Savin² – Silviu Marian Nastac³

¹Transilvanska univerza v Brasovu, Oddelek za proizvodno strojništvo, Romunija

²Nacionalni inštitut za raziskave in razvoj in razvoj in tehnični fiziki, Oddelek za neporušitvene preiskave, Romunija

³Univerza regije Galati »Dunarea de Jos«, Fakulteta za tehniko in agronomijo, Romunija

Članek opisuje mehanske in površinske lastnosti kompozitov, ojačenih z lignoceluloznimi vlakni, pred fotodegradacijo in po njej. UV-sevanje škoduje mehanskim lastnostim kompozita, saj vpliva na hidrofobno vedenje osnove.

Uporaba lignoceluloznih kompozitov s polimerno osnovo v okolju z UV-sevanjem lahko povzroči fotodegradacijo, s tem pa oslabitev materiala in mikrorazpoke v osnovi. Fotodegradacija je glavni učinek delovanja UV-sevanja iz okolice na polimerne materiale, ki se kaže v naslednjih pojavih: prekinitev kemičnih vezi med verigami polimerov, oblikovanje prostih radikalov zaradi razpada vezi C-H v polimernih verigah ter oksidacija površine zaradi peroksidnih radikalov. Material, ki je izpostavljen UV-sevanju, lahko tudi postane občutljivejši na druge dejavnike (npr. vlažnost).

Preučeni sta bili dve vrsti kompozitov. Preizkušanci so bili izrezani iz plošč v skladu s priporočili evropskih standardov za upogibne preizkuse po tritočkovni metodi. Prvi lignocelulozni kompozit je bil komercialni izdelek za avtomobilsko industrijo iz poliuretanske smole in 50 % konopljinih vlaken za ojačitev. Drugi kompozit je bil narejen po novi recepturi s 25-odstotnim volumskim deležem vlaken v obliki hrastovih delcev. Vlakna so bila zmešana s poliestrsko smolo POLYLITE 440 - M888 po metodi ročnega laminiranja. V kalupu je bilo izdelanih pet različnih plošč pri temperaturi strjevanja 22 °C. Morfologija površine vzorcev je bila analizirana po metodi kontaktnega kota in z določitvijo površinske hrapavosti z mikroskopom na atomsko silo NTEGRA Probe Nanolaboratory. Nato sta bila z dinamično mehansko analizo določena prožnostni modul E' in modul izgub E'' v izotermnih pogojih ($T = 30$ °C) ob spreminjanju frekvence obremenjevanja ($f = 1$ Hz, 5 Hz, 10 Hz, 50 Hz). Preizkušanci so bili v naslednjem koraku v sevalni komori s fluorescentnimi sijalkami Philips moči 18 W, razporejenimi pod kotom 120°, za 168 ur (7 dni) izpostavljeni UV-sevanju valovne dolžine $\lambda = 365$ nm. Sledila je ponovitev vseh zgoraj naštetih preizkusov.

Z vidika kontaktnega kota in površinske energije je bilo ugotovljeno, da UV-sevanje vpliva na površinsko strukturo lignoceluloznih kompozitov, ojačenih z večjimi delci (od 0,2 mm do 1 mm). Vzorci iz poliestrske smole in lesnih delcev velikosti 0,04 mm in 0,01 mm so bili kemično stabilnejši. S povečanjem velikosti ojačitvenih delcev se je povečalo tudi notranje trenje v kompozitni strukturi po izpostavitvi UV-sevanju. Največja razlika je bila ugotovljena pri kompozitih, ojačenih z delci velikosti 1 mm (modul izgub E'' se je povečal za 60 % do 76 %). Pri zelo majhnih lesnih delcih (do 0,04 mm) se je notranje trenje bolj zmanjšalo po fotolizi preizkušancev, kar je razvidno iz manjših vrednosti viskoznega modula po izpostavitvi UV-sevanju. Ker so bili preizkušanci izpostavljeni upogibu, so se največje napetosti pojavile v zgornjih in spodnjih slojih, to pa tudi pojasnjuje signifikanten vpliv UV-sevanja zaradi procesa zamreženja polimera v strukturi kompozita.

Predstavljena raziskava se lahko nadaljuje s preučevanjem viskoelastičnega vedenja kompozitov, ojačenih z lesnimi delci, po daljši izpostavitvi UV-sevanju ali temperaturnim nihanjem. Povečati bi bilo mogoče tudi število vzorcev za boljšo statistično značilnost in spremeniti volumske deleže komponent v recepturi za pripravo kompozita.

Virov na temo sprememb mehanskih in morfoloških lastnosti lignoceluloznih kompozitov na osnovi poliestra pod vplivom UV-sevanja je razmeroma malo. Preučevanje lignoceluloznih kompozitov in določanje strukturnih sprememb površine po izpostavitvi UV-sevanju je zelo pomembno zaradi hidrofилnega značaja celuloze. Določene so bile spremembe prožnostnega modula (E') in modula izgub (E'') pred izpostavitvijo UV-sevanju in po njej. Za analizo mehanskega vedenja in površinskih sprememb so bile uporabljene neporušitvene metode.

Ključne besede: lignocelulozni kompozit, prožnostni modul, modul izgub, površinska energija, metoda kontaktnega kota, UV-degradacija

Komplementarne metode za vrednotenje prevlek v vlogi toplotne pregrade iz cirkonijevega dioksida, stabiliziranega z itrijevim oksidom

Adriana Savin^{1,*} – Mihail Liviu Craus^{1,2} – Vitaly Turchenko² – Frantisek Novy³ –
Aura C. Mocanu⁴ – Marian Soare⁴ – Janez Grum⁵ – Oleksandr Sergiyovich Doroshkevich^{2,6}

¹Nacionalni inštitut za raziskave in razvoj v tehnični fiziki, Oddelek za neporušitvene preiskave, Romunija

²Skupni inštitut za jedrske raziskave, Frankov laboratorij za nevtronsko fiziko, Rusija

³Univerza v Žilini, Fakulteta za strojništvo, Slovaška republika

⁴SC Nuclear NDT Research and Services SRL, Romunija

⁵Univerza v Ljubljani, Fakulteta za strojništvo, Slovenija

⁶Ukrajinska nacionalna akademija znanosti, Fizikalno-tehniški inštitut v Donecku »A. A. Galkin«, Ukrajina

V članku je predstavljen uporaba elektromagnetne neporušitvene (NDE) metode na osnovi elektromagnetnega senzorja (EM) z lečo iz metamateriala za vrednotenje prevlek iz cirkonijevega dioksida na jeklu AISI 316L. Metamateriali (MM), v tem primeru konična »švicarska rulada« (Conical Swiss Roll, CSR), lahko služijo kot koncentratorji EM pretoka v radiofrekvenčnem območju. EM leča v senzorju je zasnovana po načelih Fourierjeve optike in omogoča izboljšanje prostorske ločljivosti metode za vrednotenje kakovosti površine in oprijema prevleke s podlago. Za preiskave vzorcev so bile uporabljene tudi komplementarne metode vrstična elektronska mikroskopija (SEM), rentgenska difrakcija (XRD) in nevtronska difrakcija (ND).

Potencial prevlek za toplotno pregrado (TBC) ni le v lastnostih samega materiala, temveč tudi v mikrostrukturi prevleke, ki je odvisna od postopka nalaganja. Nanokompoziti z nanometrskimi delci druge faze v keramični osnovi in/ali na kristalnih mejah lahko vzdržijo temperaturne cikle pri bistveno višjih temperaturah kot preproste prevleke YSZ. Zaradi manjšega števila praznin imajo tudi bistveno večjo trdnost in odpornost proti lezenju. Vrednotenje površinske strukture in morebitnega razslojevanja na stiku naloženih slojev tovrstnih prevlek cirkonijevega dioksida na nerjavnem jeklu je zato pomembna naloga.

Za opredelitev točnosti rezultatov ter korelacije med najdenimi drobnimi napakami in odzivom senzorja z MM bodo potrebni dodatni testi na večjem številu preizkušancev z različnimi prevlekami, ki bodo razkrili vpliv površinske hrapavosti na koeficient lomne žilavosti ter vpliv števila slojev. Rezultate bi bilo mogoče dopolniti z dodatnimi preiskavami po metodah ND, rentgenske difrakcije in drugih, ki omogočajo določitev fazne sestave in strukturnih parametrov.

Novost je v načinu nalaganja slojev cirkonijevega dioksida brez vmesnega substrata TGO, majhni debelini naloženih slojev in v metodi neporušitvene preiskave. Vključene so bile tudi alternativne metode za karakterizacijo prevlek, kot so vrstična elektronska mikroskopija (SEM), rentgenska difrakcija in metalografske preiskave.

Ključne besede: keramika na osnovi ZrO_2 , itrijev oksid, vrstična elektronska mikroskopija, ND, rentgenska difrakcija, EM test

Information for Authors

All manuscripts must be in English. Pages should be numbered sequentially. The manuscript should be composed in accordance with the Article Template given above. The maximum length of contributions is 10 pages. Longer contributions will only be accepted if authors provide justification in a cover letter. For full instructions see the Information for Authors section on the journal's website: <http://en.sv-jme.eu>.

SUBMISSION:

Submission to SV-JME is made with the implicit understanding that neither the manuscript nor the essence of its content has been published previously either in whole or in part and that it is not being considered for publication elsewhere. All the listed authors should have agreed on the content and the corresponding (submitting) author is responsible for having ensured that this agreement has been reached. The acceptance of an article is based entirely on its scientific merit, as judged by peer review. Scientific articles comprising simulations only will not be accepted for publication; simulations must be accompanied by experimental results carried out to confirm or deny the accuracy of the simulation. Every manuscript submitted to the SV-JME undergoes a peer-review process.

The authors are kindly invited to submit the paper through our web site: <http://ojs.sv-jme.eu>. The Author is able to track the submission through the editorial process - as well as participate in the copyediting and proofreading of submissions accepted for publication - by logging in, and using the username and password provided.

SUBMISSION CONTENT:

The typical submission material consists of:

- A **manuscript** (A PDF file, with title, all authors with affiliations, abstract, keywords, highlights, inserted figures and tables and references),
 - Supplementary files:
 - a **manuscript** in a WORD file format
 - a **cover letter** (please see instructions for composing the cover letter)
 - a ZIP file containing **figures** in high resolution in one of the graphical formats (please see instructions for preparing the figure files)
 - possible **appendices** (optional), cover materials, video materials, etc.
- Incomplete or improperly prepared submissions will be rejected with explanatory comments provided. In this case we will kindly ask the authors to carefully read the Information for Authors and to resubmit their manuscripts taking into consideration our comments.

COVER LETTER INSTRUCTIONS:

Please add a **cover letter** stating the following information about the submitted paper:

1. **Paper title**, list of **authors** and their **affiliations**.
2. **Type of paper**: original scientific paper (1.01), review scientific paper (1.02) or short scientific paper (1.03).
3. A **declaration** that neither the manuscript nor the essence of its content has been published in whole or in part previously and that it is not being considered for publication elsewhere.
4. State the **value of the paper** or its practical, theoretical and scientific implications. What is new in the paper with respect to the state-of-the-art in the published papers? Do not repeat the content of your abstract for this purpose.
5. We kindly ask you to suggest at least two **reviewers** for your paper and give us their names, their full affiliation and contact information, and their scientific research interest. The suggested reviewers should have at least two relevant references (with an impact factor) to the scientific field concerned; they should not be from the same country as the authors and should have no close connection with the authors.

FORMAT OF THE MANUSCRIPT:

The manuscript should be composed in accordance with the Article Template. The manuscript should be written in the following format:

- A **Title** that adequately describes the content of the manuscript.
- A list of **Authors** and their **affiliations**.
- An **Abstract** that should not exceed 250 words. The Abstract should state the principal objectives and the scope of the investigation, as well as the methodology employed. It should summarize the results and state the principal conclusions.
- 4 to 6 significant **key words** should follow the abstract to aid indexing.
- 4 to 6 **highlights**; a short collection of bullet points that convey the core findings and provide readers with a quick textual overview of the article. These four to six bullet points should describe the essence of the research (e.g. results or conclusions) and highlight what is distinctive about it.
- An **Introduction** that should provide a review of recent literature and sufficient background information to allow the results of the article to be understood and evaluated.
- A **Methods** section detailing the theoretical or experimental methods used.
- An **Experimental section** that should provide details of the experimental set-up and the methods used to obtain the results.
- A **Results** section that should clearly and concisely present the data, using figures and tables where appropriate.
- A **Discussion** section that should describe the relationships and generalizations shown by the results and discuss the significance of the results, making comparisons with previously published work. (It may be appropriate to combine the Results and Discussion sections into a single section to improve clarity.)
- A **Conclusions** section that should present one or more conclusions drawn from the results and subsequent discussion and should not duplicate the Abstract.
- **Acknowledgement** (optional) of collaboration or preparation assistance may be included. Please note the source of funding for the research.
- **Nomenclature** (optional). Papers with many symbols should have a nomenclature that defines all symbols with units, inserted above the references. If one is used, it must contain all the symbols used in the manuscript and the definitions should not be repeated in the text. In all cases, identify the symbols used if they are not widely recognized in the profession. Define acronyms in the text, not in the nomenclature.
- **References** must be cited consecutively in the text using square brackets [1] and collected together in a reference list at the end of the manuscript.
- **Appendix(-ices)** if any.

SPECIAL NOTES

Units: The SI system of units for nomenclature, symbols and abbreviations should be followed closely. Symbols for physical quantities in the text should be written in italics (e.g. v , T , n , etc.). Symbols for units that consist of letters should be in plain text (e.g. ms^{-1} , K, min, mm, etc.). Please also see: <http://physics.nist.gov/cuu/pdf/sp811.pdf>.

Abbreviations should be spelt out in full on first appearance followed by the abbreviation in parentheses, e.g. variable time geometry (VTG). The meaning of symbols and units belonging to symbols should be explained in each case or cited in a **nomenclature** section at the end of the manuscript before the References.

Figures (figures, graphs, illustrations digital images, photographs) must be cited in consecutive numerical order in the text and referred to in both the text and the captions as Fig. 1, Fig. 2, etc. Figures should be prepared without borders and on white grounding and should be sent separately in their original formats. If a figure is composed of several parts, please mark each part with a), b), c), etc. and provide an explanation for each part in Figure caption. The caption should be self-explanatory. Letters and numbers should be readable (Arial or Times New Roman, min 6 pt with equal sizes and fonts in all figures). Graphics (submitted as supplementary files) may be exported in resolution good enough for printing (min. 300 dpi) in any common format, e.g. TIFF, BMP or JPG, PDF and should be named Fig1.jpg, Fig2.tif, etc. However, graphs and line drawings should be prepared as vector images, e.g. CDR, AI. Multi-curve graphs should have individual curves marked with a symbol or otherwise provide distinguishing differences using, for example, different thicknesses or dashing.

Tables should carry separate titles and must be numbered in consecutive numerical order in the text and referred to in both the text and the captions as Table 1, Table 2, etc. In addition to the physical quantities, such as t (in italics), the units [s] (normal text) should be added in square brackets. Tables should not duplicate data found elsewhere in the manuscript. Tables should be prepared using a table editor and not inserted as a graphic.

REFERENCES:

A reference list must be included using the following information as a guide. Only cited text references are to be included. Each reference is to be referred to in the text by a number enclosed in a square bracket (i.e. [3] or [2] to [4] for more references; do not combine more than 3 references, explain each). No reference to the author is necessary.

References must be numbered and ordered according to where they are first mentioned in the paper, not alphabetically. All references must be complete and accurate. Please add DOI code when available. Examples follow.

Journal Papers:

Surname 1, Initials, Surname 2, Initials (year). Title. Journal, volume, number, pages, DOI code.

- [1] Hackenschmidt, R., Alber-Laukant, B., Rieg, F. (2010). Simulating nonlinear materials under centrifugal forces by using intelligent cross-linked simulations. *Strojniški vestnik - Journal of Mechanical Engineering*, vol. 57, no. 7-8, p. 531-538, DOI:10.5545/sv-jme.2011.013.

Journal titles should not be abbreviated. Note that journal title is set in italics.

Books:

Surname 1, Initials, Surname 2, Initials (year). Title. Publisher, place of publication.

- [2] Groover, M.P. (2007). *Fundamentals of Modern Manufacturing*. John Wiley & Sons, Hoboken.

Note that the title of the book is italicized.

Chapters in Books:

Surname 1, Initials, Surname 2, Initials (year). Chapter title. Editor(s) of book, book title. Publisher, place of publication, pages.

- [3] Carbone, G., Ceccarelli, M. (2005). Legged robotic systems. Kordić, V., Lazinica, A., Merdan, M. (Eds.), *Cutting Edge Robotics*. Pro literatur Verlag, Mammendorf, p. 553-576.

Proceedings Papers:

Surname 1, Initials, Surname 2, Initials (year). Paper title. Proceedings title, pages.

- [4] Štefanič, N., Martinčević-Mikić, S., Tošanović, N. (2009). Applied lean system in process industry. *MOTSP Conference Proceedings*, p. 422-427.

Standards:

Standard-Code (year). Title. Organisation. Place.

- [5] ISO/DIS 16000-6.2:2002. *Indoor Air - Part 6: Determination of Volatile Organic Compounds in Indoor and Chamber Air by Active Sampling on TENAX TA Sorbent, Thermal Desorption and Gas Chromatography using MSD/FID*. International Organization for Standardization. Geneva.

WWW pages:

Surname, Initials or Company name. Title, from <http://address>, date of access.

- [6] Rockwell Automation. Arena, from <http://www.arenasimulation.com>, accessed on 2009-09-07.

EXTENDED ABSTRACT:

When the paper is accepted for publishing, the authors will be requested to send an **extended abstract** (approx. one A4 page or 3500 to 4000 characters). The instruction for composing the extended abstract are published on-line: <http://www.sv-jme.eu/information-for-authors/>.

COPYRIGHT:

Authors submitting a manuscript do so on the understanding that the work has not been published before, is not being considered for publication elsewhere and has been read and approved by all authors. The submission of the manuscript by the authors means that the authors automatically agree to transfer copyright to SV-JME when the manuscript is accepted for publication. All accepted manuscripts must be accompanied by a Copyright Transfer Agreement, which should be sent to the editor. The work should be original work by the authors and not be published elsewhere in any language without the written consent of the publisher. The proof will be sent to the author showing the final layout of the article. Proof correction must be minimal and executed quickly. Thus it is essential that manuscripts are accurate when submitted. Authors can track the status of their accepted articles on <http://en.sv-jme.eu/>.

PUBLICATION FEE:

Authors will be asked to pay a publication fee for each article prior to the article appearing in the journal. However, this fee only needs to be paid after the article has been accepted for publishing. The fee is 320 EUR (for articles with maximum of 6 pages), 400 EUR (for articles with maximum of 10 pages), plus 40 EUR for each additional page. The additional cost for a color page is 90.00 EUR. These fees do not include tax.

Strojniški vestnik - Journal of Mechanical Engineering
Askerčeva 6, 1000 Ljubljana, Slovenia,
e-mail: info@sv-jme.eu



<http://www.sv-jme.eu>

Contents

Papers

- 657 Tomoki Shiotani, Katsufumi Hashimoto, Hisafumi Asaue, Takahiro Nishida, Hidefumi Takamine, Kazuo Watabe, Masato Fukuda:
Lateral Damage Identification in RC Slabs by Several Tomographic Approaches with Rainy Induced Elastic Waves
- 665 Tomaž Kek, Dragan Kusić, Rajko Svečko, Aleš Hančič, Janez Grum:
Acoustic Emission Signal Analysis for the Integrity Evaluation
- 672 Bibi Intan Suraya Murat, Paul Fromme, Marco Endrizzei, Alessandro Olivo:
Characterization of Impact Damage in Composite Plates
- 680 Adriana Savin, Nicoleta Iftimie, Rozina Steigmann, Dorin Rosu, Gabriel Silviu Dobrescu, Janez Grum, Paul Doru Barsanescu:
Effective Methods for Structural Health Monitoring of Critical Zones of Scalable Wind Turbine Blades
- 690 Valentyn Uchanin, Sergej Minakov, Giuseppe Nardoni, Orest Ostash, Sergej Fomichov:
Nondestructive Determination of Stresses in Steel Components by Eddy Current Method
- 698 Mariana Domnica Stanciu, Adriana Savin, Silviu Marian Nastac:
Mechanical and Surface Properties of Lignocellulosic Fibres Reinforced Composites
- 706 Adriana Savin, Mihail Liviu Craus, Vitaly Turchenko, Frantisek Novy, Aura C. Mocanu, Marian Soare, Janez Grum, Oleksandr Sergiyovich Doroshkevich:
Complementary Methods for Evaluation of Yttria Stabilized Zirconia Coatings used as Thermal Barrier Coating